

©Copyright 2020

M. P. Ross

Precision Mechanical Rotation Sensors for Terrestrial Gravitational Wave Observatories

M. P. Ross

A dissertation
submitted in partial fulfillment of the
requirements for the degree of

Doctor of Philosophy

University of Washington

2020

Reading Committee:

Jens Gundlach, Chair

Eric Adelberger

Sanjay Reddy

Program Authorized to Offer Degree:
Physics

University of Washington

Abstract

Precision Mechanical Rotation Sensors for Terrestrial Gravitational Wave Observatories

M. P. Ross

Chair of the Supervisory Committee:
Professor Jens Gundlach
Physics

The LIGO observatories are comprised of 4-km long dual recycled Fabry-Perot Michelson interferometers. Each observatory deploys a multi-stage seismic isolation system to isolate from terrestrial seismic motion. These systems use seismometers to measure motion at a broad band of frequencies.

Seismometers are inherently susceptible to contamination due to tilts. These dominate the seismometer readings at low frequency limiting the performance of LIGO's seismic isolation. We developed low-frequency inertial rotation sensors to subtract this tilt-contamination from ground seismometers. These sensors were deployed at both LIGO observatories which allowed for operation at high wind speeds.

In addition, a compact rotation sensor was developed with the capability of being deployed on the LIGO seismic isolation platforms. A prototype was built and tested. A theoretical control model was designed to exploit this novel sensor. This model showed a significant decrease in control noise leakage into the gravitational wave band.

These sensors have found application in a number of auxiliary fields. The ground rotation sensors have allowed for novel seismological studies while the compact rotation sensor has been applied to study of Newtonian noise.

TABLE OF CONTENTS

	Page
List of Figures	iii
Chapter 1: Introduction	2
1.1 Gravitational Wave Theory	2
1.1.1 Linearized General Relativity	2
1.1.2 Compact Binary Coalescence	4
1.2 LIGO	5
1.2.1 Sensitivity	5
1.2.2 Events	8
1.3 Seismic Isolation	10
1.3.1 LIGO Isolation Scheme	10
1.3.2 Internal Seismic Isolation	11
1.3.3 Sensor Correction	14
Chapter 2: 1-meter Scale Ground Rotation Sensors	16
2.1 Ground Tilt	16
2.1.1 Tilt Contamination	16
2.1.2 Sensor Correction with Tilt Subtraction	18
2.2 Beam Rotation Sensors	19
2.2.1 Mechanical System	19
2.2.2 Flexures	23
2.2.3 Vacuum System	23
2.2.4 Multi-Slit Autocollimator Readout	24
2.2.5 Controls	30
2.2.6 Noise Performance	31
2.3 Results	33

2.3.1	Hanford Installation	33
2.3.2	Livingston Installation	35
2.3.3	Ground Tilt Model	36
2.3.4	Duty Cycle Improvements	38
Chapter 3:	30-cm Scale On-Board Rotation Sensors	42
3.1	Angular Controls	42
3.2	Compact Beam Rotation Sensor	44
3.2.1	Mechanical System	44
3.2.2	Kinematic Mount	45
3.2.3	Interferometric Readout	47
3.2.4	Calibration	50
3.2.5	Mass Adjustment	52
3.2.6	Controls	54
3.2.7	Noise Performance	54
3.3	Projected Improvements	55
3.3.1	Isolation Scheme	55
3.3.2	Angular Control Performance	65
Chapter 4:	Auxiliary Applications	69
4.1	Geophysics	69
4.1.1	Rayleigh Wave Theory	69
4.1.2	Wave-Field Parameter Extraction	72
4.1.3	Single Station Dispersion Measurements	73
4.2	Newtonian Noise	75
4.2.1	Theory	75
4.2.2	Observations	77

LIST OF FIGURES

Figure Number	Page
1.1 Spectrogram of the strain caused by a binary neutron star merger	6
1.2 Optical layout of the LIGO interferometers	7
1.3 Strain sensitivity of the LIGO and Virgo Observatories	8
1.4 Example ambient ground motion spectrum	11
1.5 Schematic of the LIGO seismic isolation system	12
1.6 Sensor noise for the seismic isolation system	13
1.7 Performance of the ISI	15
2.1 Ground motion spectra during low and high winds	17
2.2 CAD rendering of the BRS	20
2.3 Side view of a CAD rendering of the BRS	20
2.4 Transfer function from platform tilt to measured tilt for the cBRS	22
2.5 Image of a BRS flexure	24
2.6 Close up view of the center of the CAD rendering of the BRS	25
2.7 Picture of an installed BRS	26
2.8 Schematic of a multi-slit autocollimator	27
2.9 Simulation of the BRS image analysis algorithm	29
2.10 Noise budget for the Beam Rotation Sensors	32
2.11 Representative amplitude spectral density showing the tilt subtraction during windy conditions	33
2.12 Time series showing tilt subtraction	34
2.13 Differential platform motion	35
2.14 Observed and modeled tilt vs wind speed	37
2.15 Duty cycle improvements for the LIGO Hanford Observatory	39
2.16 Duty cycle improvements for the LIGO Livingston Observatory	40
2.17 Expectation value of wind speed during GW events	41
3.1 Model of the performance of the current angular sensing and control system	42

3.2	Theoretical noise curves for the cBRS and seismometer pair	43
3.3	CAD rendering of the cBRS	45
3.4	Side view of the CAD rendering of the cBRS	46
3.5	CAD rendering of the cBRS kinematic mount	47
3.6	Diagram of the cBRS fiber interferometer read-head	48
3.7	Layout of the cBRS readout optics	49
3.8	Interference pattern of a cBRS fiber interferometer vs cavity length	51
3.9	CAD rendering of the cBRS mass adjuster	52
3.10	Demonstration of the effect of actuating the remote mass adjuster	53
3.11	Prototype cBRS noise performance	55
3.12	Noise models for the cBRS, a collection of seismometers, and two types of CPS	56
3.13	Projected rotational performance of Stage 2 of the ISI	58
3.14	Projected rotational performance of Stage 1 of the ISI	59
3.15	Projected translational performance of Stage 1 of the ISI	61
3.16	Projected translational performance of Stage 2 of the ISI	62
3.17	Comparison of the rotational isolation performance of Stage 2 during O2 and the projected performance with the inclusion of the cBRS	64
3.18	Comparison of the translational isolation performance during O2 and the projected performance with the inclusion of the cBRS	65
3.19	Projected performance of the angular sensing and control system	66
3.20	Comparison of the ASC performance with and without the cBRS	67
3.21	Projected low frequency strain noise with and without the cBRS	68
4.1	Observations of the seismic waves by instruments installed at the End-Y Station of LHO	71
4.2	Single station Rayleigh wave phase velocity measurements	74
4.3	The location of the cBRS during O2 alongside the array of seismometers . . .	78
4.4	Projected Newtonian noise subtraction with the array of seismometers	79
4.5	Transfer function between the cBRS and the strain output of the interferometer	80

DEDICATION

To Grace

ACKNOWLEDGMENTS

The author wishes .

The first observation showed ... that owing to the extreme sensitiveness of the instrument to vibrations, the work could not be carried on during the day. The experiment was next tried at night. ... so extraordinarily sensitive was the instrument that the stamping of the pavement, about 100 meters from the observatory, made the fringes disappear entirely!

If this was the case with the instrument constructed with a view to avoid sensitiveness, what may we not expect from one made as sensitive as possible!

Albert A. Michelson

*"The Relative Motion of the Earth and
the Luminiferous Ether"*

Chapter 1

INTRODUCTION

1.1 Gravitational Wave Theory

1.1.1 Linearized General Relativity

In the early twentieth century, the theory of General Relativity supplanted the static space-time, in which all prior physics was formulated, with a deformable space-time yielding a geometric explanation for gravity. This space-time is described by a unitless tensor field, $g_{\mu\nu}$, called the metric. The deformation of this metric follows the Einstein equation [1]:

$$R_{\mu\nu} - \frac{1}{2}R g_{\mu\nu} + \Lambda g_{\mu\nu} = \frac{8\pi G}{c^4} T_{\mu\nu} \quad (1.1)$$

where $R_{\mu\nu}$ is the Riemann tensor, R is the Ricci scalar, Λ is the cosmological constant, G is the gravitational constant, c is the speed of light, and $T_{\mu\nu}$ is the stress energy tensor.

If one focuses on a locally-flat region of space which is much smaller than the scale of the universe, then the cosmological constant term is negligible and the metric can be approximated via [2]:

$$g_{\mu\nu}(\vec{x}, t) \approx \eta_{\mu\nu}(\vec{x}, t) + h_{\mu\nu}(\vec{x}, t) \quad (1.2)$$

where $\eta_{\mu\nu}$ is the flat Minkowski metric and $h_{\mu\nu}$ is a small perturbation¹, $|h_{\mu\nu}| \ll 1$. Applying the Einstein equation and transferring to a transverse-traceless coordinate system yields the wave equation:

$$\square h_{\mu\nu} = -\frac{16\pi G}{c^4} T_{\mu\nu} \quad (1.3)$$

For a complete derivation see Reference [2]. Vacuum solutions propagating along the

¹The largest amplitude of gravitational wave strain measured thus far is on the order of $|h_{\mu\nu}| \approx 10^{-21}$ [3]

z-axis can readily be found as:

$$h_{ij}(t, x) = \begin{pmatrix} h_+ & h_\times & 0 \\ h_\times & -h_+ & 0 \\ 0 & 0 & 0 \end{pmatrix} \cos(\omega t - \kappa z) \quad (1.4)$$

where h_+ and h_\times are the amplitudes in the “plus” and “cross” polarizations², ω is the angular frequency of oscillation, and κ is the wavenumber. Here i and j run from 1 to 3 and correspond to the three spatial coordinates. The time components are suppressed as the $h_{0\nu}$ components are zero due the coordinate choice and h_{00} is zero outside the source.

In the long wavelength limit, a source of gravitational waves can be decomposed into a sum of momenta of the stress-energy tensor:

$$h_{ij}(t, x) = \frac{1}{r} \frac{4G}{c^4} \Lambda_{ij,kl} \left(S^{kl} + \frac{1}{c} n_m \dot{S}^{kl,m} + \frac{1}{2c^2} n_m n_p \ddot{S}^{kl,mp} + \dots \right)_{\text{ret}} \quad (1.5)$$

where $\Lambda_{ij,kl}$ is the projection from the source frame to transverse-traceless coordinates and the momenta are defined as:

$$S^{ij}(t) = \int T^{ij}(t, \mathbf{x}) d^3x \quad (1.6)$$

$$S^{ij,k}(t) = \int T^{ij}(t, \mathbf{x}) x^k d^3x \quad (1.7)$$

$$S^{ij,kl}(t) = \int T^{ij}(t, \mathbf{x}) x^k x^l d^3x \quad (1.8)$$

with the subscript “ret” denoting the evaluation at retarded time. The leading term of Equation 1.5 can be expressed in terms of the mass quadrupole moment of the source, Q_{ij} , as:

²A massless graviton is assumed. A massive graviton would yield five polarizations instead of two. Current graviton mass constraints are $m_g \leq 4.7 \times 10^{-23} eV/c^2$ [4]

$$h_{ij}(t, x) = \frac{1}{r} \frac{2G}{c^4} \ddot{Q}_{ij}(t - r/c) \quad (1.9)$$

Thus the emission of gravitational waves is primarily driven by time varying quadropole moments. Varying higher order moments will also emit gravitational waves but are subdominant in most natural systems.³

1.1.2 Compact Binary Coalescence

As of writing, the only systems that have been observed to emit gravitational waves are composed of two compact⁴ astrophysical objects orbiting a common center of mass, so-called compact binaries. These objects could be neutron stars, as with the Hulse-Taylor binary pulsar[6], GW170817[7], and GW190425[8], or black holes like GW150914[3] and most events in the GWTC-1[9].

Such a system can be approximated as two point masses, $m_{1,2}$, in a Keplerian orbit which decays due to the emission of gravitational waves. This approximation is only valid during the inspiral phase of the merger when the distance between the two objects is much larger than the size of the objects. For a complete simulation of the gravitational wave emission during a merger, one must numerically compute the evolution of the space-time around the objects. [10]

The gravitational waves emitted under the point-mass approximation follow:

$$h_+(t) = \frac{4}{r} \left(\frac{GM}{c^2} \right)^{5/3} \left(\frac{\pi f}{c} \right)^{2/3} \frac{1 + \cos^2 \theta}{2} \cos(\omega t + \phi) \quad (1.10)$$

$$h_\times(t) = \frac{4}{r} \left(\frac{GM}{c^2} \right)^{5/3} \left(\frac{\pi f}{c} \right)^{2/3} \cos \theta \sin(\omega t + \phi) \quad (1.11)$$

³GW190412 [5], a high mass-ratio binary system, is the only observation to contain contributions from higher moments.

⁴The compactness of the objects is of importance only to satisfy a point-mass approximation and to allow observation in current instruments. Non-compact objects such as white and brown dwarfs will emit gravitational waves in their inspiral phase but merge due to Roche lobe overflow long before entering the frequency band accessible today.

where $M = (m_1 m_2)^{3/5} / (m_1 + m_2)^{1/5}$ is the “chirp mass”, r is the distance from the observer to the center of mass of the source, θ is the viewing angle with respect to the axis of the orbital plane, $f = \omega / 2\pi$ is the frequency of oscillation, and ϕ is the initial phase of the system.

The emission of gravitational waves carry energy away from the system and thus the orbit must decay. As the radius of the orbit decreases, the frequency of oscillation must grow due to Kepler’s law. This then causes the amplitude of the emitted gravitational waves to grow and decay of the orbit to quicken. The frequency change during this runaway process can be shown to be:

$$\dot{f} = \frac{96}{5} \pi^{8/3} \left(\frac{GM}{c^3} \right)^{5/3} f^{11/3} \quad (1.12)$$

This process produces a characteristic “chirp” signal which begins at low frequency and low amplitude then grows in amplitude while shifting to higher frequency. The signal culminates in a final sharp increase in both frequency and amplitude before the objects merge. This can be seen in Figure 1.1 which shows a spectrogram of the observed strain at the LIGO observatories of the binary neutron star merger GW170817.

Although binary systems are the topic of choice here, many other systems should theoretically emit gravitational waves. These can range from asymmetric spinning stars [11] and supernovae [12] to cosmic strings [13] and density perturbations in the early universe [14]. With the measurement of gravitational waves, humankind has technologically expanded our senses to include the faint vibrations of space-time. This ability has allowed the study of new types of astronomical systems and may one day allow further insight into the beginning of the universe and the nature of gravity.

1.2 *LIGO*

1.2.1 *Sensitivity*

The Laser Interferometric Gravitational wave Observatory (LIGO) [15] is a pair of 4-km-long L-shaped interferometric gravitational wave detectors, one located in Hanford, Washington

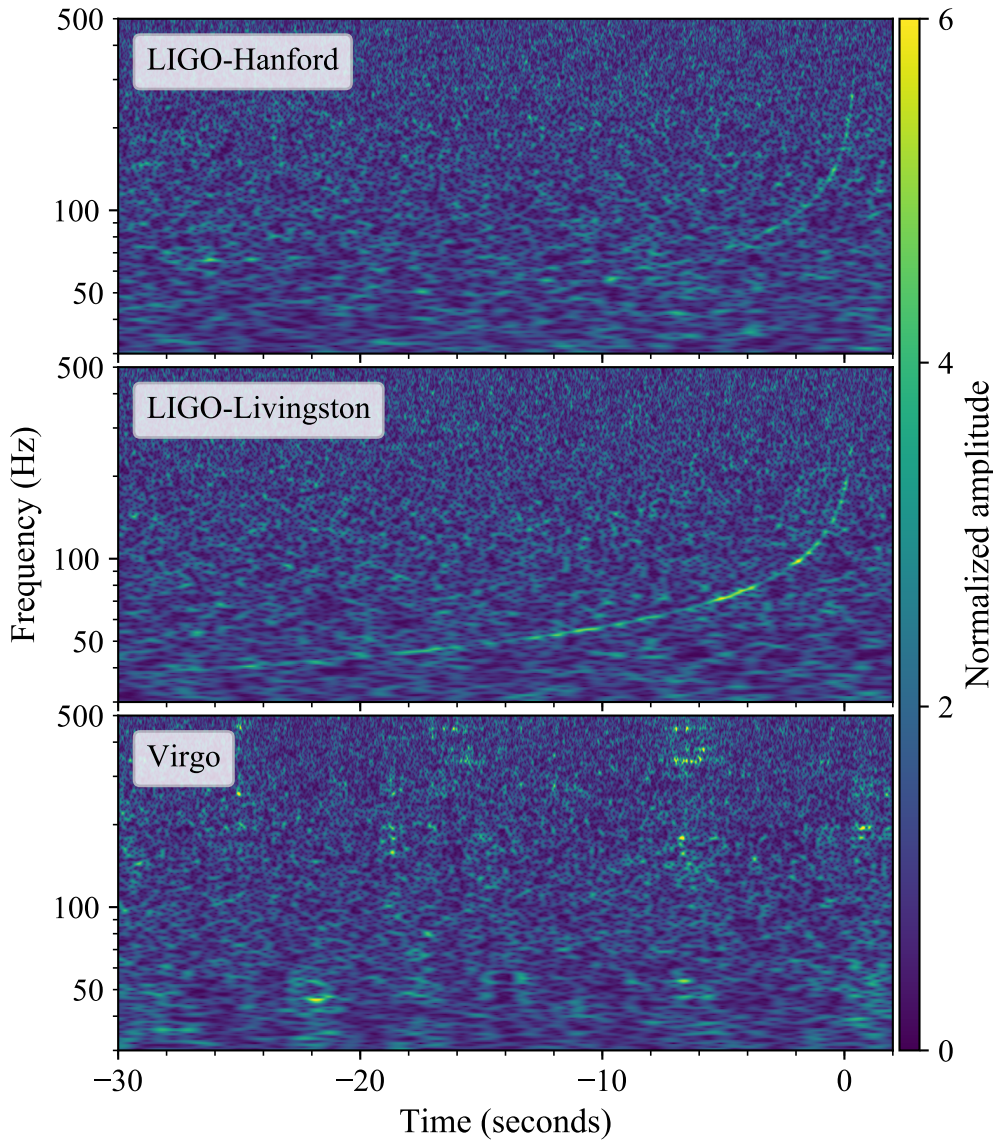


Figure 1.1: Spectrogram of the strain caused by a binary neutron star merger as seen at the LIGO Hanford Observatory, LIGO Livingston Observatory, and the Virgo Observatory. [7] A clear chirp signal can be seen starting at ~ 40 Hz which rises in both frequency and amplitude. The origin of the time axis is the time at which the neutron stars merge. The differing amount of signal in the three detectors is due to the alignment of their respective antenna-patterns with the source location.

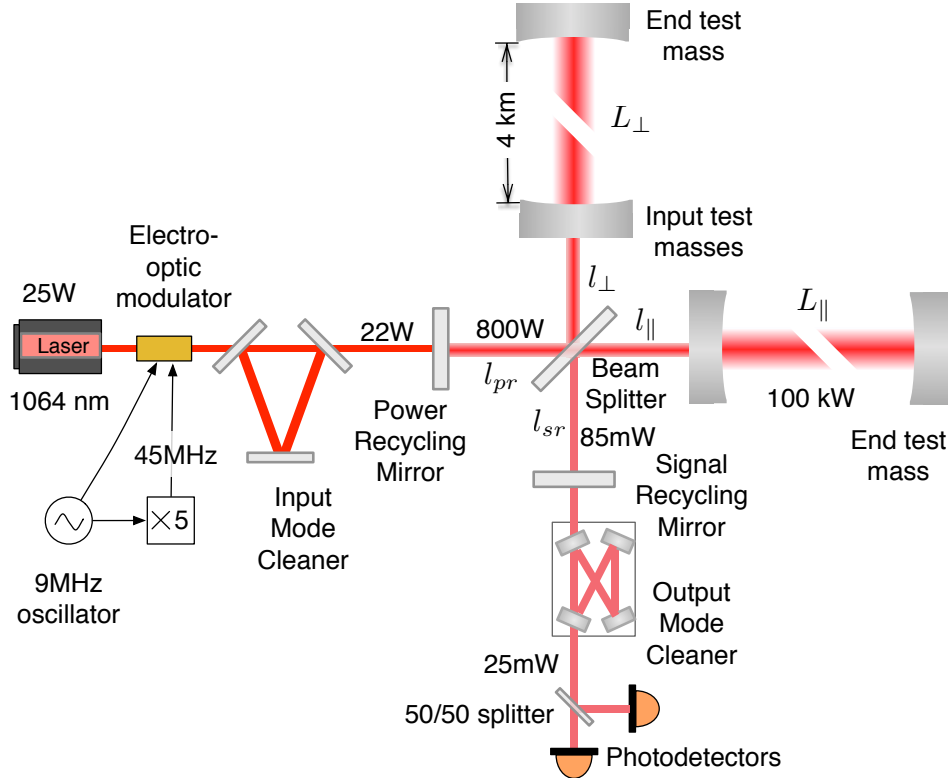


Figure 1.2: Optical layout of the LIGO interferometers [16].**check copyrights**

(LHO) and the other in Livingston, Louisiana (LLO). Each observatory is a dual-recycled Fabry-Perot Michelson interferometer which measures the differential strain between its two arms formed by pairs of partially reflective mirrors, also called test masses.

As a gravitational wave passes the observatory, the arms experience strains that follow [2]:

$$h_{xx} = h_+ (\cos^2 \theta \cos^2 \phi - \sin^2 \phi) + 2 h_x \cos \theta \sin \phi \cos \phi \quad (1.13)$$

$$h_{yy} = h_+ (\cos^2 \theta \sin^2 \phi - \cos^2 \phi) - 2 h_x \cos \theta \sin \phi \cos \phi \quad (1.14)$$

$$h = \frac{1}{2}(h_{xx} - h_{yy}) = \frac{1}{2}h_+ (1 + \cos^2 \theta) + h_x \cos \theta \sin 2\phi \quad (1.15)$$

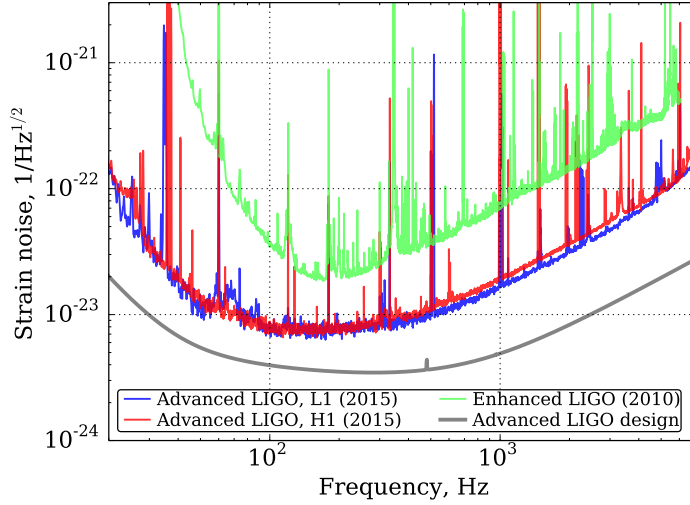


Figure 1.3: Strain sensitivity of the LIGO and Virgo Observatories. **replace with O3 sensitivity**

where h_{xx} and h_{yy} are the strains along the x and y arms respectively, θ and ϕ are the polar and azimuthal angles of the direction of propagation, and h is the differential strain as measured by the observatory. Here the polarizations are defined in the source frame.

The series of optics allows the observatory to measure differential strains down to 7×10^{-24} at 200 Hz. Noise curves for the observatories are shown in Figure 1.3 where one can see that the sensitive band of the observatory runs from 20 Hz up to 7 kHz. At low frequencies the noise is dominated by residual control noise, discussed in Section 3.1, while at high it is dominated by noise caused by quantum fluctuations. [17]

1.2.2 Events

With LIGO's current sensitivity, the primary systems of interest are compact binaries, discussed in Section 1.1.2, which merge within the band of interest. An equal mass $50 M_\odot$ binary black hole system would merge at ~ 22 Hz while a $1.4 M_\odot$ binary neutron star system merges at ~ 800 Hz yet emits appreciably while sweeping through the LIGO band.

During the first and second observing runs of LIGO, ten binary black hole systems and

one binary neutron star merger were detected with high significance. [9] The black hole binaries ranged in total mass from $18.6 M_{\odot}$ to $84.4 M_{\odot}$ and merged at distances from 320 Mpc to 2.8 Gpc. The neutron star binary had component-masses of $1.27 M_{\odot}$ and $1.46 M_{\odot}$ and merged at 40 Mpc. These systems are tabulated in Table 1.2.2.

Event Name	m1 (M_{\odot})	m2 (M_{\odot})	M_f (M_{\odot})	Distance (Mpc)	z
GW150914	$35.6^{+4.7}_{-3.1}$	$30.6^{+3.0}_{-4.4}$	$63.1^{+3.4}_{-3.0}$	440^{+150}_{-170}	$0.09^{+0.03}_{-0.03}$
GW151012	$23.2^{+14.9}_{-5.5}$	$13.6^{+4.1}_{-4.8}$	$35.6^{+10.8}_{-3.8}$	1080^{+550}_{-490}	$0.21^{+0.09}_{-0.09}$
GW151226	$13.7^{+8.8}_{-3.2}$	$7.7^{+2.2}_{-2.5}$	$20.5^{+6.4}_{-1.5}$	450^{+180}_{-190}	$0.09^{+0.04}_{-0.04}$
GW170104	$30.8^{+7.3}_{-5.6}$	$20.0^{+4.9}_{-4.6}$	$48.9^{+5.1}_{-4.0}$	990^{+440}_{-430}	$0.20^{+0.08}_{-0.08}$
GW170608	$11.0^{+5.5}_{-1.7}$	$7.6^{+1.4}_{-2.2}$	$17.8^{+3.4}_{-0.7}$	320^{+120}_{-110}	$0.07^{+0.02}_{-0.02}$
GW170729	$50.2^{+16.2}_{-10.2}$	$34.0^{+9.1}_{-11.1}$	$79.5^{+14.7}_{-10.2}$	2840^{+1400}_{-1360}	$0.49^{+0.19}_{-0.21}$
GW170809	$35.0^{+8.3}_{-5.9}$	$23.8^{+5.1}_{-5.2}$	$56.3^{+5.2}_{-3.8}$	1030^{+320}_{-390}	$0.20^{+0.05}_{-0.07}$
GW170814	$30.6^{+5.6}_{-3.0}$	$25.2^{+2.8}_{-4.0}$	$53.2^{+3.2}_{-2.4}$	600^{+150}_{-220}	$0.12^{+0.03}_{-0.04}$
GW170817	$1.46^{+0.12}_{-0.10}$	$1.27^{+0.09}_{-0.09}$	≤ 2.8	40^{+7}_{-15}	$0.01^{+0.00}_{-0.00}$
GW170818	$35.4^{+7.5}_{-4.7}$	$26.7^{+4.3}_{-5.2}$	$59.4^{+4.9}_{-4.8}$	1060^{+420}_{-380}	$0.21^{+0.07}_{-0.07}$
GW170823	$39.5^{+11.2}_{-6.7}$	$29.0^{+6.7}_{-7.8}$	$65.4^{+10.1}_{-7.4}$	1940^{+970}_{-900}	$0.35^{+0.15}_{-0.15}$
GW190412	$29.7^{+5.0}_{-5.3}$	$8.4^{+1.7}_{-1.0}$	$37.0^{+4.1}_{-3.9}$	730^{+140}_{-170}	$0.15^{+0.03}_{-0.03}$
GW190425	$1.60 - 1.87$	$1.46 - 1.69$	$3.4^{+0.3}_{-0.1}$	159^{+69}_{-71}	$0.03^{+0.01}_{-0.02}$

The recently completed third observing run has had 56 significant candidates [18]. Although these candidates have not been verified to be true gravitational wave events, they show a significant increase in rate of detection due to both the decreased noise and increased duty cycle achieved for the third observing run. Two of these candidates have been confirmed to be true gravitational wave events: GW190412 [5] a binary black hole merger with asymmetric component-masses and GW190425 [8] a binary merger with total mass of $\sim 3.4 M_{\odot}$

Observation of gravitational waves has led to further understanding of a variety of phenomena including the nature of the neutron star composition [19], the source of heavy el-

ements [20], and black hole populations [9]. Additionally, they have allowed a model independent measurement of Hubble’s constant [21, 22] and have set restrictive constraints on alternative theories of gravity [23].

1.3 Seismic Isolation

1.3.1 LIGO Isolation Scheme

To operate interferometric observatories that are sensitive to the strains of space-time, one must isolate the instrument from all other sources of differential displacement. As the observatories are located on the surface of the earth, the dominant source of such noise is ambient seismic motion.

The ambient seismic wave-field, measurements of which are shown in Figure 1.4, is continuously excited across a wide frequency range. Between 50 mHz and 1 Hz the ambient spectrum is dominated by the “microseism”, an always-present feature sourced by the Earth’s oceans. Above 1 Hz, the dominant source of seismic motion at the observatories is due to local activity. Yet even in locations without anthropogenic sources, the ground moves at these frequencies. Without isolation, this motion would dominate any measurements with the interferometer and, more practically, would disrupt any attempt to operate the interferometer at its ideal alignment. This ideal alignment is referred to as having the interferometer “locked”.

The LIGO observatories solve this issue by employing a multi-stage seismic isolation system formed of both passive and active stages. [24] First from the ground is the Hydraulic External Pre-Isolation (HEPI) system which is formed by four hydraulic actuators. This provides a factor of ~ 100 isolation at high frequencies and allows for correction of tidal effects. Suspended from this is the Internal Seismic Isolation (ISI) system⁵, described in Section 1.3.2. This is a dual-stage six-degree active isolation system and is the primary broad-band isolation. From the second stage of the ISI is hung a quadruple pendulum, at

⁵LIGO employs two versions of the ISI: the HAM-ISI for the auxiliary optics and the BSC-ISI for the core optics. Here ISI refers to the BSC-ISI as rotation sensors have only been deployed on BSC-ISIs.

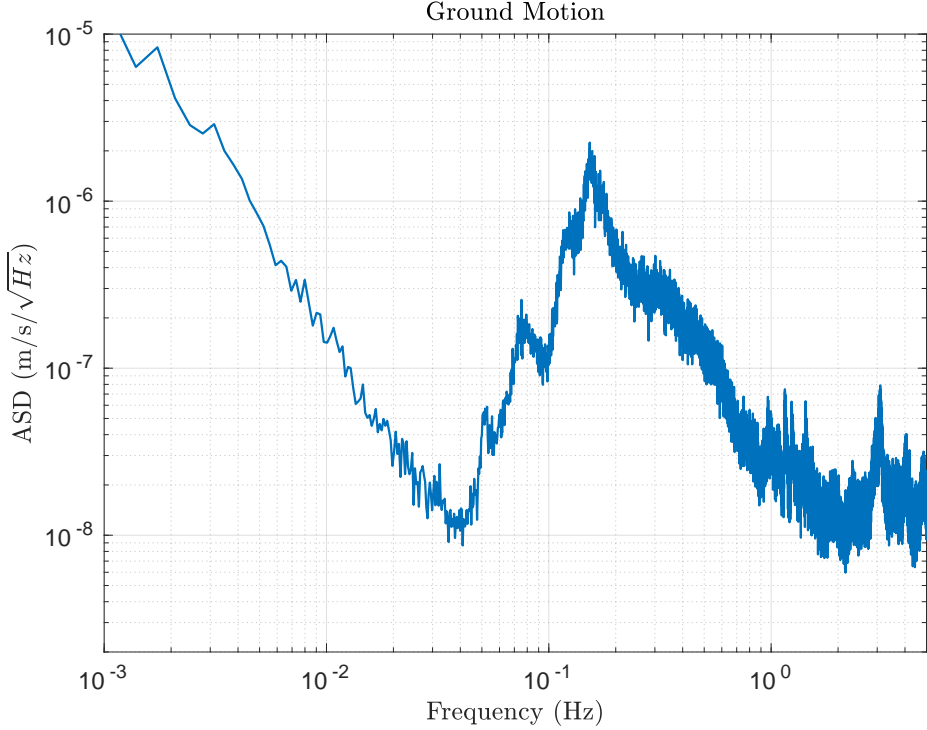


Figure 1.4: Example ambient horizontal ground motion spectrum recorded at the End-X station of the LIGO Hanford Observatory. From 40 mHz to 1 Hz the spectrum is dominated by the oceanic microseism while above 1 Hz the seismic motion is sourced by local anthropogenic activity. Below 40 mHz, the instrument is dominated by tilt contamination described in Section 2.1.1

the bottom of which is a test mass. This provides high frequency passive isolation that attenuates the motion of the test mass by $1/f^8$, where f is the frequency of the motion.

1.3.2 Internal Seismic Isolation

The ISI is comprised of two similar stages each suspended from steel blade springs and wires. The first (Stage 1) is suspended from HEPI (Stage 0) and the second (Stage 2) from the first. Each stage is controlled by a set of six magnetic actuators whose feedback signal is comprised of a collection of sensors. The motion of the table is sensed with a series of

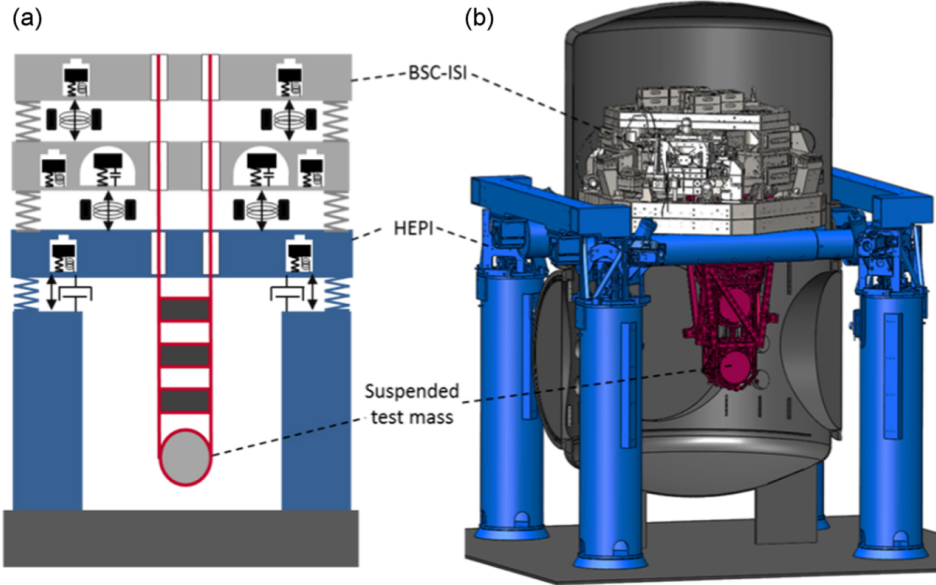


Figure 1.5: Schematic of the LIGO seismic isolation system. [24]

seismometers which are sensitive to motion with respect to an inertial frame. On the first stage, two separate models of seismometers are combined to obtain the lowest noise in a given frequency band. Sarcelles L4Cs are used above 0.5 Hz, while below this Trillium T240s are employed. These two sensors are “blended” together by sending the T240 through a low pass filter and the L4C through a high pass. The filtered signals are added together to form a low-noise broad-band inertial sensor combination. The second-stage utilizes Geotech GS13s as its inertial sensors.

The inertial motion of the platform is sensed in all six degrees of freedom using three independent seismometers of each type located 1-meter apart. The three translational signals are composed from the average of the corresponding seismometer signals, while the three rotational degrees are sensed using the difference of the motion divided by the separation.

Due to the increased T240 noise below 500 mHz, a set of Capacitive Position Sensors (CPS) are deployed to detect the relative motion between either Stage 0 and the first ISI stage or the two stages of the ISI. This is then used as the control signal at low frequencies

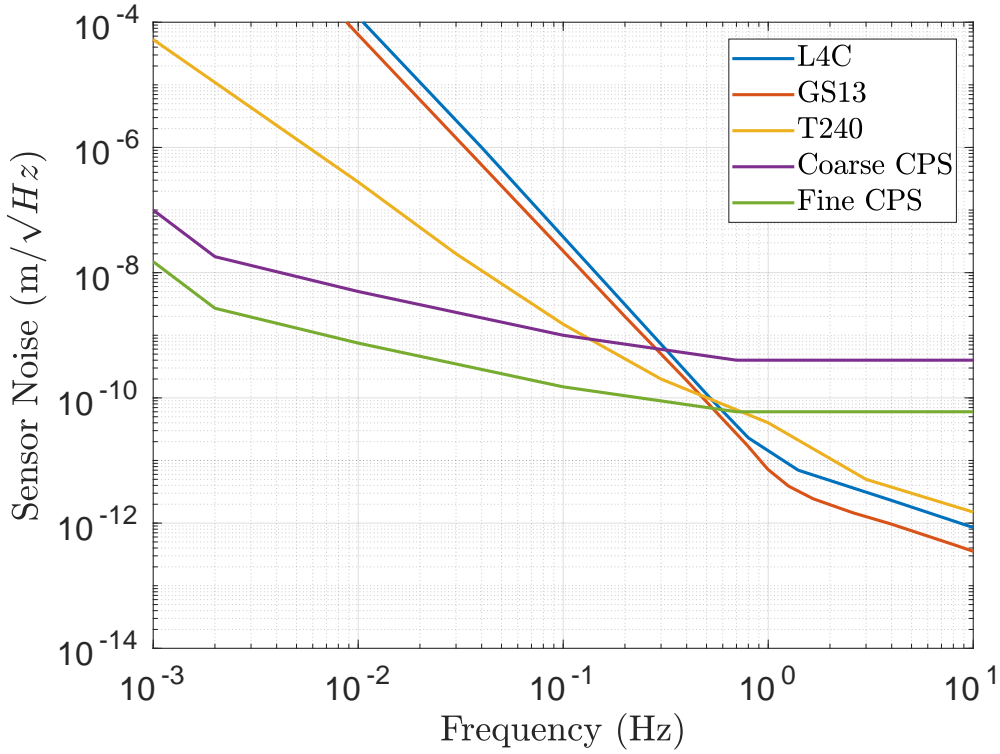


Figure 1.6: Sensor noise for the collection of sensors used on the ISI.

yielding a control for Stage 1 that follows:

$$x_{\text{cont}} = F_{LP} (x_p - x_g)_{\text{CPS}} + F_{BP} x_{p, \text{T240}} + F_{HP} x_{p, \text{GS13}} \quad (1.16)$$

where x_{cont} is the control signal, $x_{p,i}$ is the platform motion sensed by the respective sensor, x_g is the ground motion, and F_{LP} , F_{BP} , F_{HP} are respectively a low-pass, band-pass, and high-pass filter. When this signal is utilized in feedback, the residual motion of the platform can be approximated by:

$$x_p(f) \approx F_{LP} (x_g(f) + n_{\text{CPS}}(f)) + F_{BP} n_{\text{T240}}(f) + F_{HP} n_{\text{GS13}}(f) \quad (1.17)$$

where $n_i(f)$ is the sensor noise spectrum for the relevant sensor. This approximation ignores tilt-to-horizontal coupling which is addressed in Section 2.1.

1.3.3 Sensor Correction

The isolation can be further improved with the addition of a three-axis seismometer, in this case a Struckheisen STS-2, placed on the floor of the observatory. This measures the ground motion and can be used to do “sensor correction”. Sensor correction is the procedure of subtracting the ground contribution of the CPS signal to recover the low frequency platform motion. The CPS signal in this case becomes:

$$x_{CPS} = F_{LP} (x_p - x_g) + F_{SC} x_g \quad (1.18)$$

where F_{SC} is the “sensor correction” filter which has a pass-band that overlaps the CPS low pass filter. This can be rearranged to give:

$$x_{CPS} = \tilde{F}_{LP} (x_p - x_g) + \tilde{F}_{HP} x_p \quad (1.19)$$

where the tildes denote the relevant combination of F_{LP} and F_{SC} that yield effective low-pass and high-pass filters. This scheme allows for isolation down to 100 mHz and decreases the bleed-through of the ground motion due to the CPS low-pass filter’s finite roll-off. Below 10 mHz, both the ground and platform seismometers are dominated by tilt contamination which is addressed in Section 2.1. The performance of the seismic isolation system can be seen in Figure 1.7.

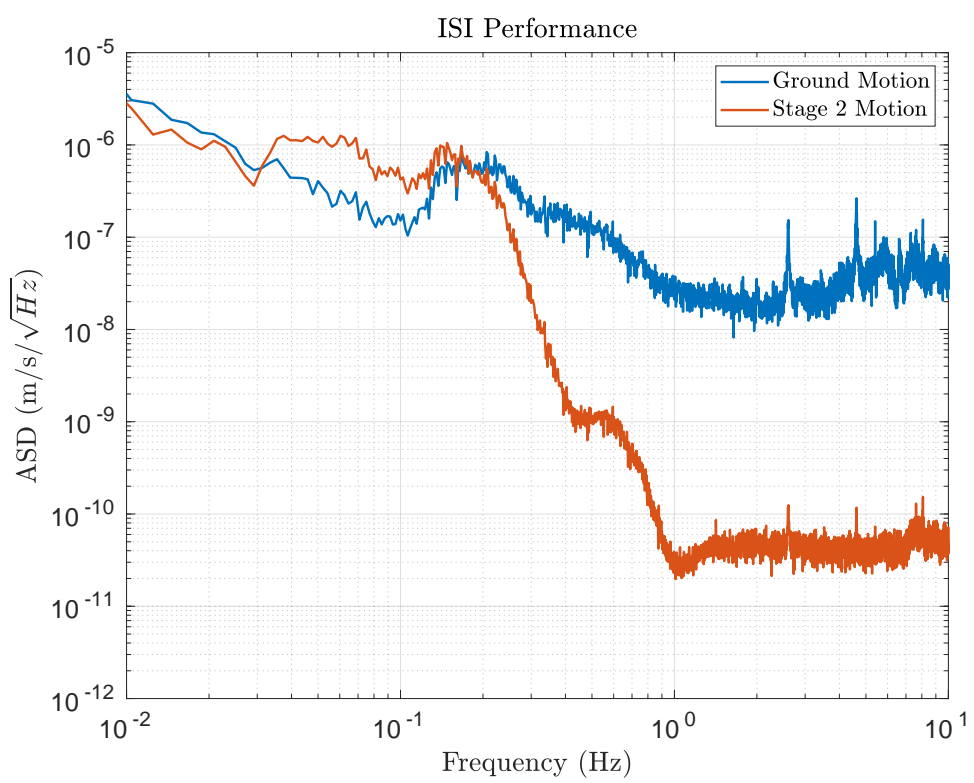


Figure 1.7: Performance of the ISI as measured by the GS13 installed on Stage 2.

Chapter 2

1-METER SCALE GROUND ROTATION SENSORS

2.1 *Ground Tilt*

2.1.1 *Tilt Contamination*

At their core, seismometers are low frequency spring-mass systems that measure the difference in motion between the casing and the device’s proof mass. Above the resonant frequency of the spring-mass system, this difference measures the motion of the casing with respect to an inertial frame. Over the past century this technology has produced devices that are sensitive to ~ 0.1 nm/s down to ~ 10 mHz. However, these systems are intrinsically susceptible to any stray forces that act on the proof mass.

Of interest here is the contamination due to the rotation of the device within a external gravitational field, namely the field caused by the Earth. The rotation with respect to a fixed gravitational force will be referred to as “tilt”.¹ From the proof mass’s frame, a tilt is equivalent to a rotation of the gravitational force. This yields a horizontal acceleration of:

$$a = g \sin(\theta)$$

where g is the gravitational acceleration on the surface of the earth and θ is the angle by which the device is tilted. This acceleration adds a second term to the seismometer’s output shown below for small angles and in the Fourier domain:

$$\tilde{x}_{seis}(\omega) = \tilde{x}_{trans}(\omega) + \frac{g}{\omega^2} \tilde{\theta}(\omega)$$

¹Although a subtle difference, the distinction would be of great consequence if the local gravitational field were to vary rapidly. In that case the sensors described in Sections 2.2 and 3.2 would be of little use as the sense inertial rotations not tilts with respect to gravity.

where \tilde{x}_{seis} is the seismometer's output in displacement units, \tilde{x}_{trans} is the translational motion of the device, and ω is the angular frequency.

With this additional contribution, it is clear that, for a given amplitude of tilt, the contamination term contributes more at lower frequencies and can readily dominate the translational signal. In the context of the ground seismometers at the observatory, the tilt signal exceeds the translational component below ~ 100 mHz. Above this frequency, the seismometer signal is dominated by the ever-present oceanic microseism. This can be seen in Figure 2.1 which shows the translation amplitude spectral density measured by a ground seismometer at LHO during both low and high wind conditions.

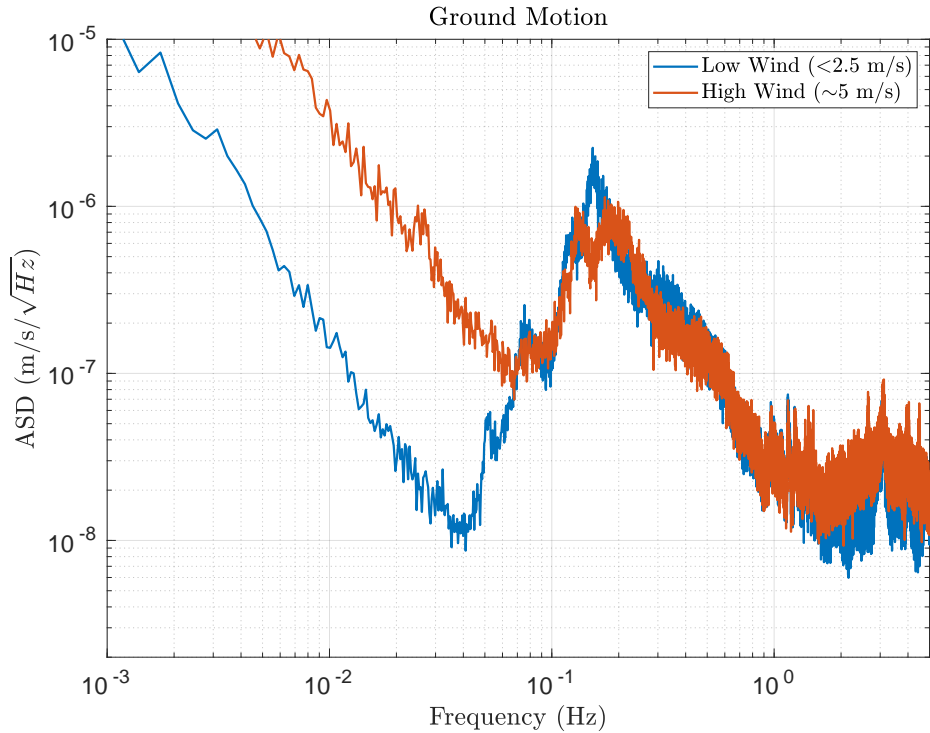


Figure 2.1: Ground motion spectra recorded at the X-End Station of the Hanford Observatory during low and high winds. Below 100 mHz, wind driven tilts become dominant during high winds. From 100 mHz to 1 Hz the spectra are dominated by the oceanic microseism while above 1 Hz the seismic motion is sourced by local anthropogenic activity.

The dominant driver of ground tilts at the observatories is wind acting on the walls of the building. Although one might naively assume that the wind would rigidly rotate the building, the true mechanism is deformation of the concrete slab caused by differential pressure on the walls of the building. This increases the noise seen by the ground seismometer during high winds. The primary consequence of this excess is that the interferometer could not remain locked during high wind speeds. Additionally, due to nonlinear deformation of the floor, tilts measured in one location can not be simply extrapolated from the tilts measured at a different location.

2.1.2 Sensor Correction with Tilt Subtraction

Several different schemes, in principle, can combat such a contamination. The most straight-forward is to decrease the effect of wind by designing buildings that interact with the wind less or by installing wind blocks such as wind fences or earthen berms. Both of these options require significant construction and, for the case of LIGO, tilt contamination was not addressed in the observatories construction. Another option is to build seismometers that are suspended in such a way that they do not experience tilts. This is an active area of research and may one day yield tilt-free seismometers. [25]

The approach that will be explored here is to measure the tilt with an independent inertial rotation sensor, described in Section 2.2, and subtract the wind-driven contribution. This would then yield a corrected channel with the following form:

$$\tilde{x}_{seis}(\omega) = \tilde{x}_{trans}(\omega) + \frac{g}{\omega^2} \tilde{\theta}(\omega) \quad (2.1)$$

$$- \frac{g}{\omega^2} \tilde{\theta}_{meas}(\omega) \quad (2.2)$$

where $\tilde{\theta}_{meas}$ is the tilt seen by the rotation sensor. Given a subtraction factor of α between the tilt component of the seismometer and rotation sensors this yields the following:

$$\tilde{x}_{seis}(\omega) = \tilde{x}_{trans}(\omega) + \frac{g}{\omega^2} (1 - \alpha) \tilde{\theta}(\omega)$$

Current installations have yielded an $\alpha \sim 0.9$. This yields a ground motion measurement with low tilt contamination which can be used within the seismic isolation system. As this correction decreases noise primarily at low frequencies, the feedback filters deployed within the isolation system can be tuned to cross over at a lower frequency away from the microseism. At the cross-over frequency, the filters have large gain and phase changes that degrade performance. Placing this cross-over below the microseism frequencies decreases the effects of this “gain peaking” and allows for isolation at lower frequencies. For more details see Reference [26].

2.2 Beam Rotation Sensors

2.2.1 Mechanical System

A Beam Rotation Sensor (BRS) is a beam-balance based inertial rotation sensor comprised of a 1-m long beam hung from two 10-15 μm thick beryllium-copper flexures, described in Section 2.2.2. Figure 2.3 shows a CAD model of the beam-balance.

This design makes the beam stiff in all degrees of freedom other than rotation around the horizontal axis which intersects the two pivot-points. This forms a system consisting of two elementary subsystems: a rotational spring-mass system formed by the stiffness of the flexures, and a simple pendulum due to the offset of the pivot point and the center of mass. This is then described by the following equation of motion: [27]

$$I\ddot{\theta} + \gamma\dot{\theta} + \kappa(1 + \frac{i}{Q})(\theta - \theta_p) + Mg\delta\theta + M\delta\ddot{x}_p = \tau_{ex} \quad (2.3)$$

where θ and θ_p are, respectively, the angle of beam and the platform with respect to gravitational vertical, τ_{ex} is the sum of all exterior torques, I is the moment of inertia, Q is the intrinsic quality factor, γ is the velocity damping factor, κ is the spring constant of the flexures, M is the mass of the balance, g is the gravitational acceleration, δ is the vertical distance from the center of mass and the pivot point, and x_p is the translation of the platform. Equation 2.3 can be rearranged to yield:

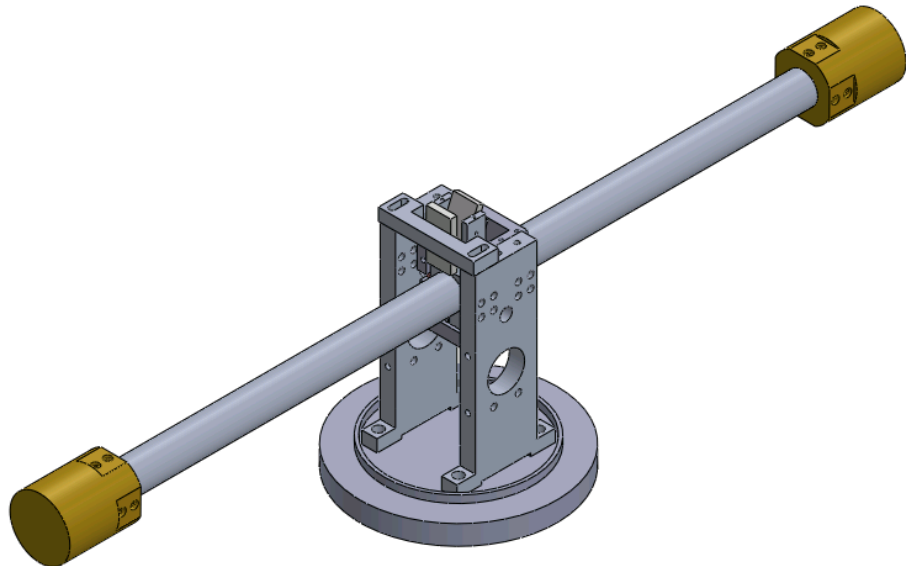


Figure 2.2: CAD rendering of the BRS with the vacuum and optical readout systems omitted. The beam with its two brass end masses can be seen along with its attached mirrors and support structure.

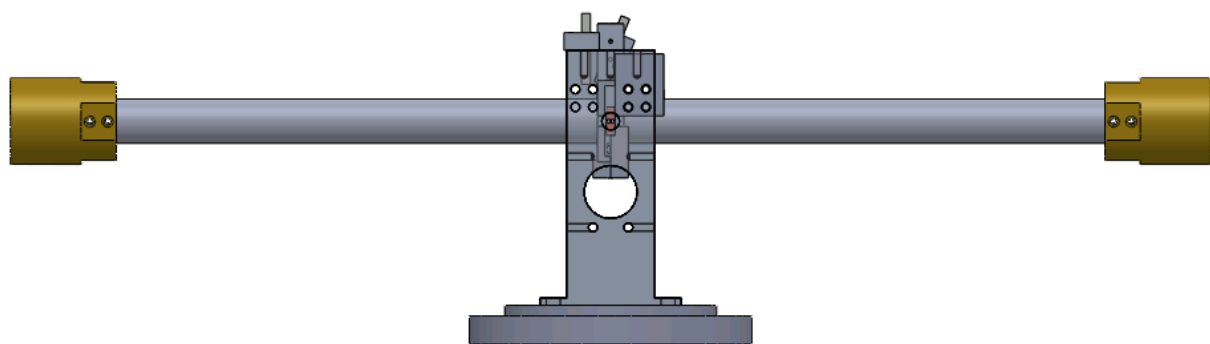


Figure 2.3: Side view of a CAD rendering of the BRS. At center, one of the copper colored flexures can be seen. The other is mounted on the opposite side.

$$\tilde{\theta} = -\frac{\tilde{\tau}_{ex} + \omega^2 M \delta \tilde{x}_p + \kappa(1 + i/Q)\tilde{\theta}_p}{I\omega^2 - i\gamma\omega - i\kappa/Q - \kappa - Mg\delta} \quad (2.4)$$

where ω is the frequency of motion and tildes denote spectral amplitudes. For the BRSs, the quantity of interest is not the angle of the beam but the difference in angle between the beam and the platform. Thus the angle that is recorded by the readout follows:

$$\tilde{\theta}_a = \tilde{\theta} - \tilde{\theta}_p \quad (2.5)$$

$$= -\frac{\tilde{\tau}_{ex} + \omega^2 M \delta \tilde{x}_p + \kappa(I\omega^2 - i\gamma\omega - Mg\delta)\tilde{\theta}_p}{I\omega^2 - i\gamma\omega - i\kappa/Q - \kappa - Mg\delta} \quad (2.6)$$

where $\tilde{\theta}_a$ is the recorded angle. This equation can be broken up into three distinct terms: the angular motion due to external torques, $\tilde{\theta}_\tau$, due to translational coupling, $\tilde{\theta}_x$, and due to rotation of the platform, $\tilde{\theta}_s$.

$$\tilde{\theta}_a = \tilde{\theta}_\tau + \tilde{\theta}_x + \tilde{\theta}_s \quad (2.7)$$

$$\tilde{\theta}_\tau = -\frac{\tilde{\tau}_{ex}}{I} \frac{1}{\omega^2 - i(\omega_0\omega/q + \omega_0^2/Q) - (\omega_0^2 + \omega_g^2)} \quad (2.8)$$

$$\tilde{\theta}_x = -\tilde{x}_p \frac{M\delta}{I} \frac{\omega^2}{\omega^2 - i(\omega_0\omega/q + \omega_0^2/Q) - (\omega_0^2 + \omega_g^2)} \quad (2.9)$$

$$\tilde{\theta}_s = -\tilde{\theta}_p \frac{\omega^2 - i\omega_0\omega/q - \omega_g^2}{\omega^2 - i(\omega_0\omega/q + \omega_0^2/Q) - (\omega_0^2 + \omega_g^2)} \quad (2.10)$$

Where $\omega_0 = \sqrt{k/I}$ is the resonant frequency, $\omega_g = \sqrt{Mg\delta/I}$, and q is the quality factor due to velocity damping. These equations illuminate the fact that the beam has a resonance at $\omega = \sqrt{\omega_0^2 + \omega_g^2}$ and $\tilde{\theta}_s$ has a zero at $\omega = \omega_g$.

To allow for high fidelity rotation sensing, the translational coupling must be negligible at the frequencies of interest. To achieve this, δ must be tuned close to zero. This is achieved firstly through the design of the beam's suspension which places the center of mass close to the pivot point. Fine adjustments are then made by adding mass to the beam above

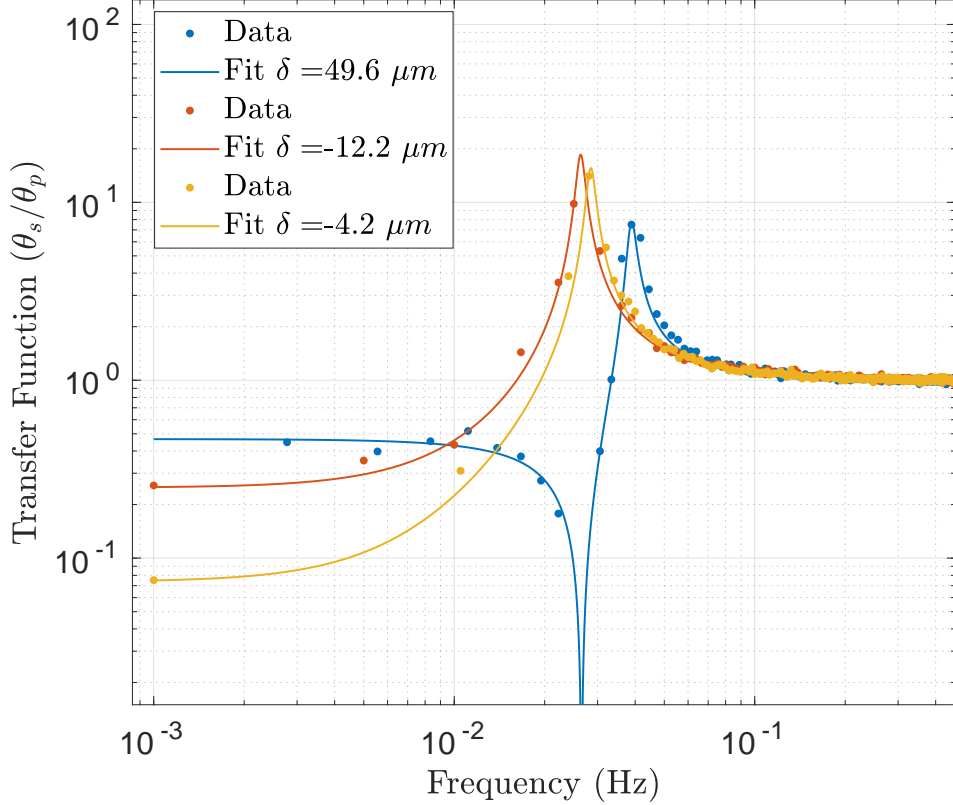


Figure 2.4: Measurements of the transfer function from platform tilt to measured tilt for the cBRS along with fits to Equation 2.10. After each measurement mass was added or removed from the top of the proof mass in order to shift the vertical position of its center of mass.

or below the pivot. These adjustments are guided by measurements of the zero in the $\tilde{\theta}_s$ transfer function, Equation 2.10, at $\omega = \omega_g$. Figure 2.4 shows this for the cBRS, described in Chapter 3. Differing amounts of tuning were achieved for each deployed device described in Section 2.3 due to scheduling constraints. The lowest translation coupling was achieved at the LHO End-Y BRS which had a $\delta < 0.5 \mu\text{m}$ yielding a translational coupling of less than 10^{-6} rad/m .

2.2.2 Flexures

The flexures which suspend the proof mass are cut out of $1/4'' \times 1/4'' \times 7/8''$ blocks of beryllium-copper by wire electrical discharge machining to yield the shape shown in Figure 2.2.2. Circular cuts were used to achieve a well defined pivot point. The opening gaps on either side were restricted to act as mechanical stops for ease of handling and transportation.

Due to machining variability in the width of flexure, batches of flexures were assayed via a microscope to determine the width of each flexure and to identify flexures that were damaged during machining and transportation. Pairs of flexures with similar widths were installed together, one on either side of the beam. Each flexure has one half clamped to the support and the other attached to the beam, as shown in Figure 2.6. This provides a suspension which is still in all degrees of freedom except for rotations about the axis intersecting the two pivot points.

The stiffness of the flexure increases with thickness. Thus in order to decrease the resonant frequency of the beam balance, the flexure width is minimized. This is limited practically by the motion of the machining wire to yield flexures with widths of $10\text{-}15\ \mu\text{m}$. It was found that flexures thinner than $10\ \mu\text{m}$ could be achieved. However, the finished pieces contained irregular holes laterally through the flexure. These flexures would have lower breaking strength and would increase the loss if installed on in a BRS.

2.2.3 Vacuum System

To decrease the effects of air currents and gas damping, each BRS is placed into its own vacuum chamber which emulates the outline of the device, as shown in Figure 2.7. This chamber is initially evacuated to $\sim \mu\text{Torr}$ pressures using a roughing pump and turbo. After which the vacuum is maintained via a 10 l/s ion pump further decreasing the pressure to $\sim 0.1\ \mu\text{Torr}$.

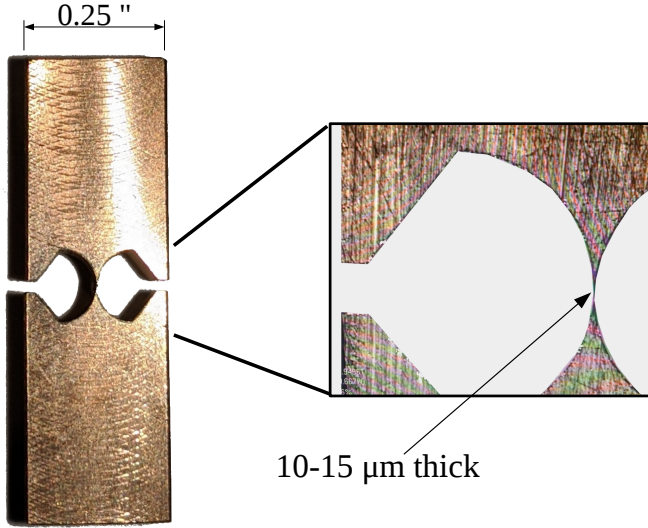


Figure 2.5: Image of a flexure used to suspend the beam balance with detail showing microscope image of the flexure point.

2.2.4 Multi-Slit Autocollimator Readout

The angular readout is achieved by a multi-slit autocollimator [28] which can be thought of as an improved optical lever.

Optical levers are simple optical angular readouts which exploit the law of reflection to measure angular deflections of a mirror by observing the displacement of a reflected beam. The angle of the mirror is described as:

$$\theta_s = \frac{x_{\text{reflected}}}{2d} \quad (2.11)$$

where θ_{mirror} is the angle of the mirror, $x_{\text{reflected}}$ is the displacement of the reflected beam, and d is the distance between the optical system and the mirror. This allows one to increase

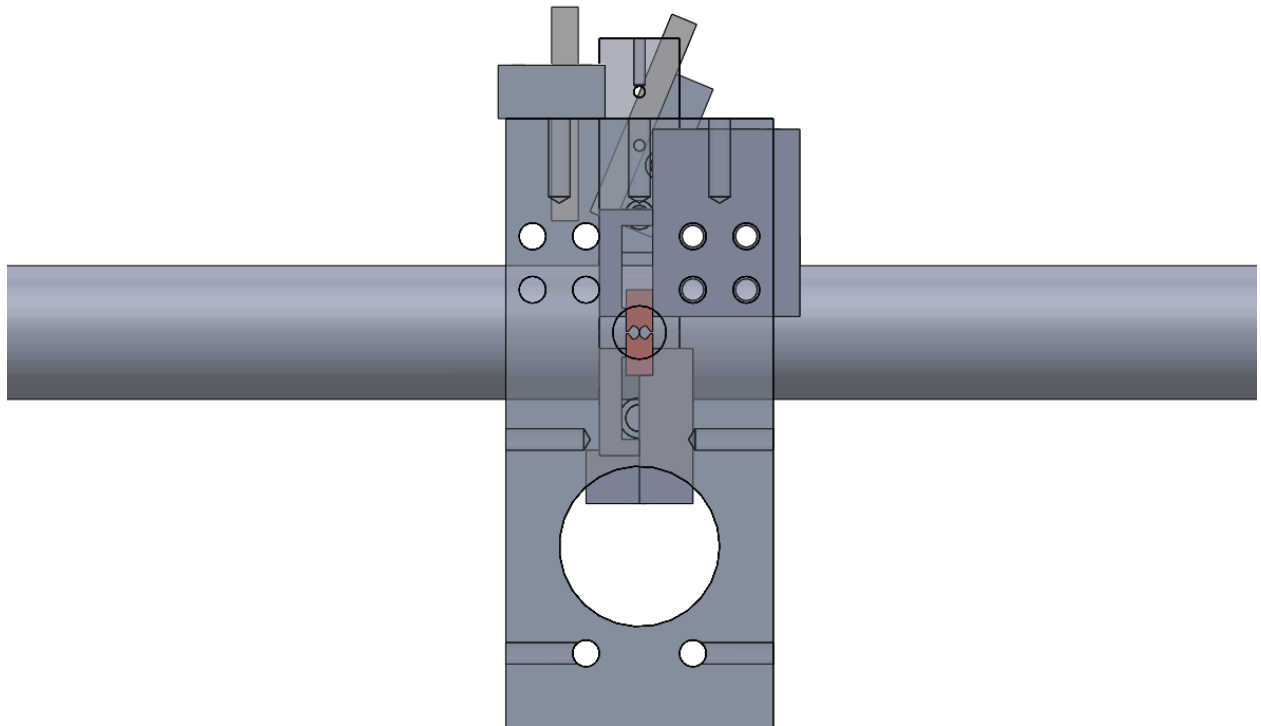


Figure 2.6: Close up view of the center of the CAD rendering of the BRS. One of the copper colored flexures can be seen at center along with its clamps. The two gray block at the top are mirrors for optical sensing, one fixed to the support the other attached to the beam.

the precious of the angular measurements arbitrarily by increasing d . However, with this comes the disadvantage that the effective gain of the sensor depends on d which may not be well known and may vary in time.

An autocollimator adds a lens located one focal length from light source and the screen. This effectively replace the distance dependence with the focal length of the lens which allows the system to be only sensitive, to first order, to the angular motion of the mirror.

To improve upon this further, a partially reflective mirror can be placed in between the

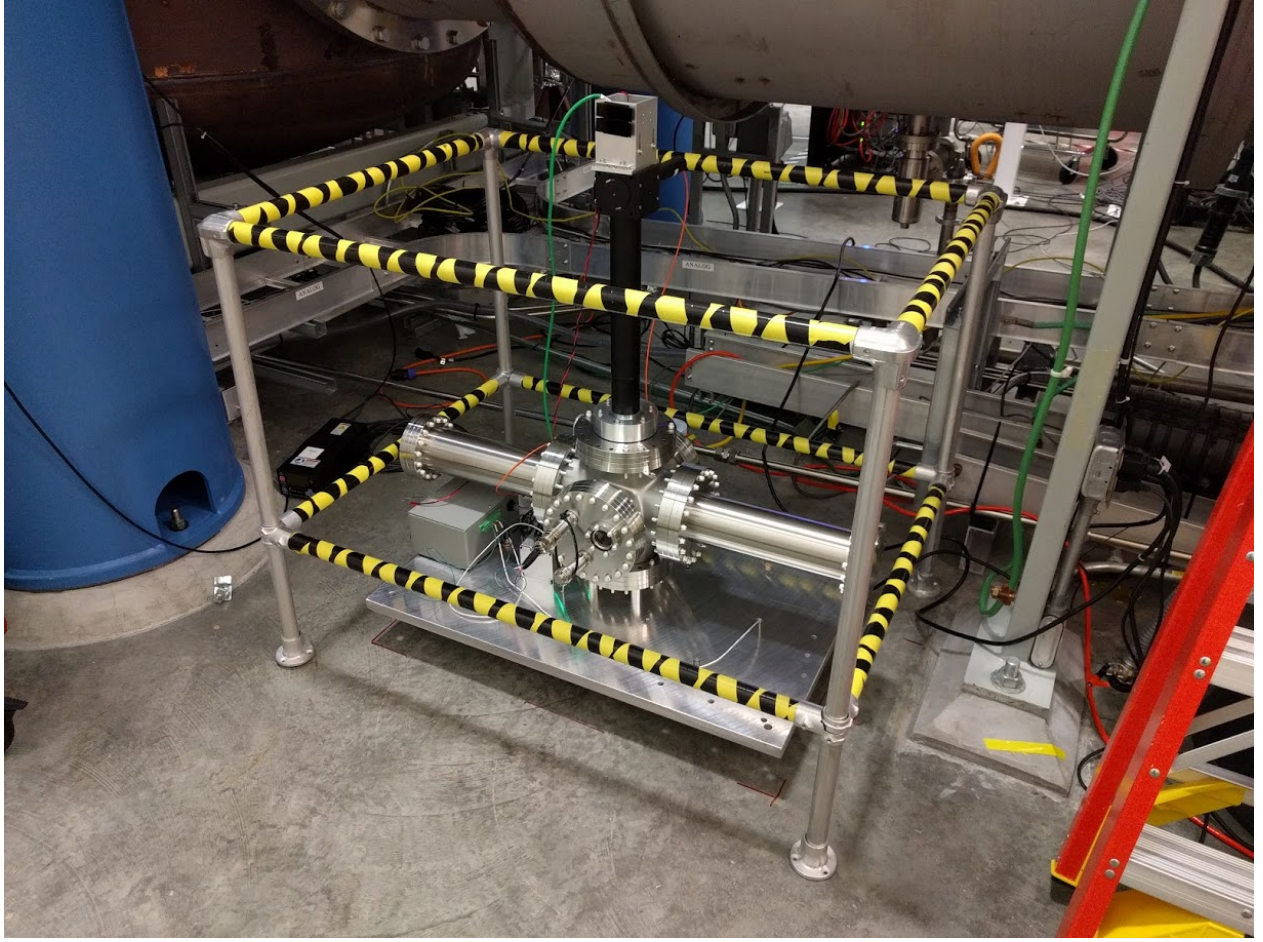


Figure 2.7: Picture of the BRS installed at LLO End-Y before the installation of the thermal insulation.

optical system and the main mirror to act as a reference and allows for the subtraction of any motion of the optical system with respect to the main mirror. This yield an angular readout described by:

$$\theta_s = \frac{x_{\text{main}} - x_{\text{reference}}}{2f} \quad (2.12)$$

where f is the focal length of the lens and $x_{\text{reference}}$ is the beam spot from the reference mirror.

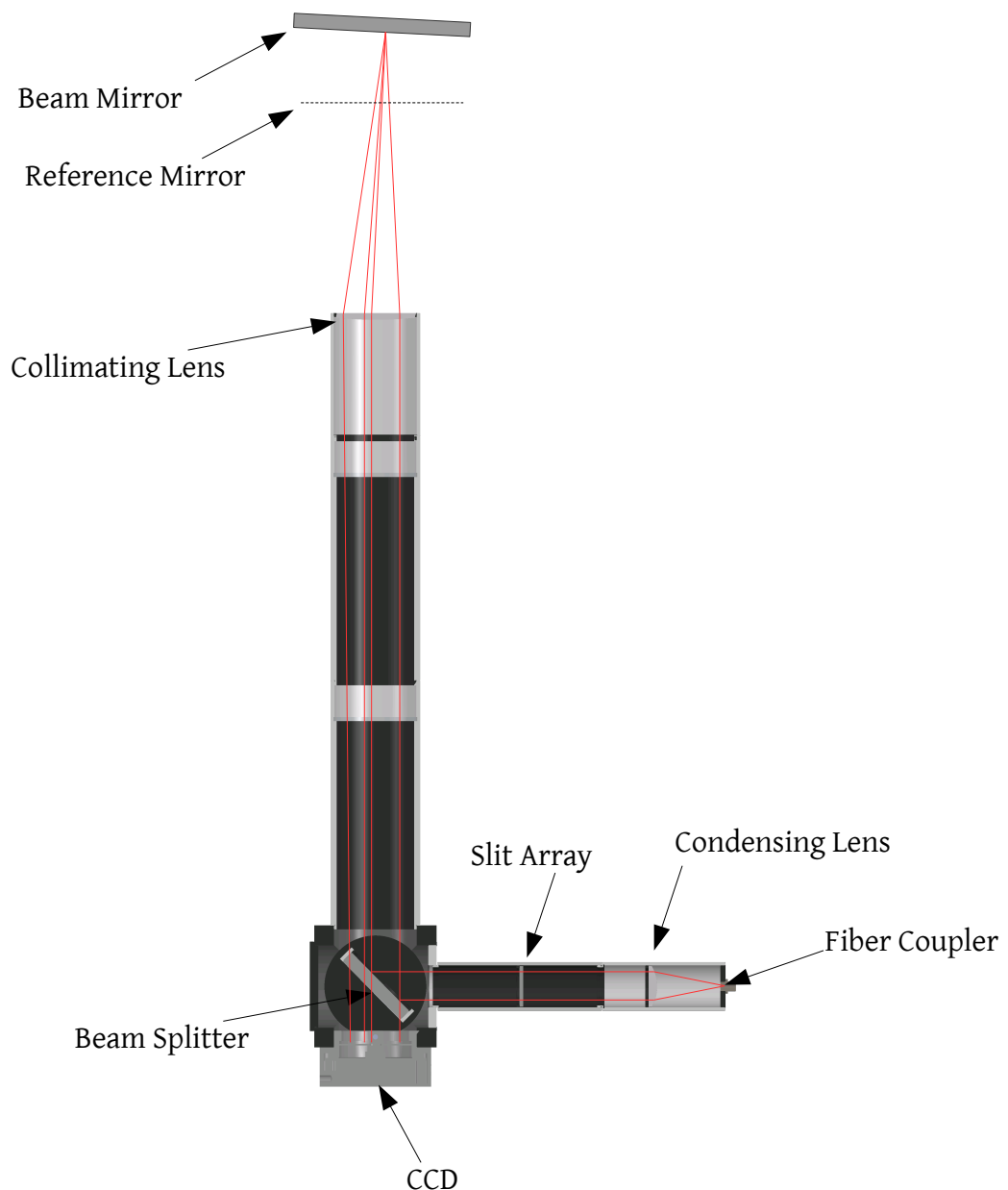


Figure 2.8: Schematic of a multi-slit autocollimator used for as the angular readout for the BRSs.

Parameter	Value
CCD	Balser Racer raL4096-24 gm
Pixel Number	4096
Pixel Size	$7 \mu\text{m} \times \mu\text{m}$
Pixel Depth	12 bits
Light Source	Fiber coupled LED
Wavelength	455 nm
Condensing lens focus	50 mm
Collimating lens focus	500 mm
Number of slits	38
Slit size	$\sim 0.127 \text{ mm}$

An increase in sensitivity can be made by employing a multi-slit autocollimator [28], shown in Figure 2.8. This consists of an autocollimator with the light source replaced by a illuminated photomask of a number of thin slits. The pattern is then reflected off a set of reference and main mirrors and imaged by a line CCD camera. These images are then analyzed to measure the distance between them thus yielding a measurement of angle. For the BRSs, this image analysis is achieved using bespoke software written in C# which can be found at www.github.com/mpross/BRSReadout

To extract the distance between the patterns, the image goes through a series of steps which take it from a vector of pixel intensities to a single angular output. When the software begins, the first frame that is captured is saved. All future frames are split into two, with one part representing the reference mirror and the other the main mirror. The cross correlation is then taken between each part and its matching section of the first frame. This gives a curve who's maximum is located at the pixel number corresponding to separation between the pattern in the current frame and the first frame, which can be seen in Figure 2.9. The points of this curve that are near the maximum are then fit to a Gaussian which allows for the extraction of the location of the peak with sub-pixel resolution. This is done for each

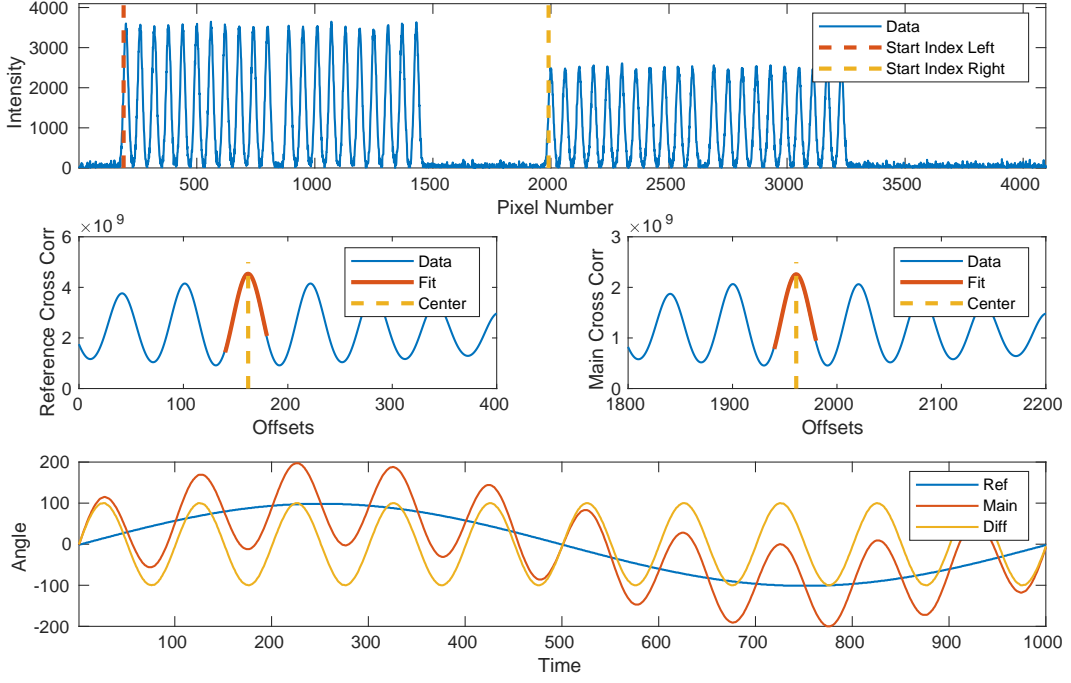


Figure 2.9: Simulation of the BRS image analysis algorithm. The top pane shows a simulated frame of the fringes as seen by the CCD, the middle panes show the cross correlation and fit from the two patterns, and the bottom shows the output of the algorithm for each pattern and the difference of the two. For this simulation the main pattern was modulated at 10 mHz while the reference was at 1 mHz.

pattern separately after which the difference between the reference pattern location and the main pattern location is taken. The difference is then proportional to the change in angle between the casing and the beam following Equation 2.12.

Compared to previous image analysis algorithms [28], this algorithm is computationally efficient while also being less susceptible to variations in the pattern image due to dust particulate, incorrect focusing, or beam clipping. A sensitivity of ~ 0.3 nrad/ $\sqrt{\text{Hz}}$ was achieved with this autocollimator design and image analysis algorithm.

2.2.5 Controls

As the BRSs are installed in active lab spaces, anthropogenic actively and environmental disturbances regularly apply torques on the beam-balance, either through mechanical or gravitational coupling. These can then cause the motion at the resonant frequency to rise to undesirable amplitudes. As the beam motion increases so does the noise and the effects of non-linearities of the readout. Additionally, some disturbances can be large enough to cause the amplitude to exceed the dynamic range of the autocollimator readout system.

To alleviate this issue, capacitor plates are installed underneath each end of the beam-balance to act as actuators. The force between the two capacitor plates follows:

$$F = \frac{\epsilon A V^2}{2d^2} \quad (2.13)$$

where ϵ is the permittivity of the material between the plates, A is the area of the plate, V is the voltage applied to the plates, and d is the distance between the plates. The plate under the beam is connected to a DAC while the beam is grounded which allows for a controlled actuation torque to be applied to the beam.

The control scheme that was adopted was one in which the feedback signal that is sent to the capacitors is the angular velocity of the beam band-passed between 2 mHz and 20 mHz to include only motion at frequencies near the resonance. The feedback is additionally applied with low gain so that the feedback only adds loss to the system as compared to locking the system in a strong feedback loop where all of the motion is absorbed into the control system. This is then implemented with two gain stages, a “low amplitude” stage, which is always on and yields a Q of 10-15, and a “high amplitude” stage, which is triggered if the amplitude rises above a threshold that is set based on the behavior of the given device and gives a Q of 5-10.

2.2.6 Noise Performance

In addition to the $0.3 \text{ nrad}/\sqrt{\text{Hz}}$ white noise of the autocollimator readout, these devices suffer from various mechanical noise sources, namely noise due to temperature variations and due to the thermal motion of the flexures.

Although the exact physical mechanism is unknown at this juncture, it has been observed that variations in the exterior temperature cause shifts in the balance's equilibrium position. Furthermore, temperature gradients across the instrument emanating from unbalanced heat sources and air currents have been seen to cause time varying noise. To alleviate this issue the instrument's vacuum chamber and optics are wrapped in multiple alternating layers of packing foam and aluminum foil. The entire apparatus is then placed inside a large double walled insulation box to further decrease any temperature variations. This decreases these effects yet it is believed to still limit the performance below 20 mHz.

More fundamental is the noise due to the thermal vibrations of the flexure. At non-zero temperature, a portion of the thermal energy of the flexures excites mechanical motion. This causes a fundamental stochastic noise floor that follows [29]:

$$\tilde{\theta}_T(\omega) = \sqrt{\frac{4k_B T \omega_0^2}{I\omega Q((\omega^2 - \omega_0^2)^2 + \omega_0^4/Q^2)}} \quad (2.14)$$

To limit the influence on the performance of the device, the resonant frequency of the spring-mass system is pushed to the lowest frequency that is mechanically feasible. This is the fundamental noise of the instrument and thus is independent of readout and environmental effects.

One further noise source comes from voltage noise on the capacitive actuators. The force follows Equation 2.13 and can be shown to be sub dominate. Assuming a voltage noise on the capacitors of $0.1 \text{ V}/\sqrt{\text{Hz}}$, which is larger than expected with the installed electronics, the corresponding torque noise is $4.3 \times 10^{-13} \text{ N}/\sqrt{\text{Hz}}$. This then leads to an angle noise that is ~ 100 times less than the measured noise.

The noise budget for a BRS is shown in Figure 2.10 which shows that the device is

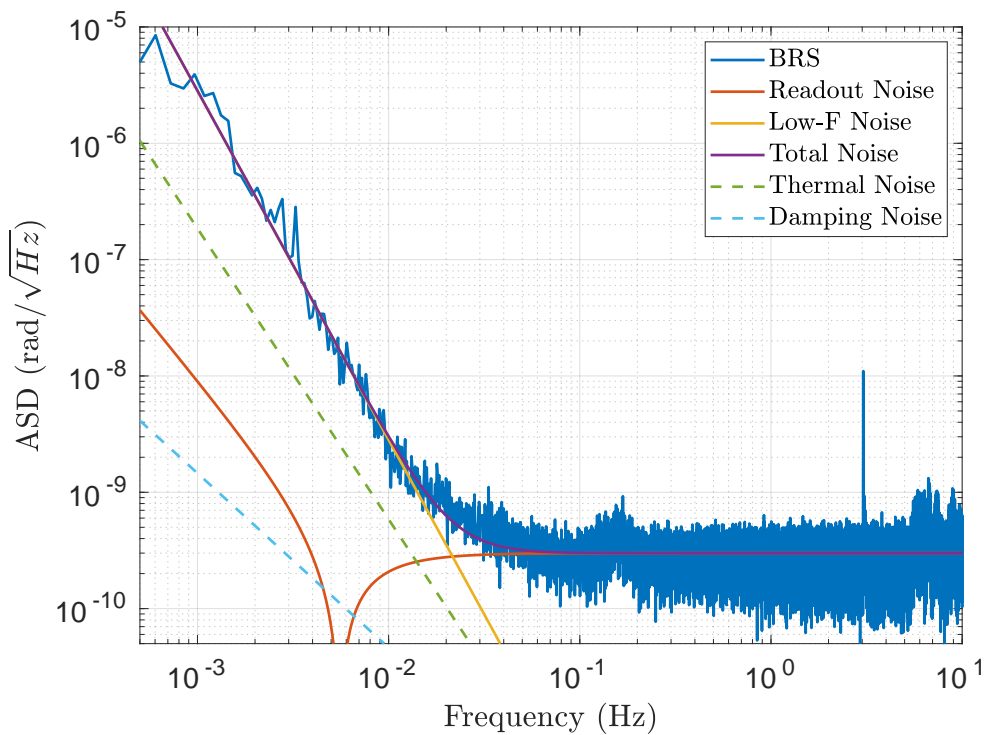


Figure 2.10: Noise budge for the Beam Rotation Sensors where the blue curve shows the performance at a quiet time, in red is a model of the readout noise, yellow shows an estimate of the low-frequency noise, purple shows the sum of these, and cyan and green show upper limits of the thermal and damping noise.

readout dominated above ~ 20 mHz and below is dominated by unknown noise thought to be sourced by temperature variations. Respectively at 150 mHz, 3 Hz, and 6 Hz the rotational microseism, torsion mode of the beam-balance, and motion due to nearby instrumentation can be seen above the predicted noise sources.

2.3 Results

2.3.1 Hanford Installation

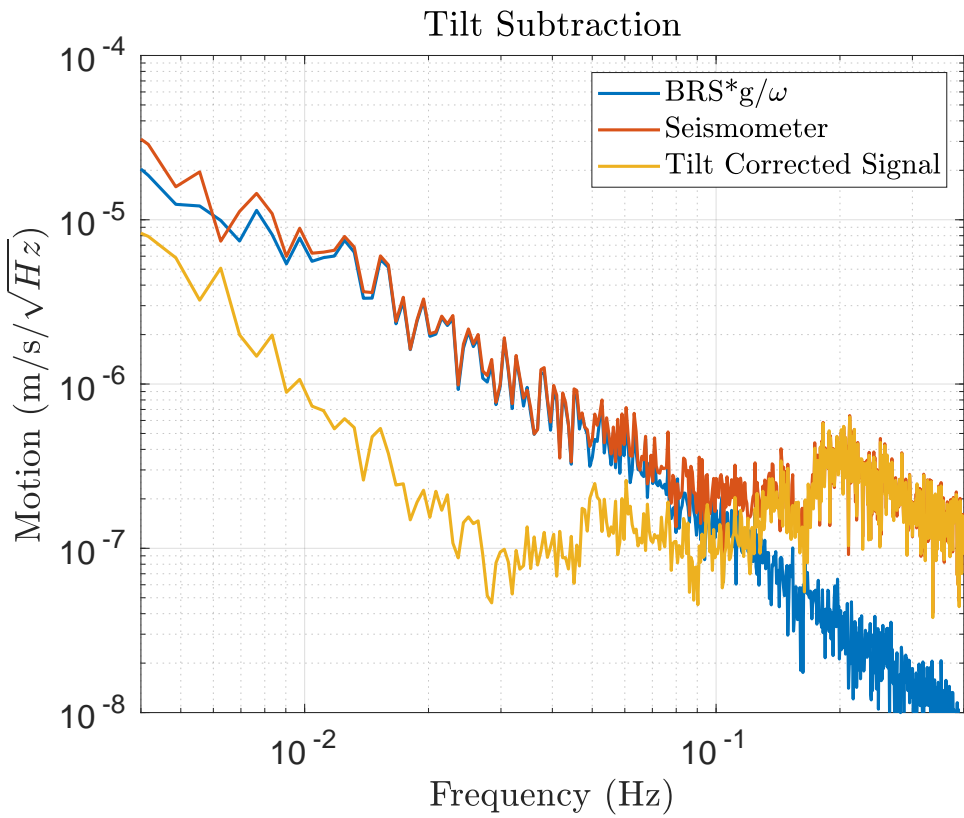


Figure 2.11: Representative amplitude spectral density showing the tilt subtraction during ~ 11 m/s winds achieved at End-X of LHO where blue is the BRS signal multiplied by g/ω , red is the raw seismometer signal, and yellow is the tilt corrected signal. Similar performance has been achieved by all of the deployed BRSs.

Between LIGO's first (O1) and second (O2) observing runs, two BRSs were installed at the LIGO Hanford Observatory (LHO), one at each end station correcting the translations along their respective arm.² Although one would expect that the corner station seismometers would also need to be corrected, a location was found within the corner station building which exhibited low tilt.³ As such no BRS was necessary to achieve low tilt contamination.

The tilt subtraction performance achieved with these devices can be seen in Figure 2.11 where it is evident that the system achieves tilt subtraction from around 6 mHz to 50 mHz. Above 50 mHz the seismometer signal is dominated by the oceanic microseism and the tilt contribution is negligible. Below 6 mHz, the BRS signal becomes overwhelmed by instrumental noise. This performance can also be seen in Figure 2.12 which shows a example time series of the tilt subtraction where suppression of a handful of transients, likely due to wind gusts, can be seen.

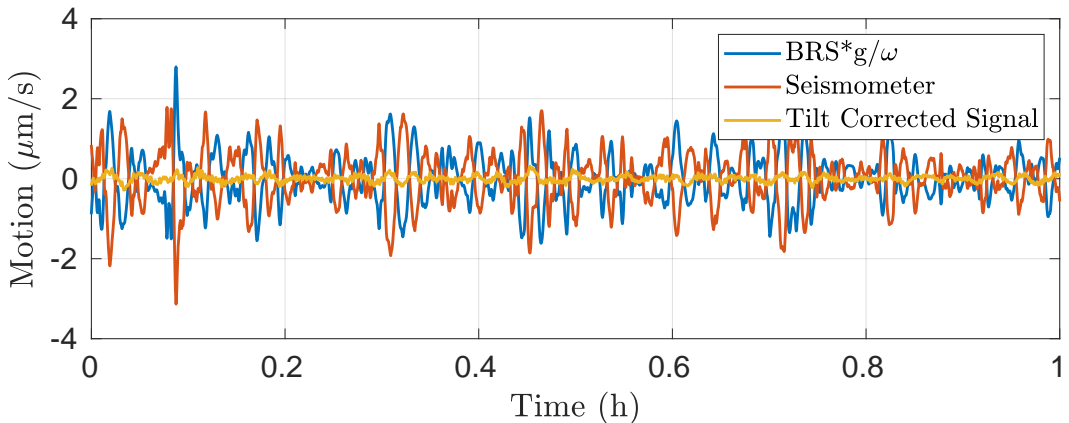


Figure 2.12: Time series showing the tilt subtraction at End-X of LHO where blue is the BRS signal multiplied by g/ω , red is the raw seismometer signal, and yellow is the tilt corrected signal. All channels are band-passed from 10-100 mHz. As can be seen, the tilt subtraction removes a collection of transients, likely due to the gusts of wind.

²Motion orthogonal to the interferometer arms couples only indirectly through pathways such as defects of the test masses and mechanical cross couplings. Thus this coupling is significantly suppressed compared to motion along the arms.

³This low tilt location is due to its distance from the walls of the building.

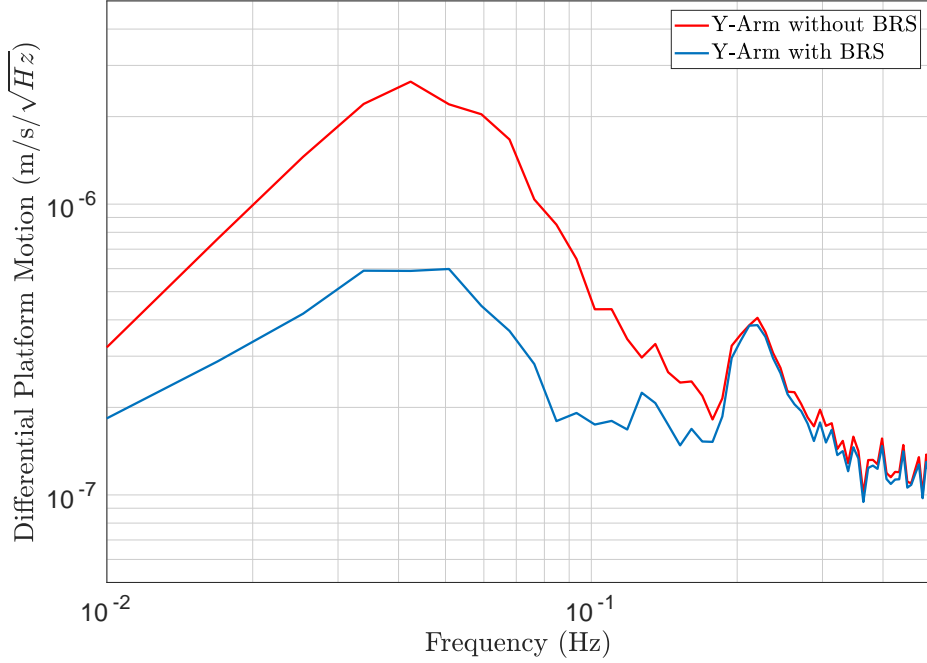


Figure 2.13: Differential platform motion for the Y-Arm of LHO with and without the BRSs installed.

This tilt subtracted channel was then used as the ground signal for the isolation's sensor correction, described in Section 1.3.3 instead of the raw seismometer. The primary effect of the interferometer of the use of this channel is a decrease in the differential motion between pairs of platforms which form the arms of the interferometer. This is shown in Figure 2.13 where it is evident that the differential motion was decreased by a factor of $\sim 3\text{-}4$ between 20–100 mHz. This decrease in differential motion increases the ability to lock the interferometer by decreasing the demand on the downstream control systems.

2.3.2 Livingston Installation

After the success of the Hanford BRS installation, four devices were installed at the LIGO Livingston Observatory (LLO) between the second and third (O3) observing runs. Due to

differences in the size and shape of the corner station building at LLO, a low tilt location was not found. Thus two BRSs were installed located near the two input test masses along with one at each end station correcting the seismometer signal oriented along their respective arms.

All four devices achieved comparable tilt-subtraction as the Hanford installation and were implemented in a similar fashion.

2.3.3 Ground Tilt Model

As mentioned in Section 2.1.1, the primary driver of ground tilts at the observatories is wind acting on the building’s walls which deforms the concrete floor in a non-trivial manner. Thus modeling the ground tilt spectrum for a given wind speed from first principals is intractable. However, with the collection of observations made by the BRSs installed at the sites, an empirical model can be readily constructed.

To achieve this, hour long spectra of the BRS output at the End-X of LHO during O3a were sorted into a collection of bins depending on the average wind speed measured during that hour. Each bin was then averaged to yield a representative spectrum for each wind speed. This was then fit to an empirically determined model, Equation 2.15, containing two terms: the first constituting the broad behavior of the spectrum and a second which enhances the high frequency motion at high wind speeds. The parameters of this were then fit vs wind speed to yield a tilt spectrum vs wind speed model.

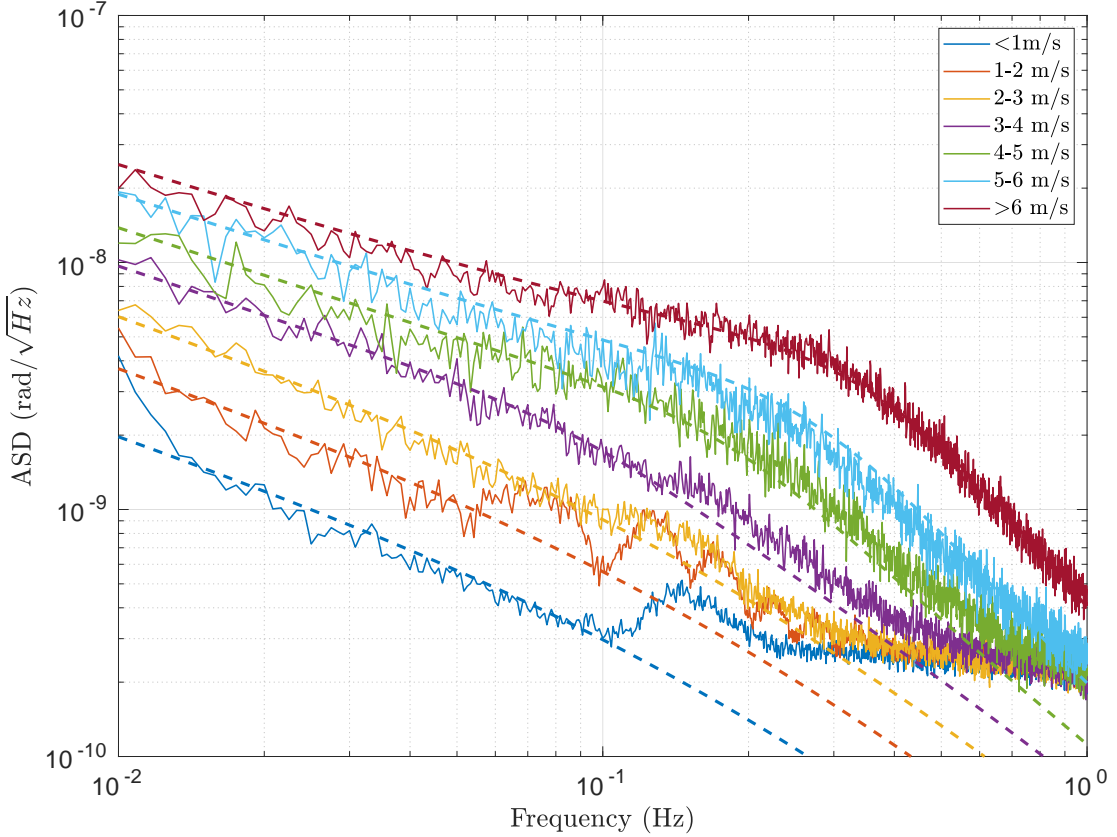


Figure 2.14: Observed and modeled tilt vs wind speed for LHO End-X. The solid lines are the measured ground tilt while the dashed are the model. At low wind speeds, the BRS noise and the microseism become dominate at high frequencies.

$$\tilde{\theta} = \frac{x_1}{(f/1 \text{ Hz})^{2/3}(1 + f/f_1)} + \frac{x_2}{1 + (f/f_2)^3} \quad (2.15)$$

$$f_1 = 0.2 \text{ Hz}$$

$$f_2 = (0.1 (s/1 \text{ m/s}) - 0.25) \text{ Hz} \text{ if } s > 2.5 \text{ m/s} \text{ else } f_2 = 0$$

$$x_1 = (1.4 \times 10^{-11} (s/1 \text{ m/s})^2 + 5.7 \times 10^{-11} (s/1 \text{ m/s}) + 6.4 \times 10^{-11}) \text{ rad}/\sqrt{\text{Hz}}$$

$$x_2 = (1.8 \times 10^{-10} (s/1 \text{ m/s})^2 - 7.6 \times 10^{-10} (s/1 \text{ m/s}) + 1.2 \times 10^{-9}) \text{ rad}/\sqrt{\text{Hz}}$$

Here s is the wind speed, f is the frequency, and $\tilde{\theta}$ is the tilt spectral density. Comparison of this model to data is shown in Figure 2.14 which shows good agreement at most wind speeds. Below 1 m/s, the tilt due to the microseismic motion and the sensor noise become dominate above 100 mHz. Between 1-2 m/s, the data was corrupted by local anthropologic activity above \sim 50 mHz. This model can be utilized to calculate the theoretical performance of the seismic isolation, as is done in Section 3.3.1.

2.3.4 Duty Cycle Improvements

The figure of merit which most readily displays the improvements in duty cycle due to inclusion of the BRSs is the empirical probability of the interferometer being locked at a given wind speed over the three observing runs. This is shown in Figures 2.15 and 2.16 for LHO and LLO, respectively. It should be noted that BRSs were implemented at Hanford for both O2 and O3a while Livingston was only for O3a.

For Hanford, the benefit of the tilt subtraction scheme can clearly be seen between O1 and O2 curves. During O1 the locked probability fell monotonically with wind speed, while for O2 the probability stayed relatively constant up to 15 m/s above which it fell steadily. For O3a, Hanford saw a clear decrease in performance at high wind speeds yet still out performed the O1 scheme. This loss of performance is likely due to the Y-arm beam being displaced away from the center of the test masses to avoid point absorbers on the Input-Y test mass. This is known to increase coupling between the angular motion of the test mass and the length measured by the interferometer. This then increases the drive needed to keep the interferometer locked and thus increases the susceptibility of the system to increased seismic motion.

If one allows for a fudge factor to be applied to the O2 duty cycle in order to match the low wind speed performance of O1 and O3a, then this duty cycle equates to an observing time increase of 13.1 days per year between O1 and O2 and a decrease of 2.9 days/year between O2 and O3a.

Also shown in Figure 2.15 is the fraction of the GW events or candidates detected during

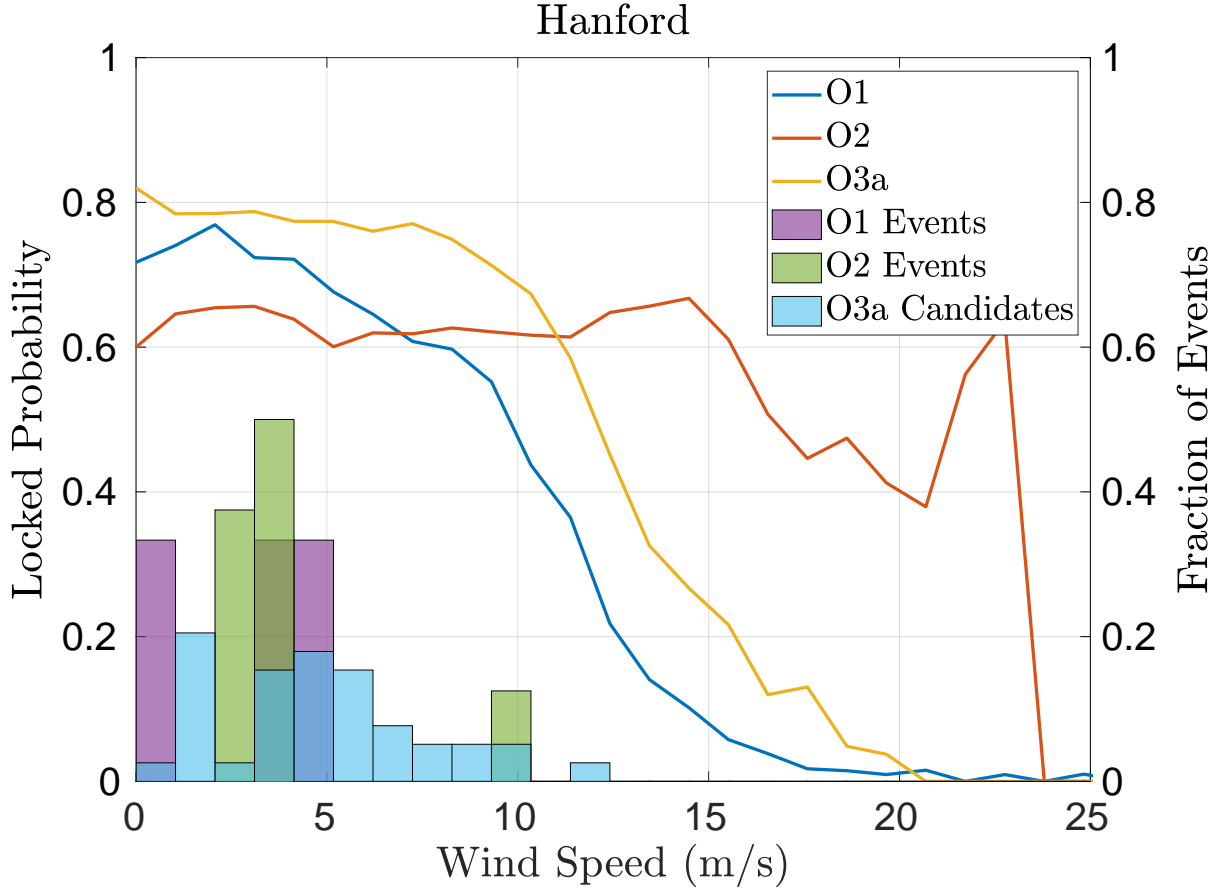


Figure 2.15: Duty cycle improvements for the LIGO Hanford Observatory along with distribution of observed events vs. wind speed.

O1, O2, and O3a at a given wind speed. This shows that a collection of GW events have been observed whose detection probability is directly increased due to the increase duty cycle at higher wind speeds. Namely, GW170104 was measured at ~ 11 m/s which had an increase in duty cycle of $\sim 20\%$ between O1 and O2. Additionally, a number of O3a candidates have been detected above ~ 5 m/s at which the probability of being locked is increased by $\sim 20\%$.

At Livingston, the improvements at increased wind speeds is less dramatic as can be seen in Figure 2.16. Although between O1 and O2 tilt subtraction was not implemented, a increase in duty cycle was achieved by implementing a single seismometer for sensor correction on

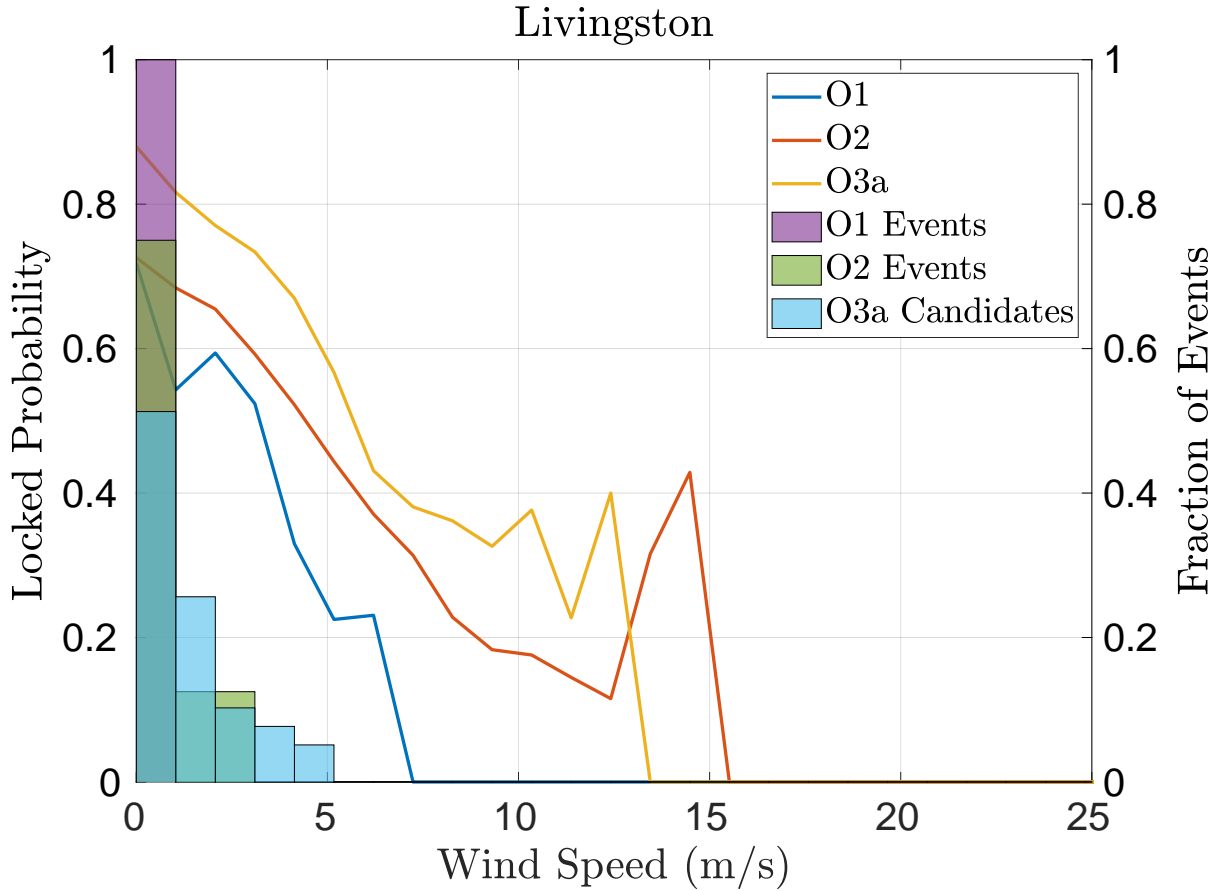


Figure 2.16: Duty cycle improvements for the LIGO Livingston Observatory along with distribution of observed events vs. wind speed.

all of the corner station platforms. This decreased the differential mode motion at higher wind speeds and thus made the interferometer lock more robust. An additional increase in performance can be seen between O2 and O3a due to the deployment of tilt subtraction. However, the probability of being locked still dropped monotonically with wind speed, similar to the O1 performance of Hanford.

Despite this, there is a collection of O3a candidates detected between 3-6 m/s which are more probable with the increased robustness against wind speed. Additionally, this performance equates to an observing time increase of 13.9 days per year between O1 and O2

and 6.9 days/year between O2 and O3a.

An additional metric that quantifies the improved robustness of the interferometer is the expectation value of wind speed during gravitational wave events which is shown in Figure 2.17. In the limit that the detection likelihood is independent of wind speed, one would expect that the expectation value of the wind speed during events would match that of the entire run. As can be seen in Figure 2.17, with the installation of the BRSs each site approaches this limit.

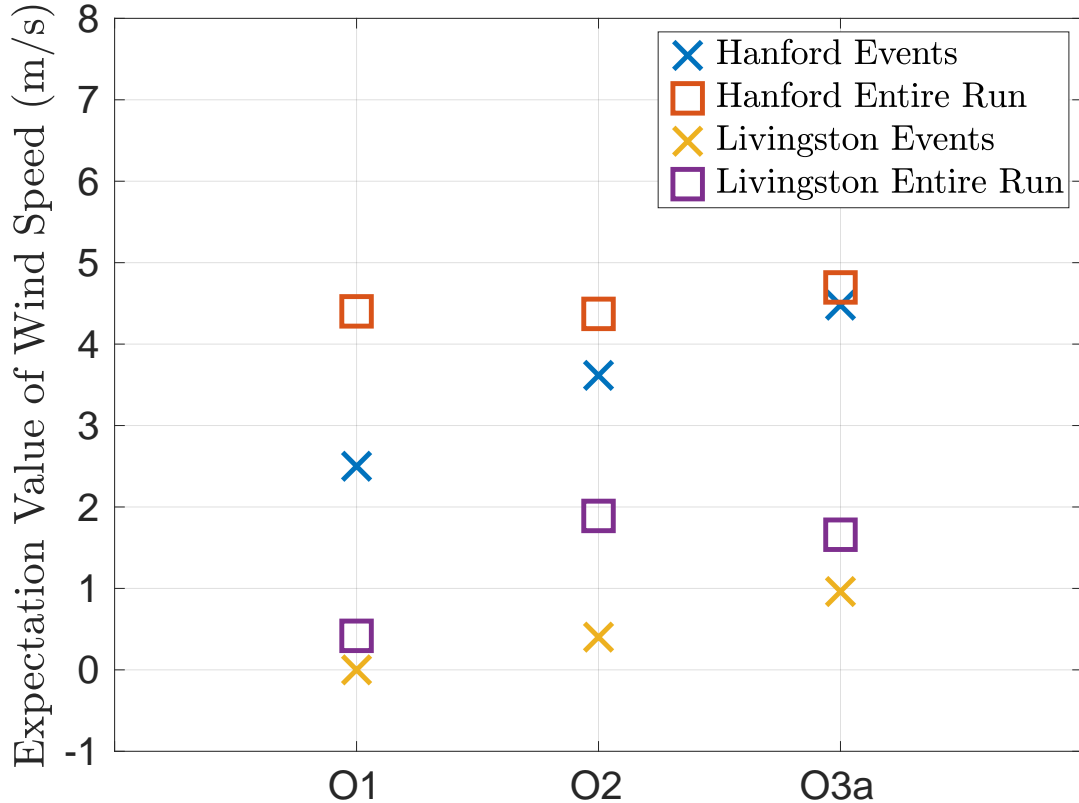


Figure 2.17: Expectation value of wind speed during gravitational wave events and for the entire observing runs.

Chapter 3

30-CM SCALE ON-BOARD ROTATION SENSORS

3.1 Angular Controls

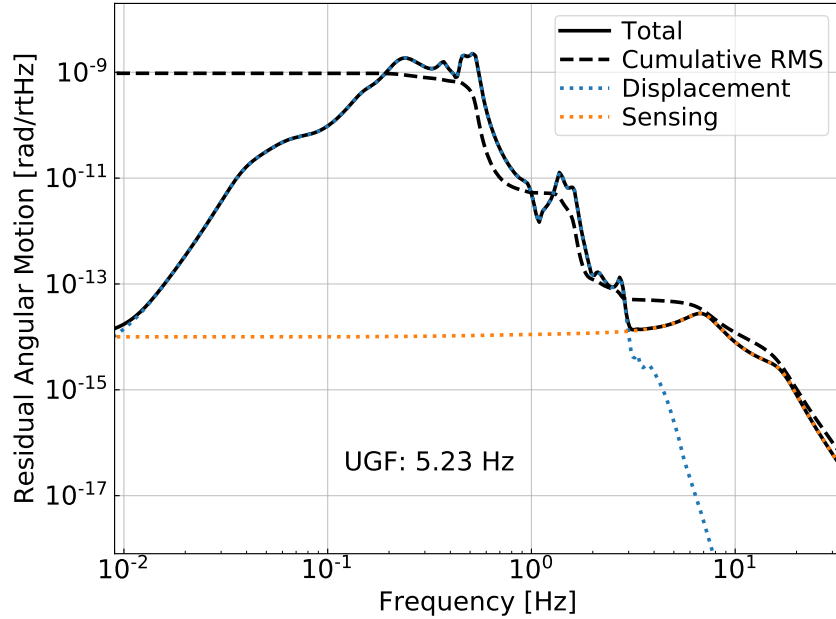


Figure 3.1: A model of the performance of the current angular sensing and control system. This model optimizes the unity gain frequency of the ASC loop to maximize performance above ~ 10 Hz while maintaining the low frequency rms at $1 \text{ nrad}/\sqrt{\text{Hz}}$.

To operate the LIGO interferometers in their optimal configuration, the relative angular motion of the test masses must be under 1 nrad rms [30]. Although the seismic isolation system significantly attenuates the input motion to the optics, additional controls are needed

to meet this requirement. The angular sensing and control system (ASC) consists of a number of optical sensors which are fed back to actuators on the quadruple pendulum.

With the current seismic isolation system, at ~ 0.2 Hz the rotational performance is limited by the sensor noise in the seismometer pair which forms the isolation platform's angular sensors [26]. This then increases the residual translational motion due to tilt contamination, described in Section 2.1.1. To eliminate this residual, high-gain feedback loops are required on the downstream ASC system, which themselves are limited by their respective sensor noise above ~ 3 Hz. This left over noise then leaks into the gravitational wave band between 10 - 55 Hz due to the inability to sharply roll off the sensor noise without interfering with the control at lower frequencies. A model of the current ASC system is shown in Figure 3.1.

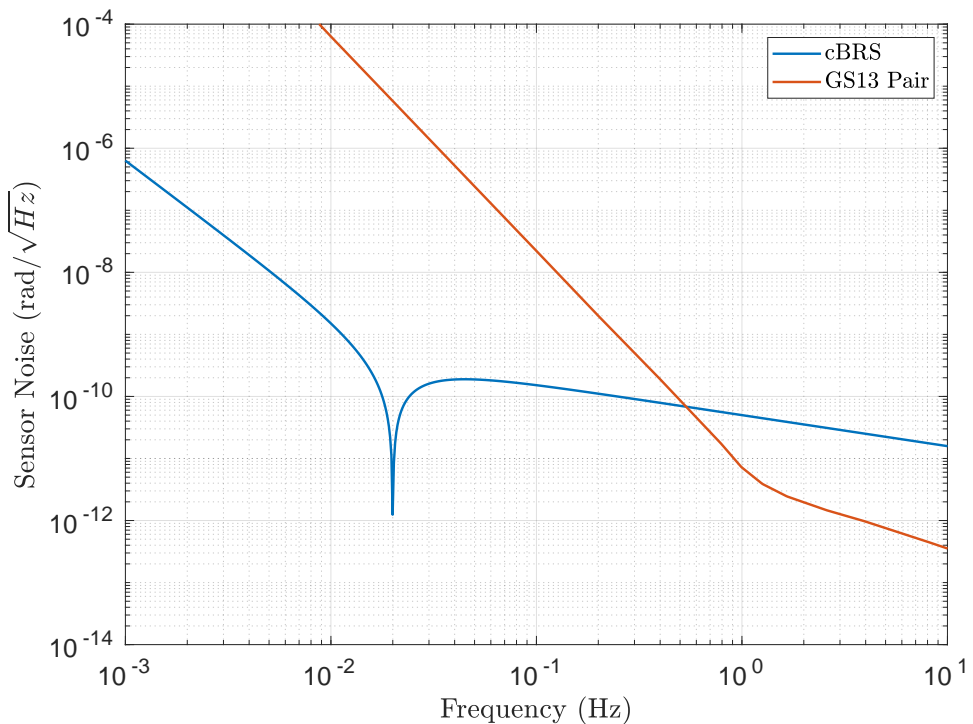


Figure 3.2: Theoretical noise curves for the cBRS, blue, and seismometer pair located 1-m apart.

The compact Beam Rotation Sensor (cBRS), described in the following, was designed to be an alternative angular sensor for the seismic isolation system with \sim 100-1000 times lower noise than the current sensors. Design sensitivity of the cBRS and the current seismometer pair are shown in Figure 3.12. With this decreased noise, the seismic isolation control loops can be tuned to significantly increase the performance of both the translational isolation, through decreased tilt contamination described in Section 2.1.1, and, directly, the rotational isolation. Details of this follow in Section 3.3.1. This decreased residual rotation would then allow the angular control loops to be retuned, specifically decreasing the unity gain frequency (UGF), to decrease the sensor noise leakage in the gravitational wave band.

Additional benefits are also expected to accompany the improved seismic isolation. This include decreased effects of scattered light and increased robustness against environmental effects. Beforehand modeling these effects are intractable but will be studied in detail for future installations.

3.2 Compact Beam Rotation Sensor

3.2.1 Mechanical System

Similar to the BRS described in Chapter 2, the compact Beam Rotation Sensor (cBRS), shown in Figure 3.3-3.4, consists of a 30-cm long cross hung from 10-15 μm thick beryllium-copper flexures and has an identical operating principle as the BRS. Above the resonant frequency the beam acts as an inertial reference whose angle is measured with respect to the support. Thus Equations 2.7-2.10 govern its mechanics. The cross shape of the balance decreases the sensitivity of the device to gradients in the local gravitational field while allowing for increased moment of inertia compared to a similarly sized beam.

This design yields a resonant frequency of \sim 20 mHz which limits the use of such a device with high fidelity to frequencies about and above this. This removes the possibility of using such a device for ground tilt subtraction since the relevant ground tilts happen below 40 mHz.

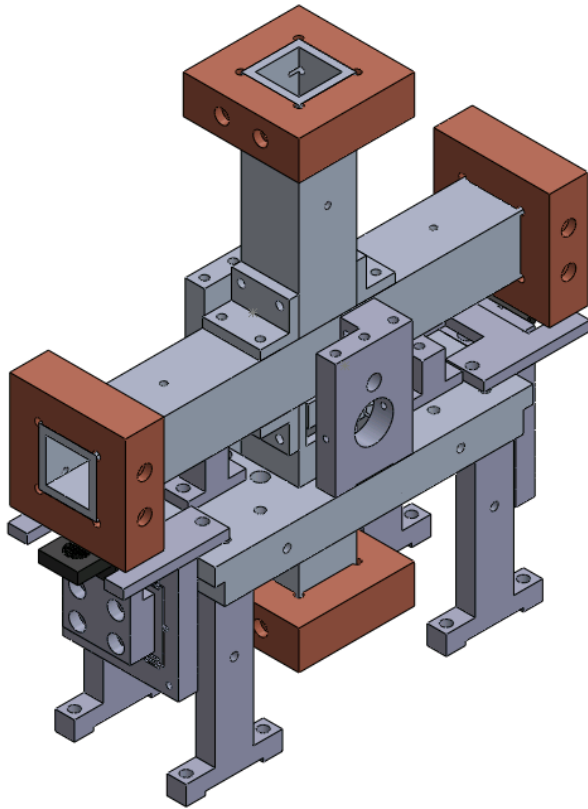


Figure 3.3: CAD rendering of the compact BRS (cBRS) showing the cross with its copper end masses which is hung from the flexures from the surrounding support structure. Additionally, the translation stages which hold the fiber interferometer readouts can be seen on either end of the support below the two horizontal end masses.

3.2.2 Kinematic Mount

To allow for ease of installation, the proof mass is suspended via a kinematic mount, shown in Figure 3.5. The mount consists of three titanium spheres which are attached to the proof mass's horizontal beam and three pairs of titanium cylinders attached to a seat. This seat is then suspended by flexures, described in Section 2.2.2. The spheres and cylinders are epoxied in place to form an equilateral triangle.

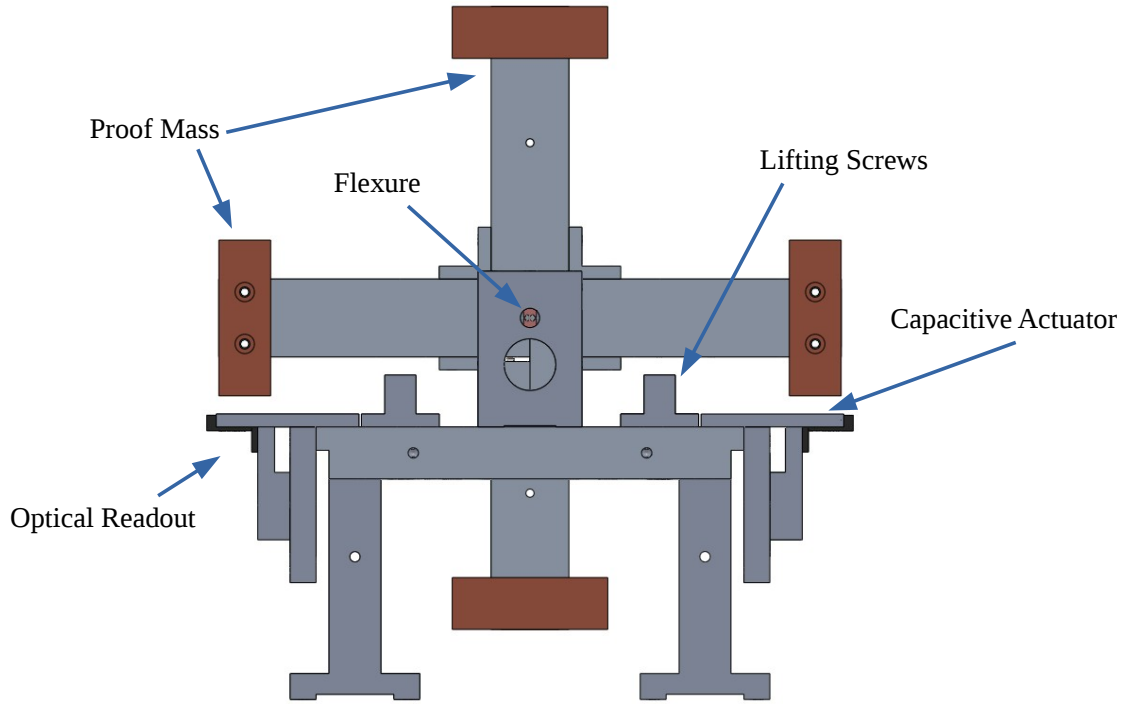


Figure 3.4: CAD rendering of the compact BRS (cBRS) showing the cross with its copper end masses which is hung from the flexures from the surrounding support structure. Additionally, the translation stages which hold the fiber interferometer readouts can be seen on either end of the support below the two horizontal end masses.

This design allows for the delicate procedure of clamping the flexures to be done with only the seat. After which the proof mass is lowered on to the seat where the matching sets of spheres and cylinders repeatably constrains its position relative to the flexures.

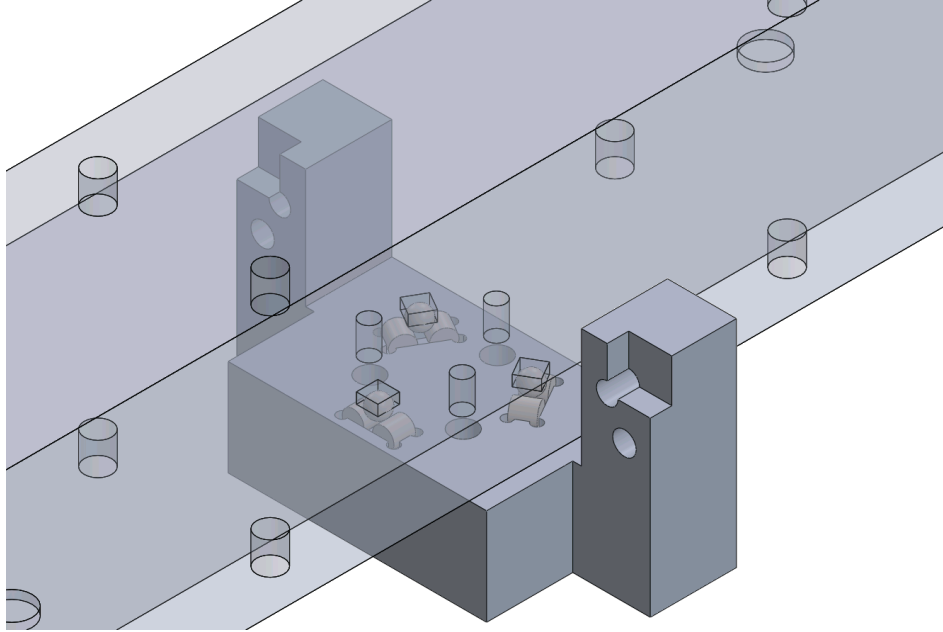


Figure 3.5: CAD rendering of the compact BRS (cBRS) showing the cross with its copper end masses which is hung from the flexures from the surrounding support structure. Additionally, the translation stages which hold the fiber interferometer readouts can be seen on either end of the support below the two horizontal end masses.

3.2.3 Interferometric Readout

In order to maintain the small size of the entire device and to decrease readout noise, an interferometric readout was developed that consists of a Fabry-Perot cavity formed by a beamsplitter-coated optical-fiber and a full-reflecting mirror placed on the bottom of the balance's end masses, shown in Figure 3.6. The reflectance of this cavity is then monitored by employing a circulator to separate the incoming and outgoing rays. The readout optics are schematically shown in Figure 3.7. As the cavity length changes the reflectance undergoes an interference pattern described by:

$$R = \frac{F \sin^2(2\pi nx/\lambda)}{1 + F \sin^2(2\pi nx/\lambda)} \quad (3.1)$$

where R is the reflectance, F is the finesse, x is the length of the cavity, n is the index of refraction of the cavity, and λ is the wavelength.

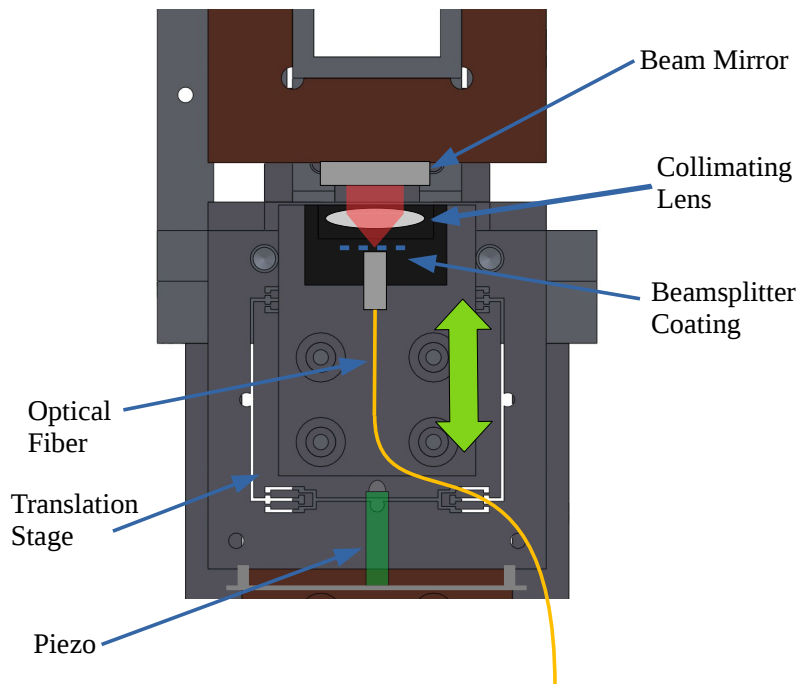


Figure 3.6: Diagram of the cBRS fiber interferometer read-head.

To linearize this readout, the optical fiber tip and collimating lens are placed on a translation stage that is driven by a piezo stack. The intensity of the reflected light is then fed back to the piezos using a PID loop to hold the cavity length fixed. This allows the system to be separated into two linear readouts, the interferometer output for small ranges above the UGF of the loop and the control loop output for large motions below the UGF. The output of the device is then the sum of these two channels.

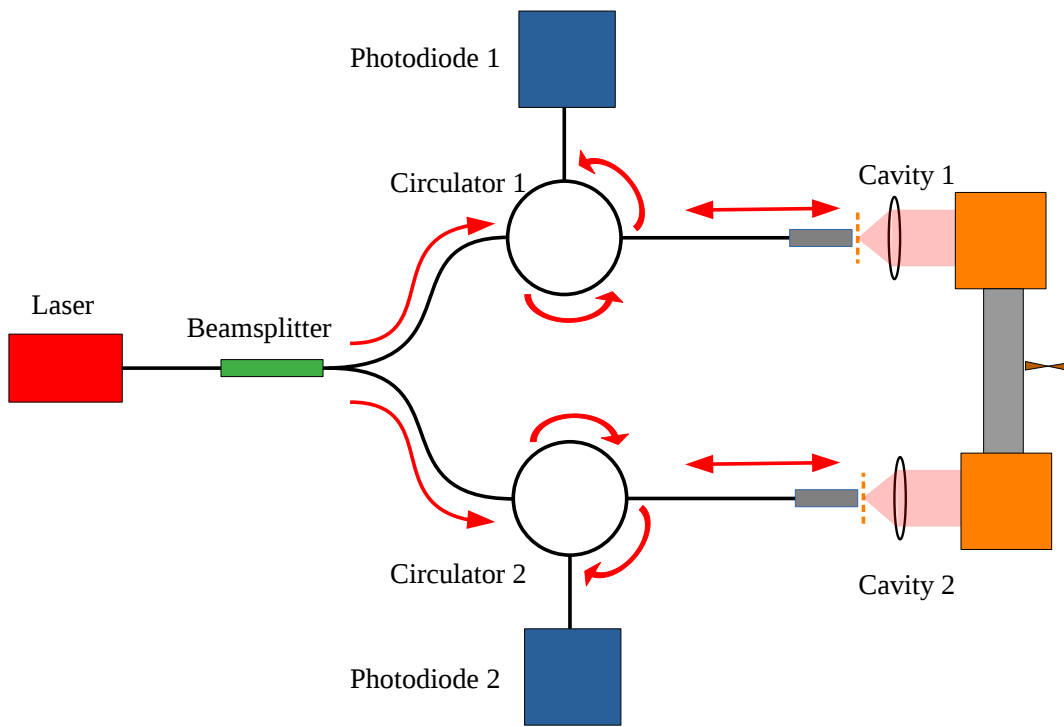


Figure 3.7: Layout of the cBRS readout optics.

Parameter	Value
Laser	QPhotonics QDFBLD-1300-10
Wavelength	1310 nm
Fiber beamsplitter	Thorlabs TWQ1300HA
Circulator	Thorlabs CIR1310-APC
Fiber-tip beamsplitter	Thorlabs SMF28ER 50/50 FC/PC
Collimating focus	2.75 mm
Photodiode	Thorlabs PDA10CS InGaAs
Piezo	Tokin AE0505D16F
Piezo Max Range	17.4 μ m at 150 V
Piezo Driver	PDU150 150 V

Although in theory the angle of the beam can be measured with a single interferometer, two readouts are deployed, one at the end of each arm, in order to allow for suppression of common mode noise. The signal seen in each readout is described by:

$$\theta_1 = \theta_s + x_1/L + x_1\delta_\lambda/\lambda^2 + n_c + n_1 \quad (3.2)$$

$$\theta_2 = -\theta_s + x_2/L + x_2\delta_\lambda/\lambda^2 + n_c + n_2 \quad (3.3)$$

Where $\theta_{1,2}$ are the angle equivalent signal seen in readout 1 and 2, θ_s is the sensed angle, $x_{1,2}$ are the length of the respective cavities, L is the arm length of the beam, δ_λ is the change in wavelength of the laser, λ is the wavelength of the laser, n_c is the sum of all unmodeled common noises, and $n_{1,2}$ are the unmodeled noises that appear in one readout and not the other.

As the angle of the beam appears with opposite phase in the two readout, the difference between the two, Equation 3.4, contains the angle while suppressing common noise. Most notable of these common noise sources is frequency noise of the laser. This couples to the angle only through the mismatch in the average cavity lengths which are matched to within 1 mm. On the other hand, the sum of the two channels, Equation 3.5, contains no contribution from the angle but is instead comprised of only noise sources and thus allows for an in-situ estimate of the sum of noises.

$$\Delta\theta = 2\theta_s + (x_1 - x_2)\delta_\lambda/\lambda^2 + n_1 - n_2 \quad (3.4)$$

$$\Sigma\theta = (x_1 + x_2)/L + (x_1 + x_2)\delta_\lambda/\lambda^2 + 2n_c + n_1 + n_2 \quad (3.5)$$

3.2.4 Calibration

The two readouts are calibrated independently to take into account differing piezo calibration and amplifier gains. The calibration is done by driving the piezo linearly through its entire

range while the beam is locked. During this drive the interference pattern wraps through multiple fringes as the cavity length is decreased. The minima of these fringes is known to be separated by $\lambda/2$ which allows for the calibration from the voltage across the piezo to displacement. The region around the 50% reflectance point, which is the operating point of the interferometer, is then fit to a linear function of displacement to yield a calibration from reflectance to displacement.

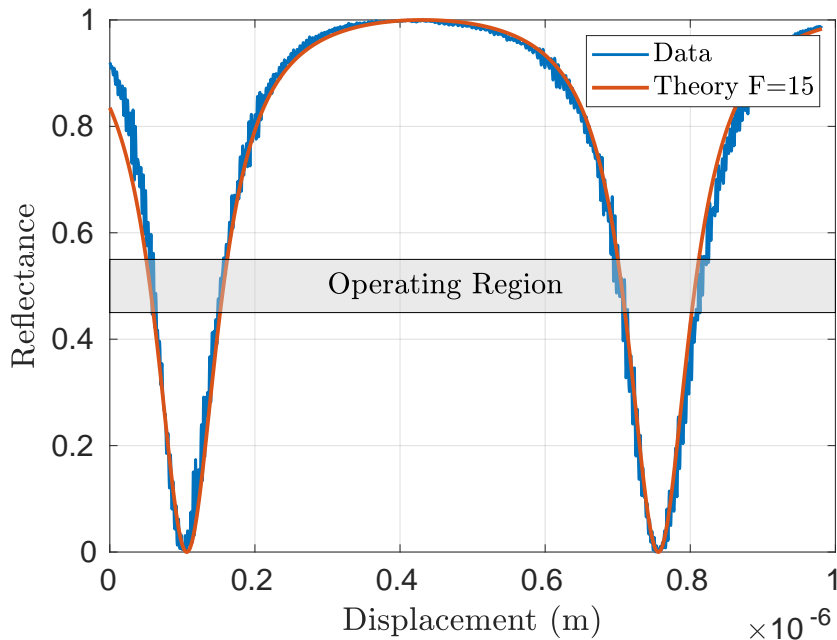


Figure 3.8: Interference pattern of a cBRS fiber interferometer vs cavity length. The gray region is where the device is operated in normal conditions. Within this region the reflectance is approximately linear verse displacement.

This calibration scheme requires independent determination of the wavelength of the laser which is specified by the manufacturer to be $1310 \text{ nm} \pm 0.01 \text{ nm}$. Additionally, this assumes that the pattern seen at the photodiode is the interference due to the Fabry-Perot cavity formed by the beam splitter coating and the mirror on the beam. This was verified by comparing the refelctance measurements to the theory as can be seen in Figure 3.8.

3.2.5 Mass Adjustment

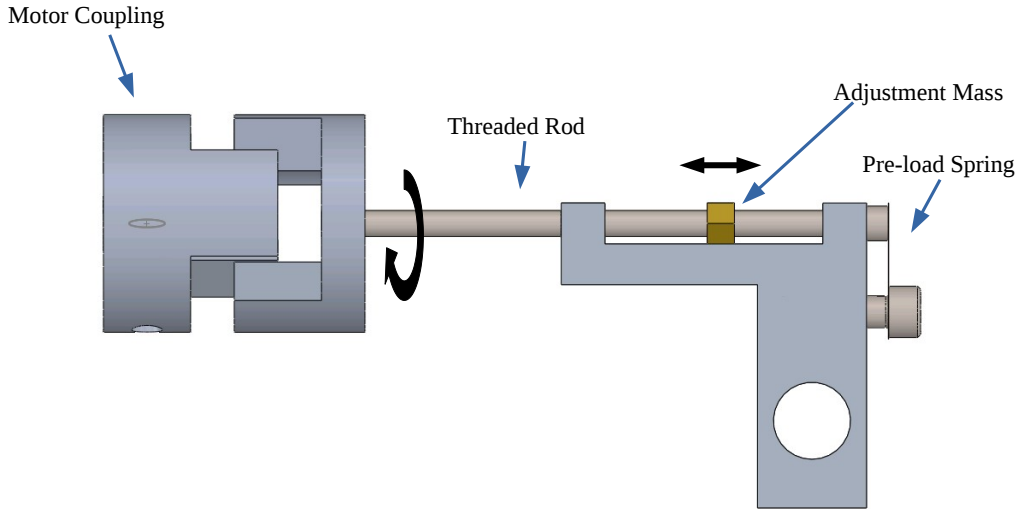


Figure 3.9: CAD rendering of the cBRS mass adjuster

Through a variety of mechanisms, both the BRSs and the cBRS can undergo long term drifts of the equilibrium position that can drive the beam-balance past the dynamic range of the readout. To counteract this, a mass on the balance can be moved or added to shift the center of mass as follows:

$$\Delta\theta = \frac{g}{\kappa}mr \quad (3.6)$$

where $\Delta\theta$ is the change in equilibrium angle, g is the gravitational acceleration, κ is the spring constant of the flexure, m is the mass added, and r is the distance from the mass and

the pivot point.

While for the BRS the horizontal center of mass (COM) was designed to be tuned by hand, for the cBRS to operate within the LIGO vacuum chambers this must be done remotely and in an automated fashion. To achieve this a mass adjuster shown in Figure 3.9 consisting of a small brass mass on a fine pitched screw is attached to the beam-balance. This allows the shifting of the mass with the rotation of the screw.

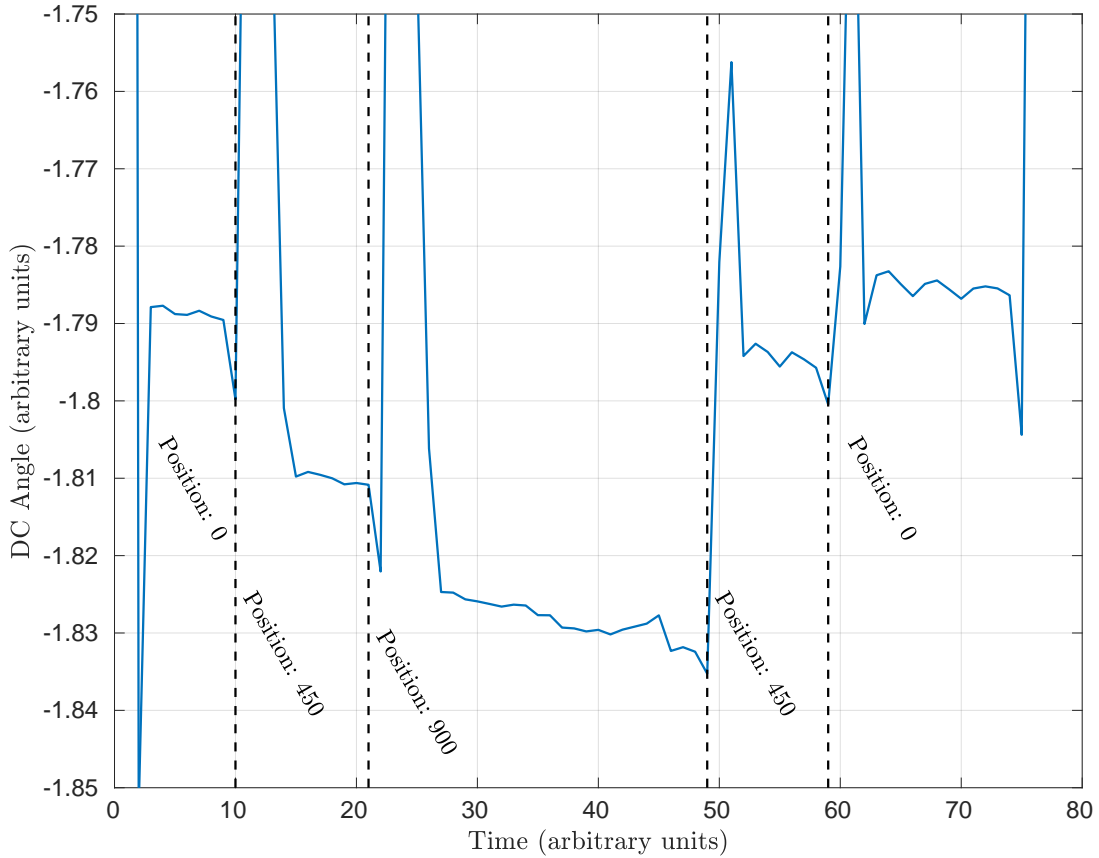


Figure 3.10: Demonstration of the effect of actuating the remote mass adjuster. The DC angle was measured by taking the mean of period long chunks of shadow sensor data while the mass adjuster was shifted to a collection of positions.

In order to avoid mechanically shorting the beam balance with wires, the motor which turns this screw is held on an independent support. The couplers between the motor and the screw are intentionally oversized to allow for decoupling via back rotations. A small shim of beryllium copper is held tightly against the opposite end of the screw to provide spring loading which hold the screws center of mass in place but allow for rotation.

To test whether this design was capable of moving enough mass accurately, a temporary uncalibrated shadow sensor was set up to measure the motion of the cBRS. The actuation of the mass adjuster can be seen in Figure 3.10 which shows the average of period long cuts of the cBRS's resonant motion. In this prototype there is clear hysteresis due to nonuniform friction along the length of the adjuster. However, this was found to not affect the ability to center the cBRS.

3.2.6 Controls

Similar to the BRS, the cBRS can be rung up do to environmental transients which can cause resonant motion in excess of the readout's dynamic range. To decrease these amplitudes, two capacitive actuators are placed under the end masses of the beam. These are actuated with low gain with the angular-readout band-passed around the resonant frequency. This allow for low Q motion during high amplitudes and high Q during low amplitudes.

3.2.7 Noise Performance

The noise performance of the current cBRS prototype, shown in Figure 3.11 is not as well modeled as the BRS, Section 2.2.6, and does not meet the design sensitivity of the instrument. The design sensitivity is determined by extrapolating the high frequency readout noise of $50 \text{ prad}/\sqrt{f}$ down to low frequency and inverting the response described by Equation 2.10.

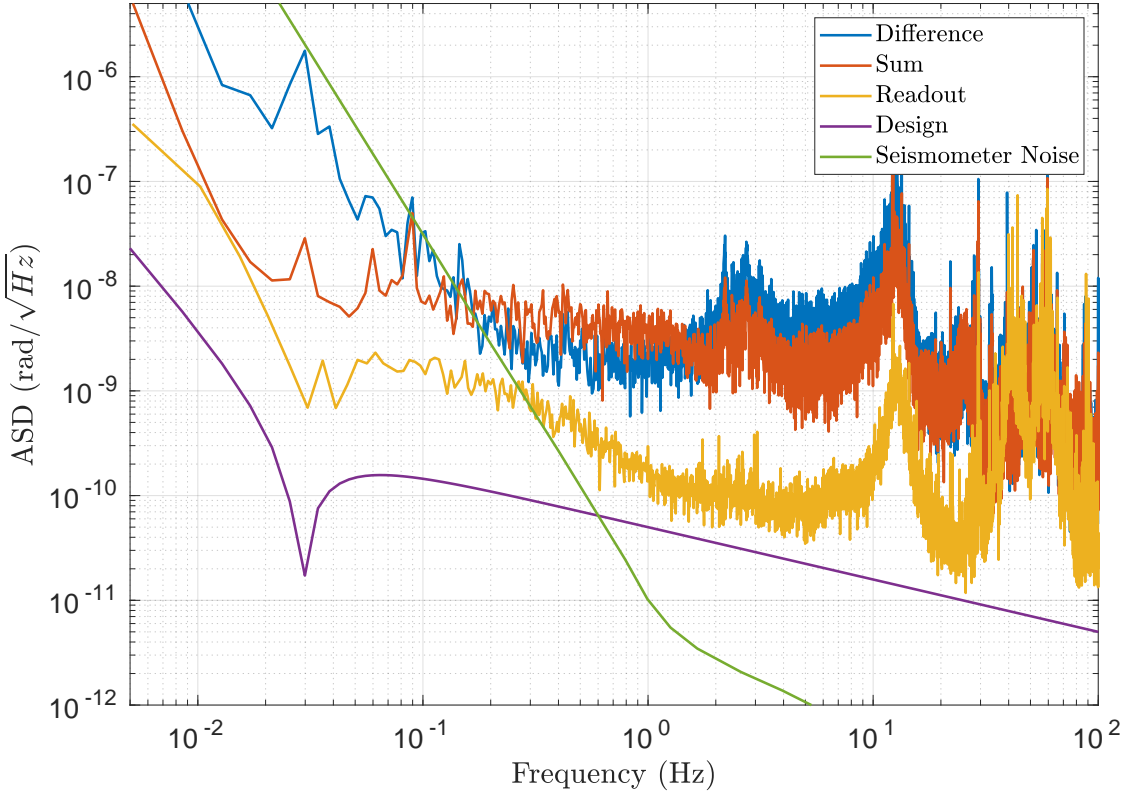


Figure 3.11: Prototype cBRS noise performance showing the sum and difference of the two readouts. Additionally shown is the readout noise measured while the beam balance was mechanically locked, the design sensitivity, and the sensitivity of the current Stage 2 rotational sensors.

3.3 Projected Improvements

3.3.1 Isolation Scheme

As described in Section 1.3, each stage and degree of freedom of the seismic isolation system utilizes a blend of multiple sensors as its feedback signal. These consist of two types of sensors: position sensors which sense differential motion between two stages and inertial sensors which sense the motion relative to an inertial frame. To assess the performance

improvements that could be achieved with the addition of a cBRS into the system, a simple two stage, two degree of freedom model was constructed.

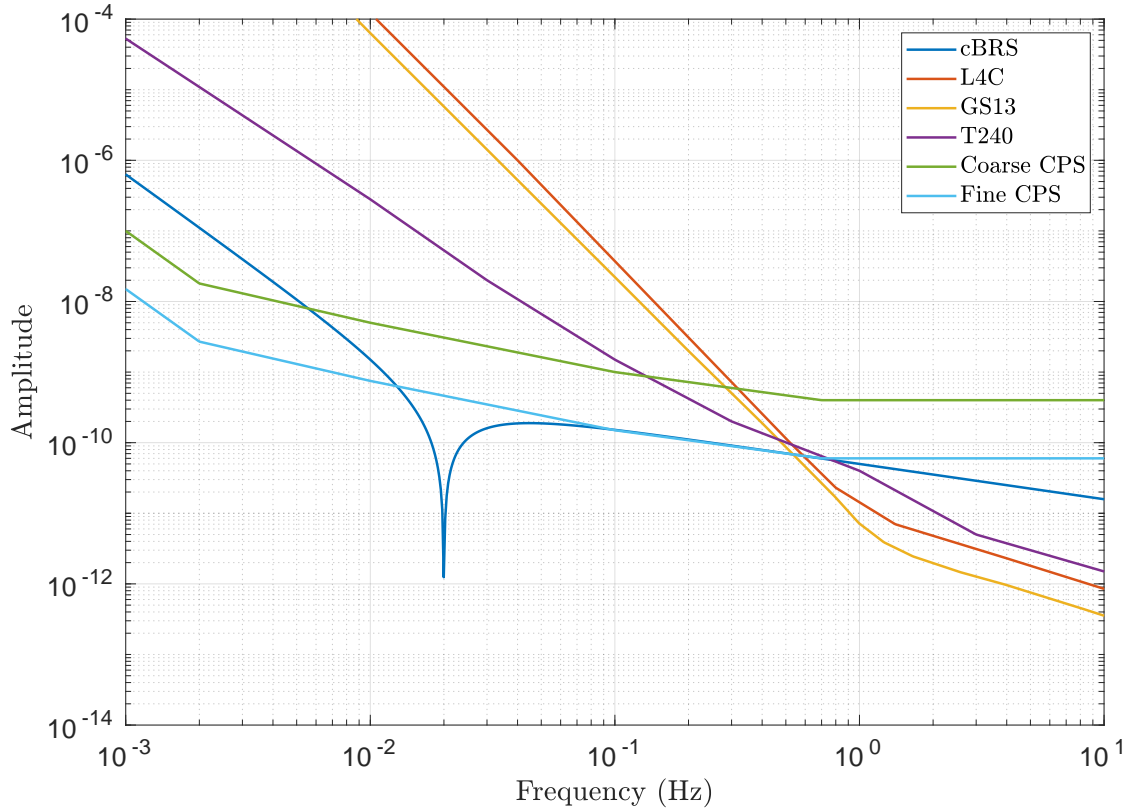


Figure 3.12: Noise models for the cBRS, a collection of seismometers: L4C, GS13, T240, and two types of CPS: Fine, used between Stage 1 and Stage 2, and coarse, used between Stage 0 and Stage 1. Each sensor is in its native units, seismometers and CPS in meters and cBRS in radian. Note that a pair of translational sensors located 1 m apart has roughly the same noise levels in both units.

This model assumes both infinite control authority and no dynamics of the isolation platforms. Additionally, purely theoretical models are used for the input motion and the sensor noises. Although a model which accounts for all six degrees of freedom is required to accurately predict the isolation performance, this simplified model is instructive for compar-

isons of the performance with and without the cBRS. Similar models [26] have been found to match measurements to within a factor of $\sim 2\text{-}3$.

Throughout this model second-order binomial filters are used as the blend filters. In addition, for each stage the inertial sensor noise is taken to be the minimum of the collection of inertial sensors. Realistically these sensors also require precise blending but the details of this blending is negligible below ~ 0.5 Hz. Figure 3.12 shows the noise curves for each sensor used in this model.

Stage 2 Rotational

In order to achieve the lowest suspension point motion, we choose to model a cBRS on the second stage of the isolation. Logistically, this is also the location which currently has enough space to install a device. Due to the rising low frequency noise in the cBRS, tuning where to place the blend frequency becomes a balance of increasing motion at low frequencies and decreasing motion at high and visa versa. The blend frequency was chosen to give a low frequency RMS motion of ~ 10 nrad/ $\sqrt{\text{Hz}}$ which matches the performance without the cBRS, see Figure 3.17. This criteria called for a blend frequency of 12 mHz. The residual tilt for Stage 2 can be approximated by:

$$\theta_2(f) \approx \tilde{F}_{LP2} (\theta_1(f) + \tilde{n}_{CPS-F}(f)) + \tilde{F}_{HP2} \min[\tilde{n}_{cBRS}(f), \tilde{n}_{GS13}(f)] \quad (3.7)$$

where θ_1 is the tilt of Stage 1, \tilde{F}_{LP2} and \tilde{F}_{HP2} are respectively the Stage 2 rotational low and high-pass blend filters, \tilde{n}_{CPS-F} , \tilde{n}_{cBRS} , and \tilde{n}_{GS13} are the rotational sensor noise for the Fine CPS, cBRS, and GS13, respectively. The performance with this loop can be seen in Figure 3.13. Above ~ 500 mHz, the performance is dominated by the GS13 noise and from 80 mHz to 500 mHz it is dominated by cBRS noise. Below 80 mHz, the position sensor contributions become dominate which makes the Stage 2 motion almost equivalent to the Stage 1 motion. The only deviation from Stage 1 motion is near the blend frequency, 12 mHz, where gain peaking added a factor of ~ 3 .

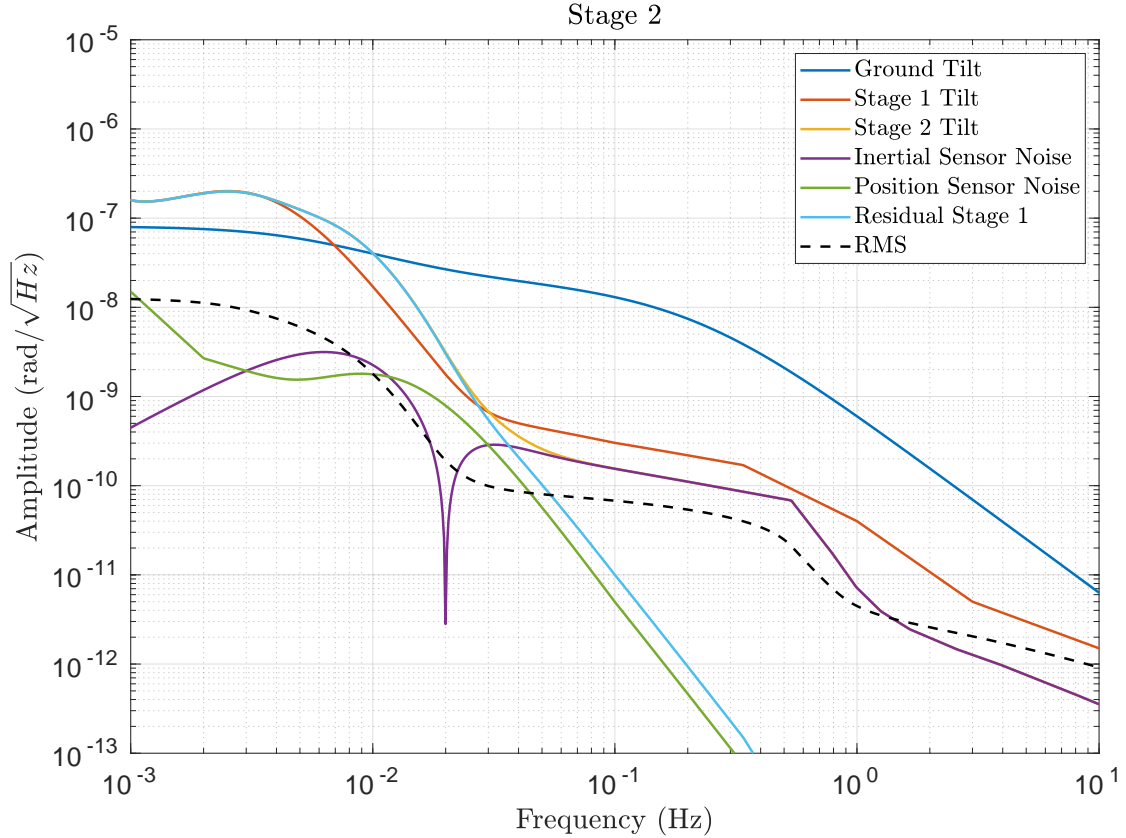


Figure 3.13: Projected rotational performance of Stage 2 of the ISI along with the contributions from the inertial and position sensor. Also shown is the input ground tilt model which represents the observed tilt during windy times and the rotational performance of the Stage 1.

Stage 1 Rotational

With Stage 2 inertially isolated in the rotation degree of freedom above ~ 80 mHz, Stage 1 can achieve superior performance if its control is a combination of the position sensor between the Stage 1 and Stage 2, fine CPS, at high frequencies, and the position sensor between Stage 1 and Stage 0, course CPS, at low. This is effectively using the Stage 2 platform as an inertial proof mass with the fine CPS as a readout. The past scheme was to use a seismometer pair as an inertial rotation sensor for high frequencies and the course CPS at low. Applying the

same criteria as Stage 2 of requiring low frequency RMS motion of ~ 10 nrad/ $\sqrt{\text{Hz}}$ yields a blend frequency of 3 mHz around which the motion is amplified by a factor of ~ 3 because of gain peaking.

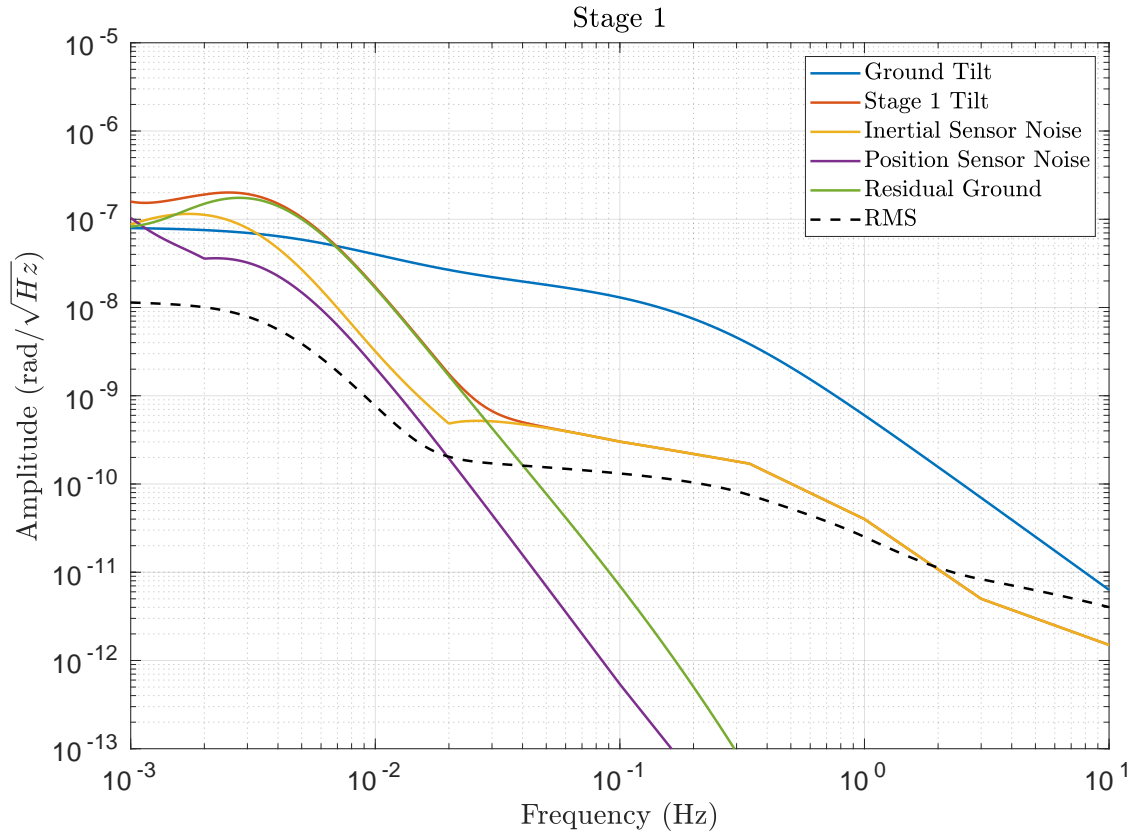


Figure 3.14: Projected rotational performance of Stage 1 of the ISI with, yellow, and without, red, the cBRS. Also shown is the input ground tilt model, blue, which represents the observed tilt during windy times.

The residual tilt for Stage 1 can be approximated by:

$$\theta_1(f) \approx \tilde{F}_{LP1} (\theta_g(f) + \tilde{n}_{CPS-C}(f)) + \tilde{F}_{HP1} \min[(\tilde{n}_{cBRS}(f) + \tilde{n}_{CPS-F}(f)), \tilde{n}_{T240}(f)] \quad (3.8)$$

where θ_g is the ground tilt, \tilde{F}_{LP1} and \tilde{F}_{HP1} are respectively the Stage 1 rotational low and high-pass blend filters, \tilde{n}_{CPS-C} , \tilde{n}_{CPS-F} , \tilde{n}_{cBRS} , and \tilde{n}_{T240} are the rotational sensor noise for the Course CPS, Fine CPS, cBRS, and T240, respectively.

The performance of this design can be seen in Figure 3.14 Below 1 mHz, it is expected the platform motion follows the ground. However, this is omitted as both the ground rotation and sensor noise are not well constrained at low frequency. Above ~ 30 mHz, the residual is dominated by the combination of the sensor noises from the fine CPS, from 30 mHz to 350 mHz, and the T240 pair, above 350 mHz.

A subtlety that arises from using both the fine and course CPS as the control for Stage 1 is that if the Stage 2 blend frequency is placed below the Stage 1 frequency then in between these two frequencies both stages are using the fine CPS as their control. Since the fine CPS measures the motion between the two stages, this effectively makes both stages uncontrolled as they are not referenced to any independent frame. In our model this is avoided by placing the Stage 1 blend frequency a decade lower than the Stage 2 blend.

Stage 1 Translational

Once the rotational degrees of freedom are controlled, the translational loops can begin to be tuned. The primary dependence of the translational performance on the rotational performance comes from tilt contamination of seismometers, described in Section 2.1.1. As with the rotational control loop design, the choice of blend frequency is a trade off between increasing low frequency motion and decreasing high. We choose to require low frequency RMS performance of < 100 nm/s/ $\sqrt{\text{Hz}}$. This requirement is approximately the performance of the current seismic isolation system. A blend frequency of 15 mHz was found to exceed this requirement. The residual motion for Stage 1 can be approximated by:

$$x_1(f) \approx F_{LP1} (x_g(f) + n_{CPS-C}(f)) + F_{HP1} (g/\omega^2 \theta_1(f) + n_{T240}(f)) \quad (3.9)$$

where x_g is the ground motion, F_{LP1} and F_{HP1} are respectively the Stage 1 translational

low and high-pass blend filters, and $n_{\text{CPS-C}}$ and n_{T240} are the translational sensor noise for the Course CPS and T240, respectively.

The performance of the Stage 1 translational isolation with this choice can be seen in Figure 3.15. Above 500 mHz, the performance is limited by the T240 noise. Between 25-500 mHz, residual ground motion dominates and between 1-25 mHz residual tilt coupled through tilt contamination of the seismometers is the primary contribution.

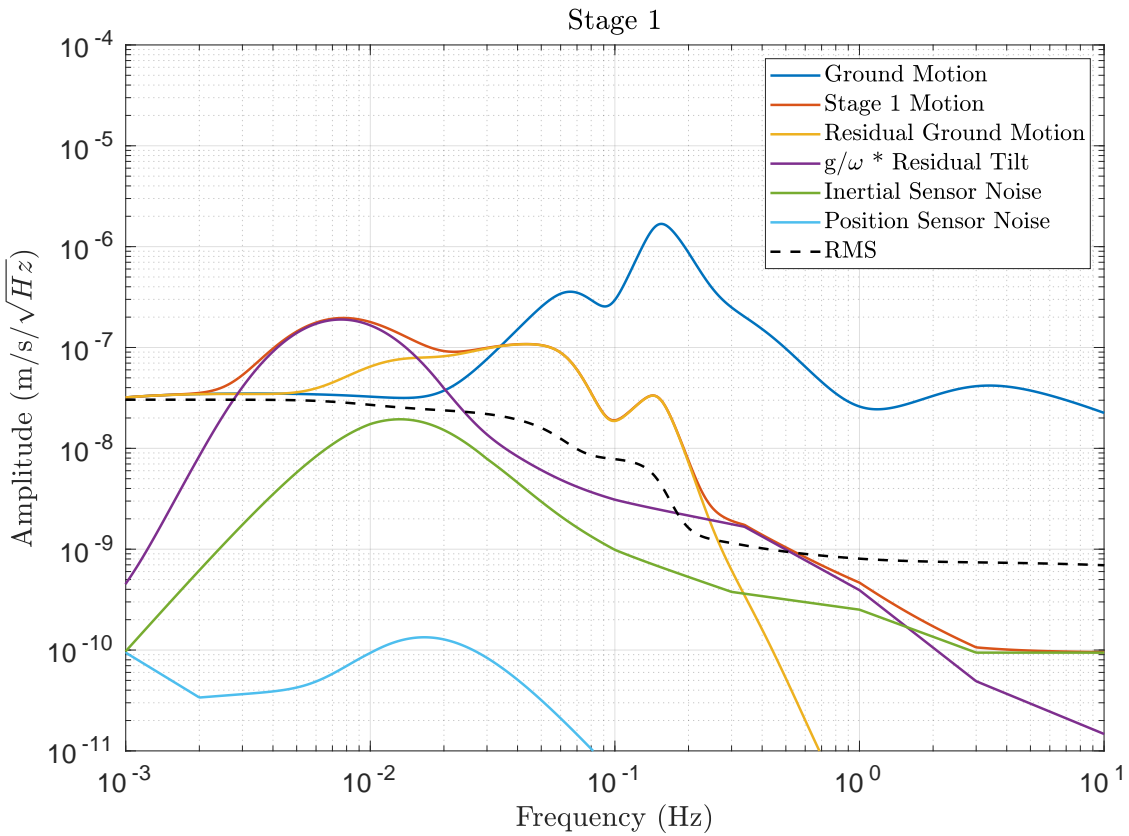


Figure 3.15: Projected translational performance of Stage 1 of the ISI with, yellow, and without, red, the cBRS. Also shown is the input ground motion model, blue, which represents the observed tilt during windy times. The control loops here can be tuned to decrease motion at ~ 100 mHz, the microseism frequencies, by increasing motion at ~ 10 mHz and vice versa.

Stage 2 Translational

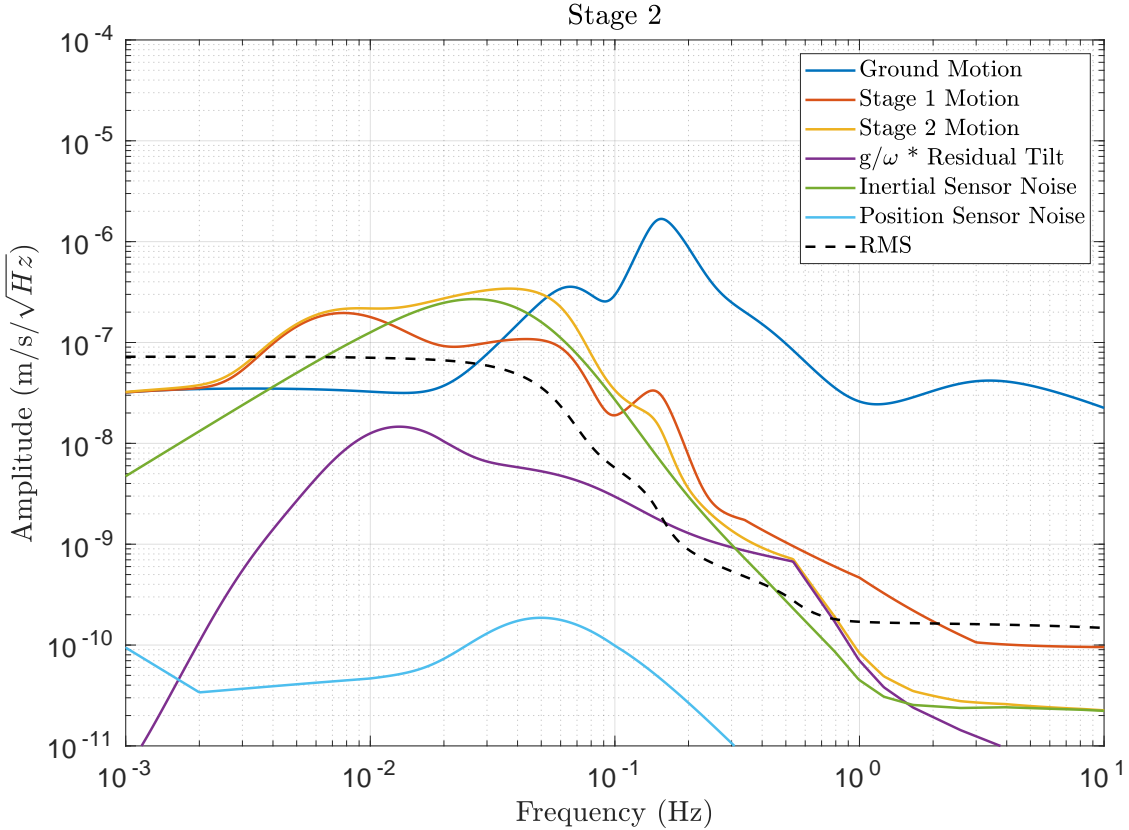


Figure 3.16: Projected translational performance of Stage 2 of the ISI with, yellow, and without, red, the cBRS. Also shown is the input ground motion model, blue, which represents the observed tilt during windy times. The control loops here can be tuned to decrease motion at ~ 100 mHz, the microseism frequencies, by increasing motion at ~ 10 mHz and vice versa.

The Stage 2 translational loops were tuned in a similar manner as Stage 1: requiring that the RMS motion at 1 mHz to be < 100 nm/s/ $\sqrt{\text{Hz}}$. This yielded a blend frequency of 45 mHz. The residual motion for Stage 2 can be approximated by:

$$x_2(f) \approx F_{LP2} (x_1(f) + n_{CPS-F}(f)) + F_{HP2} (g/\omega^2 \theta_2(f) + n_{GS13}(f)) \quad (3.10)$$

where F_{LP2} and F_{HP2} are respectively the Stage 2 translational low and high-pass blend filters, and n_{CPS-F} and n_{GS13} are the translational sensor noise for the Fine CPS and GS13, respectively.

As can be seen in Figure 3.16, this effectively flattens the residual spectrum between $\sim 5\text{-}60$ mHz to an amplitude of $2\text{--}3 \times 10^{-7}$ m/s/ $\sqrt{\text{Hz}}$ while decreasing the microseism at 150 mHz by a factor of ~ 100 .

Of particular interest for future upgrades to the seismic isolation, the limiting term of the Stage 2 translational performance in these models is the noise due to the on-platform inertial sensors whereas previous performance was dominated by the tilt contamination term. [26] This points to the need of lower noise inertial sensors for future systems. This is an active area of research with many promising candidate sensors [31, 32].

Comparison with past performance

To show the improvements relative to the past isolation configurations, the performance of the past isolation system was modeled using the same techniques as described in Section 3.3.1. The filters used here were those that were deployed for O2. These are expertly tuned to account for the true performance of the instruments and thus have more complex shapes than the binomial filters used in the proposed isolation scheme. However, they follow the same general shape as binomial filters.

A comparison of the rotational degree is shown in Figure 3.17. During O2, Stage 2 was locked to Stage 1 in the rotational degree of freedom using the position sensors across the entire band of interest. Thus the performance of the two stages was identical. With the addition of the cBRS the residual tilt is decreased by a factor of ~ 50 and ~ 100 respectively for Stage 1 and Stage 2 between 50-250 mHz. Between 1-10 mHz the residual tilt is increased by a factor of ~ 3 . Below 1 mHz it is expected that the two schemes have identical performance. However, the ground tilt is not well modeled due to the lack of sub-mHz rotation sensors so this is omitted from this model.

The performance comparison of the translational degree isolation system is shown in

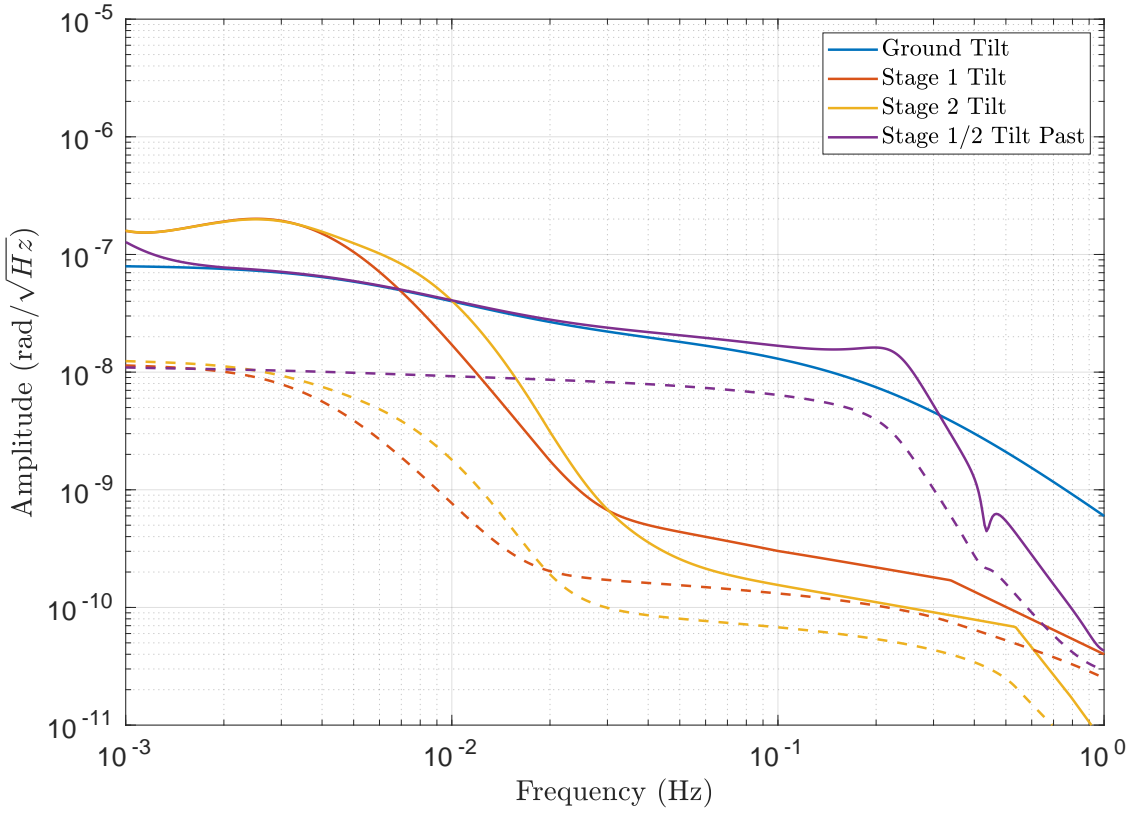


Figure 3.17: Comparison of the rotational isolation performance of Stage 2 during O2 and the projected performance with the inclusion of the cBRS. During O2, the rotational performance of the two stages was identical since they were locked together using the position sensors.

Figure 3.18. Above 1 Hz, the performance of the two schemes are similar as lowest noise sensors at those frequencies have not changed. At the secondary microseism, 100-500 mHz, the inclusion of the cBRS yields a factor of ~ 20 improvement of the residual motion while at the primary microseism, 50-100 mHz, it yields a factor of ~ 3 . With the cBRS, the residual motion between 3-30 mHz is increased by a factor of ten. However, the RMS motion at those frequencies is still below the previous performance. It is expected that the control loops downstream will be able to compensate for this increase in motion without any decrease in performance. Below 2 mHz, both schemes follow the ground since the dominate sensors

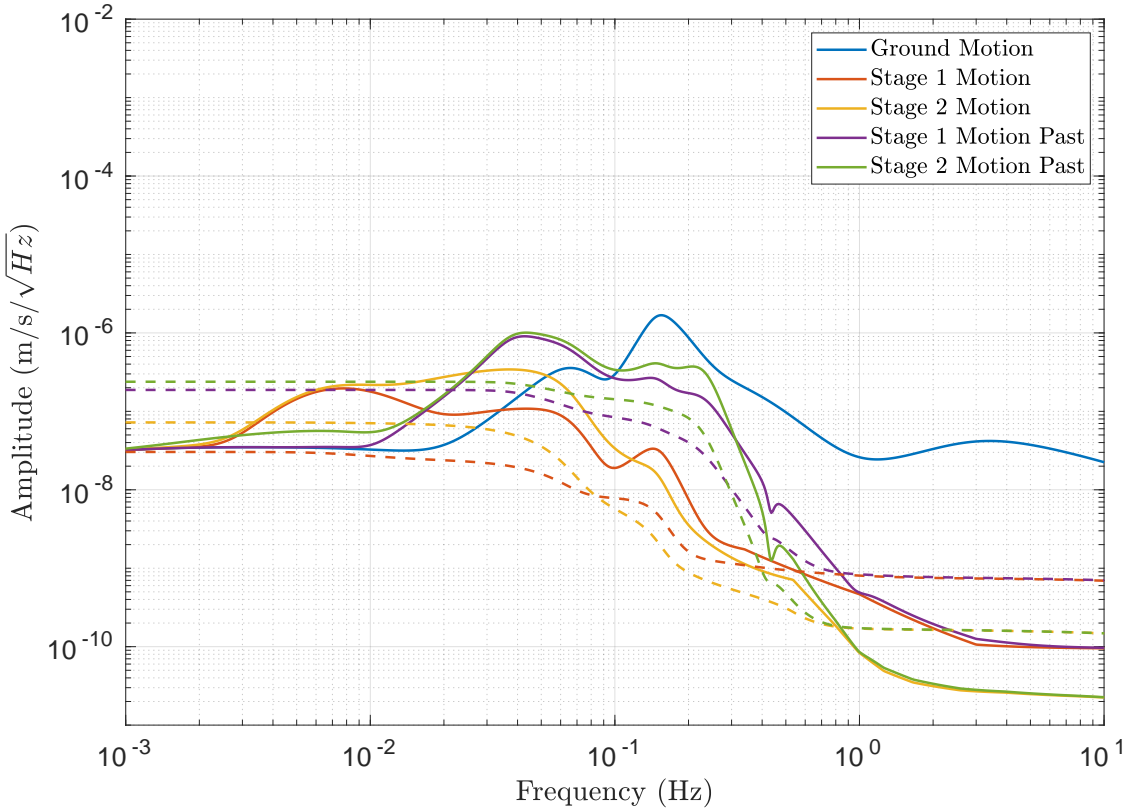


Figure 3.18: Comparison of the translational isolation performance during Q2 and the projected performance with the inclusion of the cBRS.

at those frequencies are the position sensors.

Although in reality the control loop for each isolation platform will have to be tuned individually, these models show that one can expect a significant decrease in residual motion with the deployment of the cBRS.

3.3.2 Angular Control Performance

As mentioned in Section 3.1, the most immediate effect of the increased performance of the seismic isolation with the inclusion of a cBRS is the ability to retune the angular sensing and

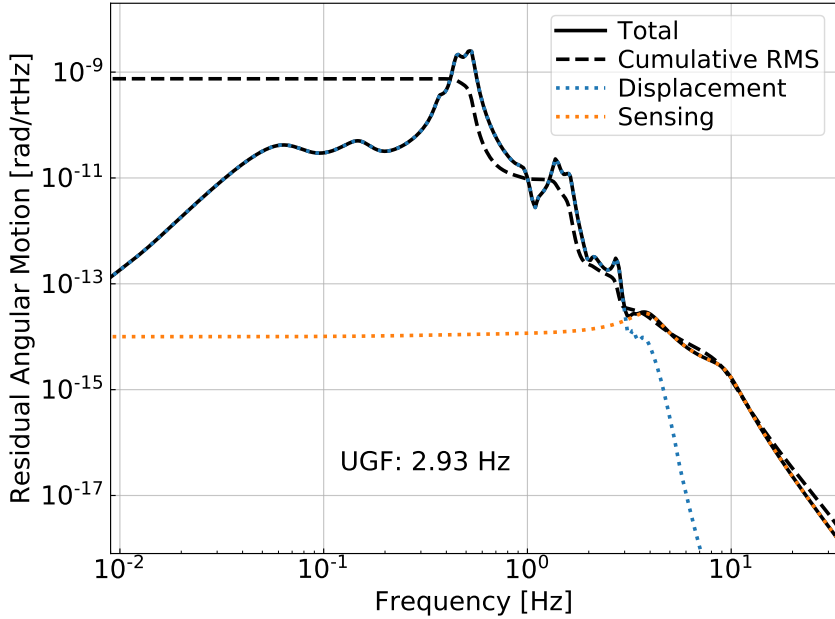


Figure 3.19: Projected performance of the angular sensing and control system with the seismic performance described in Section 3.3.1.

control (ASC) loops. In order to estimate the possible ASC performance for a given seismic performance, a simplified model was constructed which takes the motion of the suspension point as an input, optimizes a theoretical control loop, and outputs the expected residual angular motion of the test mass. The control loop is optimized to give the best performance at high frequencies while maintaining a low frequency RMS residual of $1 \text{ nrad}/\sqrt{\text{Hz}}$.

This model uses a handful of approximations that do not necessarily hold in reality. First off, this is only modeling the performance of a single test mass yet to predict the effect on the differential strain, all four test masses would need to be modeled. Additionally, it ignores the effects of radiation pressure which become important at high laser powers. [30] However, it is believed that the seismic isolation performance at low frequencies is the limiting factor in the current observatories and thus is captured by this model.

The performance of the ASC system was modeled for both the seismic performance with, Figure 3.19, and without, Figure 3.1, the cBRS installed. In both situations, the high frequency performance is limited by sensor noise which leaks into the gravitational wave band. The primary retuning that can be made with the inclusion of the cBRS is to decreasing the ASC UGF from 5.23 Hz to 2.93 Hz. Above this the residual falls off as $1/f^5$.

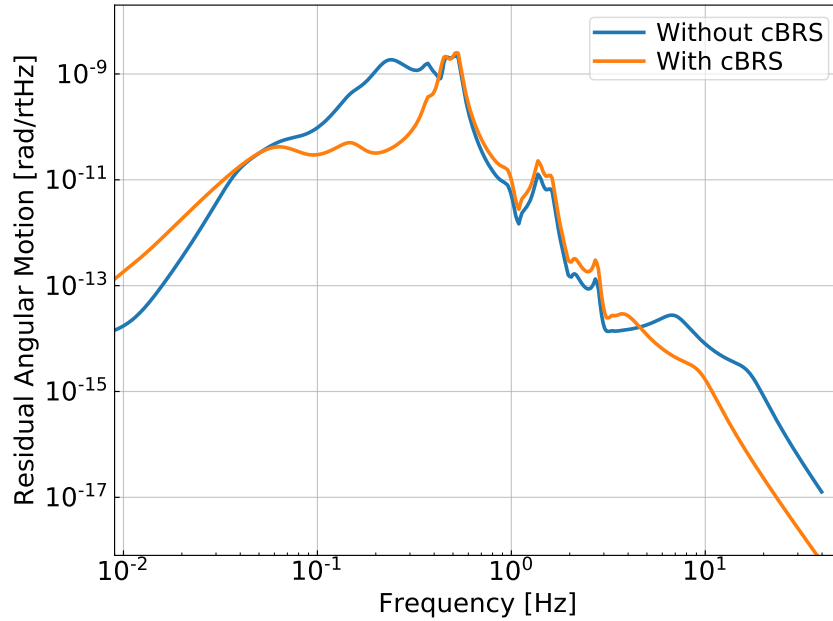


Figure 3.20: Comparison of the ASC performance with and without the cBRS

A comparison of the modeled residual for a system with and without the cBRS is shown in Figure 3.20. As expected, adding the cBRS reduces the residual between $\sim 50\text{-}500$ mHz due to the increased performance of the seismic isolation system. This allows a shift in the UGF to lower frequencies which reduces the residual above ~ 5 Hz.

This decrease in residual motion above ~ 5 Hz would directly decrease noise in the differential strain readout of the observatory as shown in Figure 3.21. It should be stressed that

for an accurate prediction of the strain noise, one would need to include the contributions from all four test masses and their couplings due to radiation pressure. However, this model suggests that with the future installation of the cBRS one would expect roughly an order of magnitude reduction in the low frequency noise in the gravitational wave channel bringing the noise closer to the aLIGO design sensitivity.

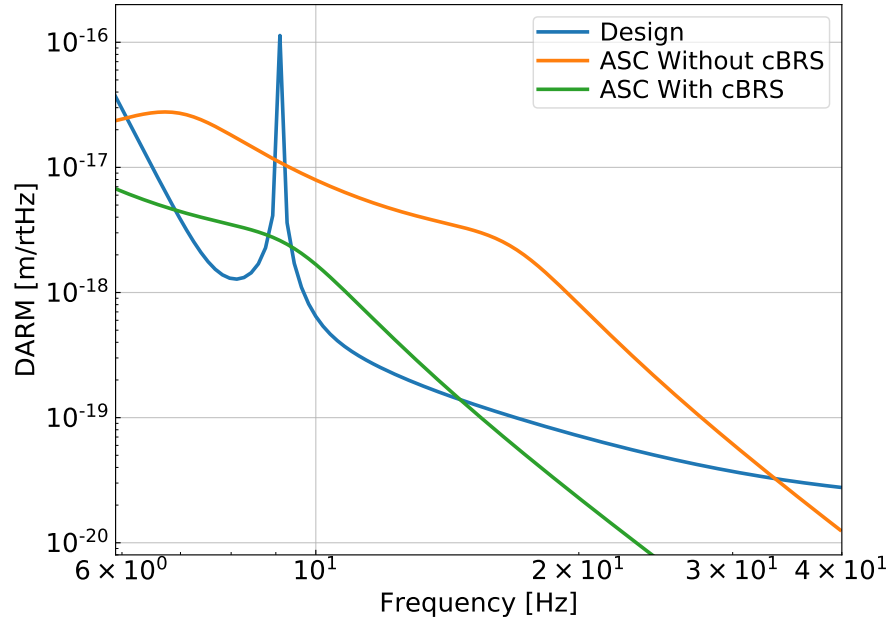


Figure 3.21: Projected low frequency strain noise with and without the cBRS. The blue line is the current sensitivity of LLO, the orange is the aLIGO design sensitivity, green is the modeled noise contribution of the current ASC system, and red is the improved ASC noise contribution with the seismic isolation described in Section 3.3.1.

Chapter 4

AUXILIARY APPLICATIONS

With every novel sensor comes novel science. Thus the development of these highly sensitive rotation sensors have opened up a handful of novel scientific avenues, tangential to seismic isolation, that have been explored.

4.1 Geophysics

Seismic waves have six components, three translations and three rotations, however seismology has long neglected the rotational components due the lack of sensitive rotation sensors. Recent developments have begun to alleviated this issue with the advent of seismically relevant ring laser gyros. [33] The rotation sensors described in Chapter 2 and 3 join a small class of ground rotation sensors that are sensitive at low frequencies and have low translational coupling which allow for the use in seismology.

4.1.1 Rayleigh Wave Theory

Seismic waves can be broken into two classes: body waves and surface waves. In regard to surface waves there are two polarization: Love waves and Rayleigh waves. The motion caused by a Love wave is constrained to the plane parallel with the surface of the medium while Rayleigh waves are constrained to a plane perpendicular the surface.

The plane wave solution of a Rayleigh wave has six components ($u_x, u_y, u_z, \theta_x, \theta_y, \theta_z$) where u_i designated the translational motion in the i th direction while θ_i is the rotation

about the i th axis. These can be described as with the following [34]

$$u_x(\mathbf{r}, t) = \alpha \sin(\zeta) \cos(\phi) \cos(\omega t - \mathbf{k} \cdot \mathbf{r}) \quad (4.1)$$

$$u_y(\mathbf{r}, t) = \alpha \sin(\zeta) \sin(\phi) \cos(\omega t - \mathbf{k} \cdot \mathbf{r}) \quad (4.2)$$

$$u_z(\mathbf{r}, t) = \alpha \cos(\zeta) \cos(\omega t - \mathbf{k} \cdot \mathbf{r} + \pi/2) \quad (4.3)$$

$$\theta_x(\mathbf{r}, t) = \frac{\partial u_z}{\partial y} = \alpha \kappa \cos(\zeta) \sin(\phi) \cos(\omega t - \mathbf{k} \cdot \mathbf{r}) \quad (4.4)$$

$$\theta_y(\mathbf{r}, t) = -\frac{\partial u_z}{\partial x} = -\alpha \kappa \cos(\zeta) \cos(\phi) \cos(\omega t - \mathbf{k} \cdot \mathbf{r}) \quad (4.5)$$

$$\theta_z(\mathbf{r}, t) = \frac{1}{2} \left(\frac{\partial u_y}{\partial x} - \frac{\partial u_x}{\partial y} \right) = 0 \quad (4.6)$$

where α is the amplitude, ζ is the ellipticity angle, ϕ is the angle of incidence in the horizontal plane, ω is the frequency, and $\mathbf{k} = \kappa(\cos(\phi), \sin(\phi), 0)$ is the wavevector.

These components can be seen in Figure 4.1 which shows the seismic waves sourced by a M 7.9 earthquake in Papua New Guinea as seen by instruments installed at the End-Y station of the LIGO Hanford Observatory (LHO). The translations were measured by a broadband three-component seismometer while the rotation was sensed by a Beam Rotation Sensor (BRS) described in Chapter 2. As one would expect from Eq. 4.3 and 4.4, the vertical velocity and the rotation differ only by a constant factor related to the phase velocity and the angle of incidence. Additionally, a large amplitude Love wave is apparent starting at ~ 1200 seconds which neither the vertical seismometer or the BRS experiences due to the waves' lack of vertical component.

From Equations 4.1-4.3 it can be seen that with only a traditional 3-axis seismometer, it is impossible to measure all five parameters that define this wave-field. ¹Additionally, the horizontal components, u_x and u_y can contain contributions from co-propagating Love waves which further muddles ones ability to extract parameters.

¹With an array of vertical seismometer four parameters: frequency, angle of incidence, wavenumber, and amplitude, can be readily measured.

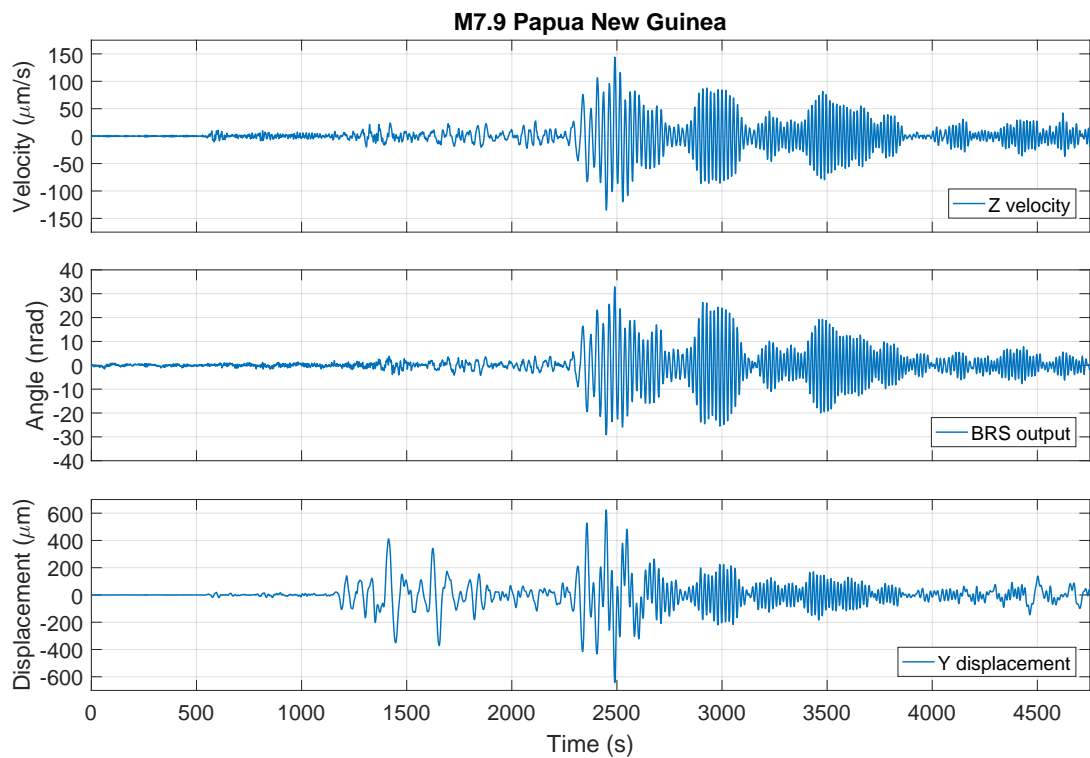


Figure 4.1: Observations of the seismic waves emanated from a M7.9 earthquake in Papua New Guinea as seen by instruments installed at the End-Y Station of LHO. [35] Both the Z velocity and Y displacement were measured by a broadband three-component seismometer while the rotation was measured by a BRS described in Chapter 2.

4.1.2 Wave-Field Parameter Extraction

With the combined measurements of the translational and rotational components at a single station, one can extract wavefield parameters that would otherwise be difficult to obtain, namely the phase velocity and angle of incidence.

Seismic wave phase velocities are common observables which not only allows for understanding of Rayleigh wave propagation but can be inverted to yield tomographical structure profiles of the interior of the earth. [36] The traditional method of extracting these is by exploiting the time of arrival of a wave as it passes through an array of many seismometers. The analysis can be constrained to only the vertical channel as it is insensitive to Love waves which could contaminate the measurements. However, this method requires many devices and effectively averages over the size of the array.

Alternatively, with measurements of the rotational components, a point-like measurement of the phase velocity can be made with three devices, a 3-component seismometer and two horizontal rotation sensors. This can be shown in the following equations:

$$v \equiv \frac{\omega}{\kappa} = \frac{\dot{u}_z}{\theta_x} \sin(\phi) \quad (4.7)$$

$$v = \frac{\dot{u}_z}{\theta_y} \cos(\phi) \quad (4.8)$$

$$v = \frac{\dot{u}_z}{\sqrt{\theta_x^2 + \theta_y^2}} \quad (4.9)$$

where the dot represents the temporal derivative. Equations 4.7 and 4.8 can be utilized if a station has only one horizontal rotation sensor but requires independent determination of ϕ , the angle of incidence. In contrast, Equation 4.9 contains only information from a single station.

In addition to the phase velocity, the angle of incidence can be determined with the

following:

$$\phi = \arctan\left(\frac{\theta_x}{\theta_y}\right) \quad (4.10)$$

Although in theory, this can be measured using a single seismometer, Love wave contamination of the horizontal translational channels would distort any such measurement. As the horizontal rotational channels are insensitive to Love waves, they allow the extraction of ϕ without such contamination.

4.1.3 Single Station Dispersion Measurements

As described in Section 2.3.1, two BRSs were installed at LHO, one at each end station located 5.66 meters apart. The End-X BRS was found to have a $\delta = 30 \mu\text{m}$ leading to a translational coupling of $2 \times 10^{-4} \text{ rad/m}$ while the End-Y BRS was found to have a coupling of $1 \times 10^{-6} \text{ rad/m}$ with a $\delta < 0.5 \mu\text{m}$. This limited any seismic studies using these devices to use only the End-Y BRS as the End-X BRS was contaminated with translational motion.

Between April, 2016 and January, 2017, six earthquakes were measured during environmentally quite times at the observatory. [35] With application of Equation 4.7 the phase dispersion curve at the End-Y Station was measured with instruments installed at a single station. Corrections of the angle of incidence were determined by an array of seismometers installed at LHO which were verified via great circle calculations. Additionally, the phase velocity was estimated in a more traditional manor using the signal delay between the array of seismometer at LHO. The measure phase dispersion curve is shown in Figure 4.2 which shows good agreement between the two methods. For more detail see Reference [35]

These measurements display the utility of including rotation sensors in seismic instruments. If a seismic station was constructed with two orthogonally oriented horizontal rotation sensors and a vertical seismometer, the phase velocity could be measured independent of angle of incidence by utilizing Eq. 4.9. Neglecting the logistical difficulty, one could imagine constructing arrays of station with both translational and rotational sensors. This would

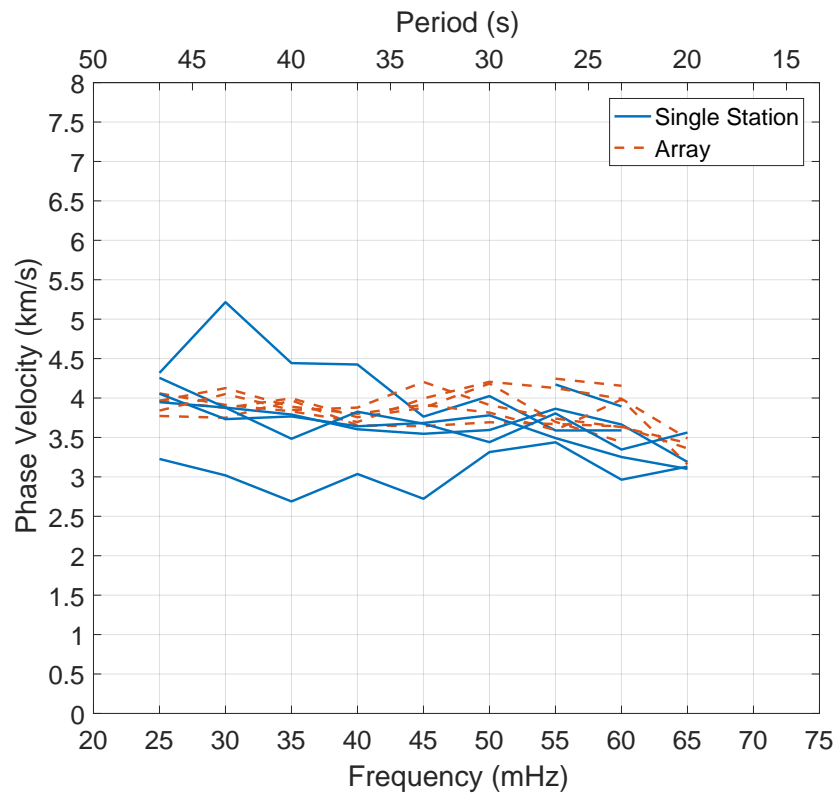


Figure 4.2: Rayleigh wave phase velocity measurements made by instruments located at the End-Y station of LHO, blue, and the same measurements achieved by the array of seismometers deployed at LHO. Each line represent the measurements achieved by different earthquakes. The angle of incidence of each wave was measured independent of the single station and used within the analysis. [35]

allow mapping of the phase dispersion curves, and thus tomography, with spatial resolution limited only by the size of the instruments. Such stations could also be installed within traditional arrays to yield independent point-like measurements to further constrain tomographic studies.

4.2 Newtonian Noise

4.2.1 Theory

The gravitational coupling between the environment and an interferometer's test masses, so called Newtonian noise, is expected to limit the performance of terrestrial gravitational wave detectors in the near future [37]. Sources of the gravitaitional field variations can range from atmospheric density changes to vibrations of the laboratory structures [38]. This coupling is unique in the fact that it can not be shielded or trivially engineered away. One can move an observatory underground to decrease the strength of the atmospherically driven fluctuations and those caused by seismic surface waves, discussed in detail in the following section. However, this process is both expensive and does not remove the sources which come from operating an instrument such as the vibrations of the vacuum structure or seismic motion sourced by laboratory equipment.

For the current surface-level interferometric observatories, the seismic motion due to Rayleigh waves is thought to be the dominant contributor to the Newtonian noise and will be the limiting noise source between 8-20 Hz [39]. The motion due to a plane Rayleigh wave follows:

$$u_z(\mathbf{r}, t) = u_z \cos(\omega t - \mathbf{k} \cdot \mathbf{r} + \pi/2) \quad (4.11)$$

where $u_z = \alpha \cos(\zeta)$, α is the amplitude, ζ is the ellipticity angle, ϕ is the angle of incidence in the horizontal plane, ω is the frequency, and $\mathbf{k} = \kappa(\cos(\phi), \sin(\phi), 0)$ is the

wavevector. The corresponding test mass acceleration in the x-direction follows [40]:

$$a_x(\mathbf{r}, t) = 2\pi u_z \gamma G \rho_0 e^{-h\kappa} \cos(\phi) \cos(\omega t - \mathbf{k} \cdot \mathbf{r}) \quad (4.12)$$

where G is the gravitational constant, ρ_0 is the density of the ground, h is the height of the test mass from the ground, and $\gamma \approx 0.8$ is a factor which accounts for the counter-action of the change of density due to the seismic wave and the vertical motion of the ground.

At first glance, these equations appear to suggest that one could predict the test mass acceleration for a given vertical seismometer signal. Such a prediction would allow for high quality subtraction of the Newtonian Noise from an observatory's data stream. However, true seismic wave-fields are not composed of stationary Rayleigh waves but instead are comprised of the sum of many desperate sources which may change their amplitude and phase in time. With this consideration, the phase difference between Eq. 4.11 and 4.12 and the lack of angle of incidence dependence in Eq. 4.11 destroy the ability to use a single vertical seismometer as a reliable sensor for Newtonian noise subtraction.

On the other hand, a horizontal seismometer described by Eq. 4.1 is both in-phase with the Newtonian noise signal and has the same angular dependence. However, seismic wave-fields also include Love waves which have horizontal components but no vertical. This contaminates these channels and would decrease the correlation between the horizontal seismometer and the Newtonian noise.

Finally, the tilt, being the rotation about the y-axis, due to a Rayleigh wave is described by the following:

$$\theta_y(\mathbf{r}, t) = \frac{\partial u_z}{\partial x} = u_z \kappa \cos(\phi) \cos(\omega t - \mathbf{k} \cdot \mathbf{r}) \quad (4.13)$$

The tilt is thus both in-phase, has the same angular dependence, and does not include Love waves. The lack of Love waves can be seen in Figure 4.1 when the horizontal seismometer experiences a large Love wave at around 1200 s while the rotation sensor sees no such signal. The tilt signal and the Newtonian noise are thus related by a handful of parameters

which can be measured independently or determined empirically and are not expected to vary in time. This points to the conclusion that a tiltmeter is the ideal sensor for Newtonian noise subtraction

4.2.2 Observations

During LIGO’s second observing run (O2), a prototype cBRS, described in Chapter 3, was installed at the corner station of the LIGO Hanford Observatory along side an array of vertical seismometers. The aim of this deployment was to investigate the Newtonian noise coupling and to test subtraction schemes. Ideally, one would place a rotation sensor directly below one of the test mass as the Newtonian noise acting on the mirror is dominated by the ground just beneath it. However, the cBRS was too large to be placed underneath the vacuum chamber which holds the test mass so it was placed just next to the vacuum chamber as can be seen in Figure 4.3.

The first goal of this instrumentation deployment was to assess the ability to combine an array of vertical seismometers to significantly subtract Newtonian noise. Unfortunately, the observatory was not sensitive enough to observe Newtonian noise with high signal-to-noise. Thus the cBRS was used as a proxy for the signal that would be seen by a future observatory. In order to achieve the combination of the 30 seismometer signals which optimally approximates the cBRS signal, a Weiner filter was constructed using seismometers as the references and the cBRS as the target.

The results of this subtraction can be seen in Figure 4.4 [41] which shows that a single seismometer can achieve a factor of ~ 1.5 reduction while the combination of all 30 seismometers achieves a reduction of ~ 10 . This can be understood with Equations 4.11-4.13. The signal from a single vertical seismometer will not have the angular dependence or phase as the tilt. However, the collection of seismometers can simulate the tilt by combining pairs of seismometers to act as effective rotation sensors.

These observations have shown that an array of 30 vertical seismometers can be expected to yield Newtonian noise reduction for future observatories of at least an order of magni-

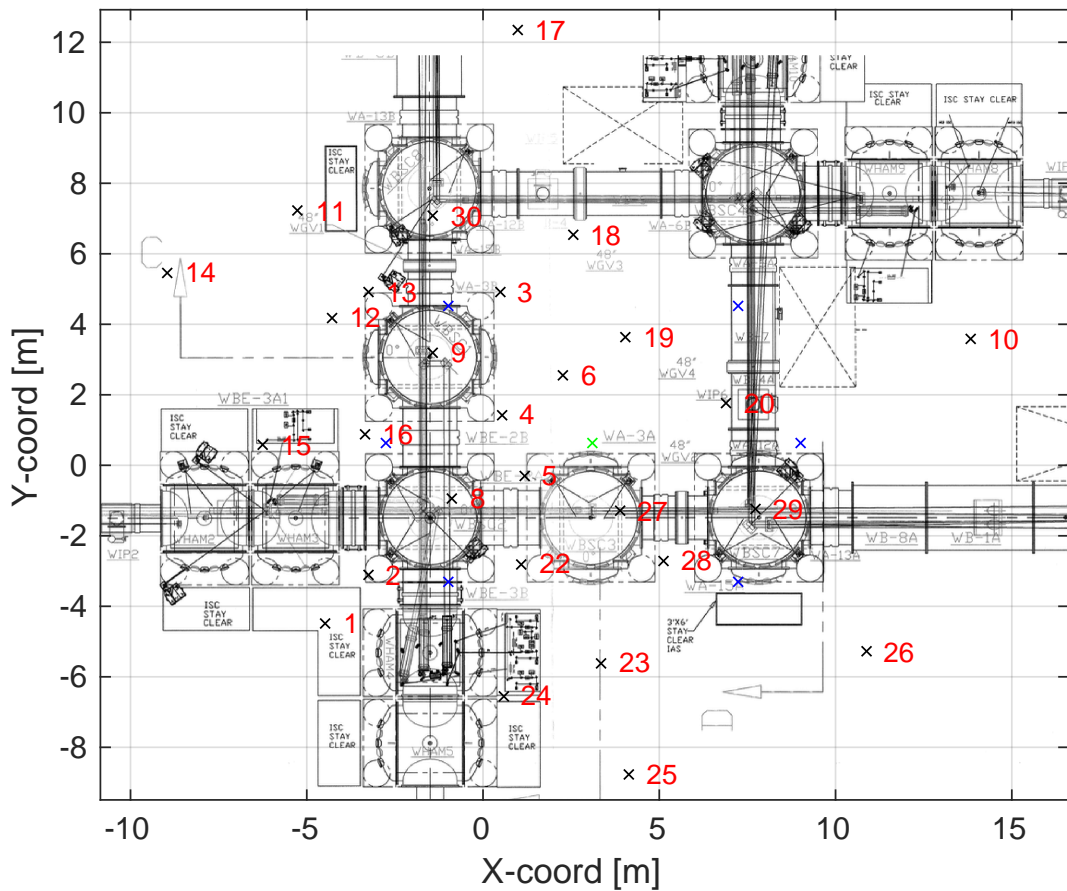


Figure 4.3: The location of the cBRS , marked by the green \times , during O2 alongside the array of seismometers, marked by the black \times s, overlaid on a schematic of the LHO corner station vacuum chambers.

tude. Indeed, similar subtraction was achieved when only the best five seismometers were included as reference channels. This points to the possibility of smaller well placed arrays also achieving similar reduction.

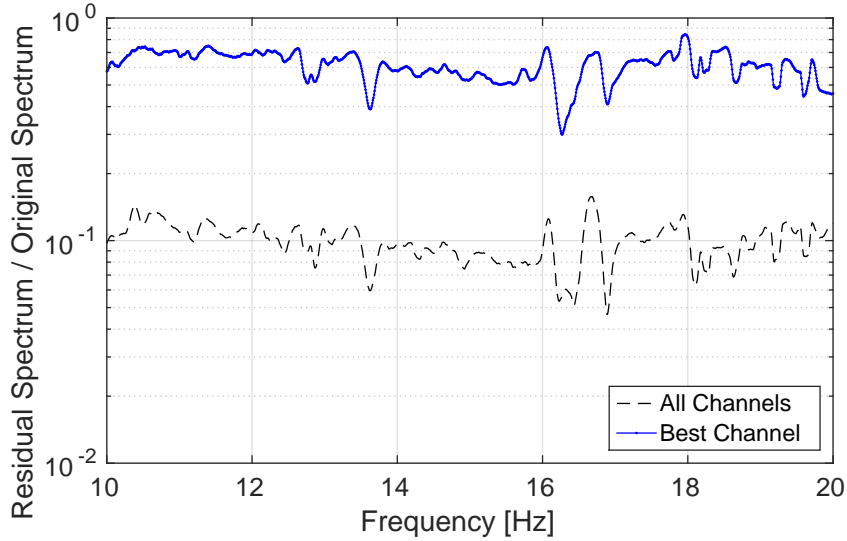


Figure 4.4: Projected Newtonian noise subtraction with the array of seismometers using the cBRS as a proxy for the noise that would be seen by a future observatory.

The second goal of this array was to investigate the coupling between ground tilt and strain for the observatory during O2. This was achieved by calculating the transfer function between the cBRS output and strain using a month of data. The resultant transfer function is shown in Figure 4.5 where it is apparent coupling is observed across many frequencies with a single-to-noise of $\sim 10\text{-}30$. The noise was estimated by recalculating the transfer function with the two data streams shifted relative to one another by 1000 s.

The nature of this coupling can not be known to be of gravitational nature a priori. Thus a collection of possible non-gravitational coupling mechanisms were investigated. [41] Namely, seismic coupling through the seismic isolation system. This path follows from ground tilt to suspension point motion which propagates to the test mass. The transfer function from the ground tilt to suspension point motion can be readily measured using the sensors on the

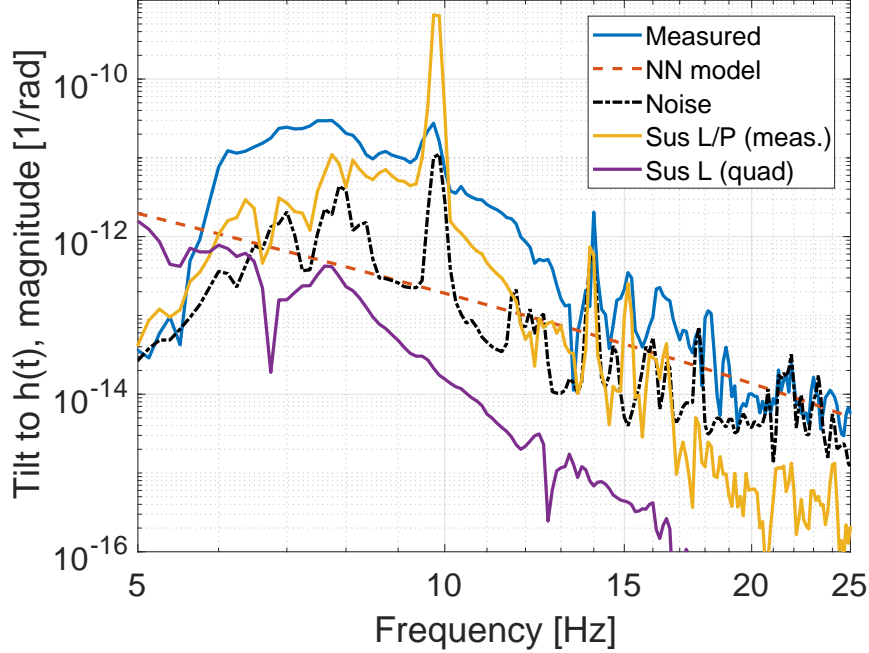


Figure 4.5: Transfer function between the cBRS and the strain output of the interferometer alongside various non-gravitational coupling mechanisms and a model for the Newtonian noise caused by an isotropic, homogeneous Rayleigh wave-field.

isolation platforms. This was then propagated to test mass motion using an analytical model of the suspension, Sus L, and a previously measured transfer function from suspension point to test mass, Sus L/P, which includes both the length and pitch couplings.

These first observations pointed to the possibility that the current observatories are already being affected by Newtonian noise. However, further modeling and investigation [39] found that the distinction between gravitational and non-gravitational coupling is still ambiguous. Deployment of future instruments, including a rotation sensor designed specifically to observe Newtonian noise, should disentangle these couplings and may allow for the first subtraction of Newtonian noise from strain output of the interferometer.

BIBLIOGRAPHY

- [1] Albert Einstein. The foundation of the general theory of relativity. *Annalen Phys.*, 354:769–822, 1916.
- [2] Michele Maggiore. *Gravitational waves: Volume 1: Theory and experiments*, volume 1. Oxford university press, 2008.
- [3] B. P. Abbott et al. Observation of gravitational waves from a binary black hole merger. *Phys. Rev. Lett.*, 116:061102, Feb 2016.
- [4] BP Abbott, R Abbott, TD Abbott, S Abraham, F Acernese, K Ackley, C Adams, RX Adhikari, VB Adya, C Affeldt, et al. Tests of general relativity with the binary black hole signals from the ligo-virgo catalog gwtc-1. *arXiv preprint arXiv:1903.04467*, 2019.
- [5] The LIGO Scientific Collaboration and the Virgo Collaboration. Gw190412: Observation of a binary-black-hole coalescence with asymmetric masses, 2020.
- [6] J. M. Weisberg and Y. Huang. RELATIVISTIC MEASUREMENTS FROM TIMING THE BINARY PULSAR PSR b1913+16. *The Astrophysical Journal*, 829(1):55, sep 2016.
- [7] B. P. Abbott et al. Gw170817: Observation of gravitational waves from a binary neutron star inspiral. *Phys. Rev. Lett.*, 119:161101, Oct 2017.
- [8] BP Abbott, R Abbott, TD Abbott, S Abraham, F Acernese, K Ackley, C Adams, RX Adhikari, VB Adya, C Affeldt, et al. Gw190425: Observation of a compact binary coalescence with total mass $\sim 3.4m_{\odot}$. *arXiv preprint arXiv:2001.01761*, 2020.

- [9] B. P. Abbott et al. Gwtc-1: A gravitational-wave transient catalog of compact binary mergers observed by ligo and virgo during the first and second observing runs. *Phys. Rev. X*, 9:031040, Sep 2019.
- [10] Bernd Brügmann. Fundamentals of numerical relativity for gravitational wave sources. *Science*, 361(6400):366–371, 2018.
- [11] B. P. Abbott et al. All-sky search for continuous gravitational waves from isolated neutron stars using advanced ligo o2 data. *Phys. Rev. D*, 100:024004, Jul 2019.
- [12] BP Abbott, R Abbott, TD Abbott, S Abraham, F Acernese, K Ackley, C Adams, VB Adya, C Affeldt, M Agathos, et al. An optically targeted search for gravitational waves emitted by core-collapse supernovae during the first and second observing runs of advanced ligo and advanced virgo. *arXiv preprint arXiv:1908.03584*, 2019.
- [13] Thibault Damour and Alexander Vilenkin. Gravitational radiation from cosmic (super)strings: Bursts, stochastic background, and observational windows. *Phys. Rev. D*, 71:063510, Mar 2005.
- [14] Richard Easther and Eugene A Lim. Stochastic gravitational wave production after inflation. *Journal of Cosmology and Astroparticle Physics*, 2006(04):010–010, apr 2006.
- [15] J. Aasi et al. Advanced LIGO. *Classical and Quantum Gravity*, 32(7):074001, mar 2015.
- [16] D. V. Martynov, E. D. Hall, B. P. Abbott, R. Abbott, T. D. Abbott, C. Adams, R. X. Adhikari, R. A. Anderson, S. B. Anderson, K. Arai, M. A. Arain, S. M. Aston, L. Austin, S. W. Ballmer, M. Barbet, D. Barker, B. Barr, L. Barsotti, J. Bartlett, M. A. Barton, I. Bartos, J. C. Batch, A. S. Bell, I. Belopolski, J. Bergman, J. Betzwieser, G. Billingsley, J. Birch, S. Biscans, C. Biwer, E. Black, C. D. Blair, C. Bogan, C. Bond, R. Bork, D. O. Bridges, A. F. Brooks, D. D. Brown, L. Carbone, C. Celerier, G. Ciani, F. Clara, D. Cook, S. T. Countryman, M. J. Cowart, D. C. Coyne, A. Cumming, L. Cunningham, M. Damjanic, R. Dannenberg, K. Danzmann, C. F. Da Silva Costa,

E. J. Daw, D. DeBra, R. T. DeRosa, R. DeSalvo, K. L. Dooley, S. Doravari, J. C. Driggers, S. E. Dwyer, A. Effler, T. Etzel, M. Evans, T. M. Evans, M. Factourovich, H. Fair, D. Feldbaum, R. P. Fisher, S. Foley, M. Frede, A. Freise, P. Fritschel, V. V. Frolov, P. Fulda, M. Fyffe, V. Galdi, J. A. Giaime, K. D. Giardina, J. R. Gleason, R. Goetz, S. Gras, C. Gray, R. J. S. Greenhalgh, H. Grote, C. J. Guido, K. E. Gushwa, E. K. Gustafson, R. Gustafson, G. Hammond, J. Hanks, J. Hanson, T. Hardwick, G. M. Harry, K. Haughian, J. Heefner, M. C. Heintze, A. W. Heptonstall, D. Hoak, J. Hough, A. Ivanov, K. Izumi, M. Jacobson, E. James, R. Jones, S. Kandhasamy, S. Karki, M. Kasprzack, S. Kaufer, K. Kawabe, W. Kells, N. Kijbunchoo, E. J. King, P. J. King, D. L. Kinzel, J. S. Kissel, K. Kokeyama, W. Z. Korth, G. Kuehn, P. Kwee, M. Landry, B. Lantz, A. Le Roux, B. M. Levine, J. B. Lewis, V. Lhuillier, N. A. Lockerbie, M. Lormand, M. J. Lubinski, A. P. Lundgren, T. MacDonald, M. MacInnis, D. M. Macleod, M. Mageswaran, K. Mailand, S. Márka, Z. Márka, A. S. Markosyan, E. Maros, I. W. Martin, R. M. Martin, J. N. Marx, K. Mason, T. J. Massinger, F. Matichard, N. Mavalvala, R. McCarthy, D. E. McClelland, S. McCormick, G. McIntyre, J. McIver, E. L. Merilh, M. S. Meyer, P. M. Meyers, J. Miller, R. Mittleman, G. Moreno, C. L. Mueller, G. Mueller, A. Mullavey, J. Munch, P. G. Murray, L. K. Nuttall, J. Oberling, J. O'Dell, P. Oppermann, Richard J. Oram, B. O'Reilly, C. Osthelder, D. J. Ottaway, H. Overmier, J. R. Palamos, H. R. Paris, W. Parker, Z. Patrick, A. Pele, S. Penn, M. Phelps, M. Pickenpack, V. Pierro, I. Pinto, J. Poeld, M. Principe, L. Prokhorov, O. Puncken, V. Quetschke, E. A. Quintero, F. J. Raab, H. Radkins, P. Raffai, C. R. Ramet, C. M. Reed, S. Reid, D. H. Reitze, N. A. Robertson, J. G. Rollins, V. J. Roma, J. H. Romie, S. Rowan, K. Ryan, T. Sadecki, E. J. Sanchez, V. Sandberg, V. Sannibale, R. L. Savage, R. M. S. Schofield, B. Schultz, P. Schwinberg, D. Sellers, A. Sevigny, D. A. Shaddock, Z. Shao, B. Shapiro, P. Shawhan, D. H. Shoemaker, D. Sigg, B. J. J. Slagmolen, J. R. Smith, M. R. Smith, N. D. Smith-Lefebvre, B. Sorazu, A. Staley, A. J. Stein, A. Stochino, K. A. Strain, R. Taylor, M. Thomas, P. Thomas, K. A. Thorne, E. Thrane, K. V. Tokmakov, C. I. Torrie, G. Traylor, G. Vajente, G. Valdes, A. A.

van Veggel, M. Vargas, A. Vecchio, P. J. Veitch, K. Venkateswara, T. Vo, C. Vorvick, S. J. Waldman, M. Walker, R. L. Ward, J. Warner, B. Weaver, R. Weiss, T. Welborn, P. Weßels, C. Wilkinson, P. A. Willems, L. Williams, B. Willke, I. Wilmut, L. Winkelmann, C. C. Wipf, J. Worden, G. Wu, H. Yamamoto, C. C. Yancey, H. Yu, L. Zhang, M. E. Zucker, and J. Zweizig. Sensitivity of the advanced ligo detectors at the beginning of gravitational wave astronomy. *Phys. Rev. D*, 93:112004, Jun 2016.

- [17] M. Tse, Haocun Yu, N. Kijbunchoo, A. Fernandez-Galiana, P. Dupej, L. Barsotti, C. D. Blair, D. D. Brown, S. E. Dwyer, A. Effler, M. Evans, P. Fritschel, V. V. Frolov, A. C. Green, G. L. Mansell, F. Matichard, N. Mavalvala, D. E. McClelland, L. McCuller, T. McRae, J. Miller, A. Mullavey, E. Oelker, I. Y. Phinney, D. Sigg, B. J. J. Slagmolen, T. Vo, R. L. Ward, C. Whittle, R. Abbott, C. Adams, R. X. Adhikari, A. Ananyeva, S. Appert, K. Arai, J. S. Areeda, Y. Asali, S. M. Aston, C. Austin, A. M. Baer, M. Ball, S. W. Ballmer, S. Banagiri, D. Barker, J. Bartlett, B. K. Berger, J. Betzwieser, D. Bhattacharjee, G. Billingsley, S. Biscans, R. M. Blair, N. Bode, P. Booker, R. Bork, A. Bramley, A. F. Brooks, A. Buikema, C. Cahillane, K. C. Cannon, X. Chen, A. A. Ciobanu, F. Clara, S. J. Cooper, K. R. Corley, S. T. Countryman, P. B. Covas, D. C. Coyne, L. E. H. Datrier, D. Davis, C. Di Fronzo, J. C. Driggers, T. Etzel, T. M. Evans, J. Feicht, P. Fulda, M. Fyffe, J. A. Giaime, K. D. Giardina, P. Godwin, E. Goetz, S. Gras, C. Gray, R. Gray, Anchal Gupta, E. K. Gustafson, R. Gustafson, J. Hanks, J. Hanson, T. Hardwick, R. K. Hasskew, M. C. Heintze, A. F. Helmling-Cornell, N. A. Holland, J. D. Jones, S. Kandhasamy, S. Karki, M. Kasprzack, K. Kawabe, P. J. King, J. S. Kissel, Rahul Kumar, M. Landry, B. B. Lane, B. Lantz, M. Laxen, Y. K. Lecoeuche, J. Leviton, J. Liu, M. Lormand, A. P. Lundgren, R. Macas, M. MacInnis, D. M. Macleod, S. Márka, Z. Márka, D. V. Martynov, K. Mason, T. J. Massinger, R. McCarthy, S. McCormick, J. McIver, G. Mendell, K. Merfeld, E. L. Merilh, F. Meylahn, T. Mistry, R. Mittleman, G. Moreno, C. M. Mow-Lowry, S. Mozzon, T. J. N. Nelson, P. Nguyen, L. K. Nuttall, J. Oberling, R. J. Oram, B. O'Reilly, C. Osthelder, D. J. Ottaway, H. Overmier, J. R.

- Palamos, W. Parker, E. Payne, A. Pele, C. J. Perez, M. Pirello, H. Radkins, K. E. Ramirez, J. W. Richardson, K. Riles, N. A. Robertson, J. G. Rollins, C. L. Romel, J. H. Romie, M. P. Ross, K. Ryan, T. Sadecki, E. J. Sanchez, L. E. Sanchez, T. R. Saravanan, R. L. Savage, D. Schaetzl, R. Schnabel, R. M. S. Schofield, E. Schwartz, D. Sellers, T. J. Shaffer, J. R. Smith, S. Soni, B. Sorazu, A. P. Spencer, K. A. Strain, L. Sun, M. J. Szczepańczyk, M. Thomas, P. Thomas, K. A. Thorne, K. Toland, C. I. Torrie, G. Traylor, A. L. Urban, G. Vajente, G. Valdes, D. C. Vander-Hyde, P. J. Veitch, K. Venkateswara, G. Venugopalan, A. D. Viets, C. Vorvick, M. Wade, J. Warner, B. Weaver, R. Weiss, B. Willke, C. C. Wipf, L. Xiao, H. Yamamoto, M. J. Yap, Hang Yu, L. Zhang, M. E. Zucker, and J. Zweizig. Quantum-enhanced advanced ligo detectors in the era of gravitational-wave astronomy. *Phys. Rev. Lett.*, 123:231107, Dec 2019.
- [18] Ligo-virgo cumulative event/candidate rate plot o1-o3.
- [19] BP Abbott, R Abbott, TD Abbott, F Acernese, K Ackley, C Adams, T Adams, P Adesso, RX Adhikari, VB Adya, et al. Gw170817: Measurements of neutron star radii and equation of state. *Physical review letters*, 121(16):161101, 2018.
- [20] Darach Watson, Camilla J Hansen, Jonatan Selsing, Andreas Koch, Daniele B Malesani, Anja C Andersen, Johan PU Fynbo, Almudena Arcones, Andreas Bauswein, Stefano Covino, et al. Identification of strontium in the merger of two neutron stars. *Nature*, 574(7779):497–500, 2019.
- [21] LIGO Scientific Collaboration, Virgo Collaboration, 1M2H Collaboration, Dark Energy Camera GW-EM Collaboration, DES Collaboration, DLT40 Collaboration, Las Cumbrés Observatory Collaboration, VINROUGE Collaboration, MASTER Collaboration, et al. A gravitational-wave standard siren measurement of the hubble constant. *Nature*, 551(7678):85–88, 2017.
- [22] BP Abbott, R Abbott, TD Abbott, S Abraham, F Acernese, K Ackley, C Adams, RX Adhikari, VB Adya, C Affeldt, et al. A gravitational-wave measurement of the

- hubble constant following the second observing run of advanced ligo and virgo. *arXiv preprint arXiv:1908.06060*, 2019.
- [23] B. P. Abbott et al. Gravitational waves and gamma-rays from a binary neutron star merger: GW170817 and GRB 170817a. *The Astrophysical Journal*, 848(2):L13, oct 2017.
 - [24] F. Maticichard et al. Seismic isolation of advanced ligo: Review of strategy, instrumentation and performance. *Classical and Quantum Gravity*, 32(18):185003, 2015.
 - [25] Fabrice Maticichard and Matthew Evans. Tilt-free low-noise seismometry. *Bulletin of the seismological society of America*, 105(2A):497–510, 2015.
 - [26] Krishna Venkateswara, Michael P Ross, Jim Warner, Conor Mow-Lowry, Brian Lantz, Jeffrey Kissel, Hugh Radkins, Thomas Shaffer, Richard Mittleman, Sam Cooper, et al. Towards windproofing ligo: Reducing the effect of wind-driven floor tilt by using rotation sensors in active seismic isolation. *arXiv preprint arXiv:2003.06447*, 2020.
 - [27] Krishna Venkateswara, Charles A. Hagedorn, Matthew D. Turner, Trevor Arp, and Jens H. Gundlach. A high-precision mechanical absolute-rotation sensor. *Review of Scientific Instruments*, 85(1), 2014.
 - [28] T B Arp, C A Hagedorn, Stephan Schlamminger, and J H Gundlach. A reference-beam autocollimator with nanoradian sensitivity from mhz to khz and dynamic range of 10(7.). *The Review of scientific instruments*, 84:095007, 09 2013.
 - [29] Peter R. Saulson. Thermal noise in mechanical experiments. *Phys. Rev. D*, 42:2437–2445, Oct 1990.
 - [30] L Barsotti, M Evans, and P Fritschel. Alignment sensing and control in advanced LIGO. *Classical and Quantum Gravity*, 27(8):084026, apr 2010.

- [31] C M Mow-Lowry and D Martynov. A 6d interferometric inertial isolation system. *Classical and Quantum Gravity*, 36(24):245006, nov 2019.
- [32] S J Cooper, C J Collins, A C Green, D Hoyland, C C Speake, A Freise, and C M Mow-Lowry. A compact, large-range interferometer for precision measurement and inertial sensing. *Classical and Quantum Gravity*, 35(9):095007, mar 2018.
- [33] Simonelli et. al. First deep underground observation of rotational signals from an earthquake at teleseismic distance using a large ring laser gyroscope. *arXiv*, 2016.
- [34] Stefano Maranó and Donat Fäh. Processing of translational and rotational motions of surface waves: Performance analysis and applications to single sensor and to array measurements. *Geophysical Journal International*, 196:317–339, 2014.
- [35] M. P. Ross, K. Venkateswara, C. A. Hagedorn, J. H. Gundlach, J. S. Kissel, J. Warner, H. Radkins, T. J. Shaffer, M. W. Coughlin, and P. Bodin. Low-Frequency Tilt Seismology with a Precision Ground-Rotation Sensor. *Seismological Research Letters*, 89(1):67–76, 11 2017.
- [36] Jordyn C. Babikoff and Colleen A. Dalton. Long-period rayleigh wave phase velocity tomography using usarray. *Geochemistry, Geophysics, Geosystems*, 20(4):1990–2006, 2019.
- [37] Peter R. Saulson. Terrestrial gravitational noise on a gravitational wave antenna. *Phys. Rev. D*, 30:732–736, Aug 1984.
- [38] Jan Harms. Terrestrial gravity fluctuations. *Living reviews in relativity*, 18(1):3, 2015.
- [39] Jan Harms, Edgard Bonilla, Michael Coughlin, Jenne Driggers, Sheila Dwyer, David McManus, Michael Ross, Bram Slagmolen, and Krishna Venkateswara. Observation of a potential future sensitivity limitation from ground motion at ligo hanford. *arXiv preprint arXiv:2001.10889*, 2020.

- [40] Jan Harms and Krishna Venkateswara. Newtonian-noise cancellation in large-scale interferometric GW detectors using seismic tiltmeters. *Classical and Quantum Gravity*, 33(23):234001, oct 2016.
- [41] M. W. Coughlin, J. Harms, J. Driggers, D. J. McManus, N. Mukund, M. P. Ross, B. J. J. Slagmolen, and K. Venkateswara. Implications of dedicated seismometer measurements on newtonian-noise cancellation for advanced ligo. *Phys. Rev. Lett.*, 121:221104, Nov 2018.
- [42] Katherine L Dooley, Lisa Barsotti, Rana X Adhikari, Matthew Evans, Tobin T Fricke, Peter Fritschel, Valera Frolov, Keita Kawabe, and Nicolás Smith-Lefebvre. Angular control of optical cavities in a radiation-pressure-dominated regime: the enhanced ligo case. *JOSA A*, 30(12):2618–2626, 2013.
- [43] W. H. K Lee, M. Celebi, M. I. Todorovska, and H. Igel. Introduction to the special issue on rotational seismology and engineering applications. *Bulletin of the Seismological Society of America*, 99(2B):945–957, 2009.
- [44] Chin-Jen Lin, Han-Pang Huang, Nguyen Dinh Pham, Chun-Chi Liu, Wu-Cheng Chi, and William H. K. Lee. Rotational motions for teleseismic surface waves. *Geophysical Research Letters*, 38(15):n/a–n/a, 2011. L15301.
- [45] M. Reinwald, M. Bernauer, H. Igel, and S. Donner. Improved finite-source inversion through joint measurements of rotational and translational ground motions: a numerical study. *Solid Earth*, 7(5):1467–1477, 2016.
- [46] A. Pancha, T. H. Webb, G. E. Stedman, D. P. McLeod, and K. U. Schreiber. Ring laser detection of rotations from teleseismic waves. *Geophysical Research Letters*, 27(21):3553–3556, 2000.
- [47] Jacopo Belfi, Nicolò Beverini, Giorgio Carelli, Angela Di Virgilio, Enrico Maccioni, Gilberto Saccorotti, Fabio Stefani, and Alexander Velikoseltsev. Horizontal rotation

- signals detected by “g-pisa” ring laser for the mw = 9.0, march 2011, japan earthquake. *Journal of Seismology*, 16(4):767–776, 2012.
- [48] Krishna Venkateswara, Charles A. Hagedorn, Jens H. Gundlach, Jeffery Kissel, Jim Warner, Hugh Radkins, Thomas Shaffer, Brian Lantz, Richard Mittleman, Fabrice Matichard, and Robert Schofield. Subtracting tilt from a horizontal seismometer using a ground rotation sensor. *Bulletin of the Seismological Society of America*, 107(2):709–717, 2017.
- [49] Brian Lantz, R Schofield, B. O'Reilly, D. E. Clark, and D DeBra. Review: Requirements for a ground rotation sensor to improve advanced ligo. *Bulletin of the Seismological Society of America*, 99(2B):980–989, 2009.
- [50] Norman A Haskell. The dispersion of surface waves on multilayered media. *Bulletin of the Seismological Society of America*, 43(1):17–34, 1953.
- [51] Fan-Chi Lin, Morgan P. Moschetti, and Michael H. Ritzwoller. Surface wave tomography of the western united states from ambient seismic noise: Rayleigh and love wave phase velocity maps. *Geophysical Journal International*, 173(1):281, 2008.
- [52] J Aasi et al. Advanced ligo. *Classical and Quantum Gravity*, 32(7):074001, 2015.
- [53] T. Meier, K. Dietrich, B. Stöckhert, and H.P. Harjes. One-dimensional models of shear wave velocity for the eastern mediterranean obtained from the inversion of rayleigh wave phase velocities and tectonic implications. *Geophysical Journal International*, 156(1):45–58, 1 2004.
- [54] Cédric P. Legendre, Li Zhao, Win-Gee Huang, and Bor-Shouh Huang. Anisotropic rayleigh-wave phase velocities beneath northern vietnam. *Earth, Planets and Space*, 67(1):28, 2015.
- [55] A. Einstein and N. Rosen. On gravitational waves. *Journal of the Franklin Institute*, 223(1):43 – 54, 1937.

- [56] Rainer Weiss. Electromagnetically coupled broadband gravitational antenna. In *K.S. Thorne, “Gravitational radiation”, 300 Years of Gravitation, S W Hawking and W Israel, pp 330–458.* University Press, 1972.